Winter 12-19-2020

Microparticle Propulsion for in vivo Navigation

Louis Rogowski
Southern Methodist University, lrogowski@smu.edu

MICROPARTICLE PROPULSION FOR *IN VIVO* NAVIGATION

Approved by:

_____
Prof. Min Jun Kim
Professor

_____
Prof. Ali Beskok
Professor

_____
Prof. Pia Vogel
Professor

_____
Prof. Edmond Richer
Associate Professor

_____
Prof. David Willis
Associate Professor

MICROPARTICLE PROPULSION FOR *IN VIVO* NAVIGATION

A Dissertation Presented to the Graduate Faculty of the

Bobby B. Lyle School of Engineering

Southern Methodist University

in

Partial Fulfillment of the Requirements

for the degree of

Doctor of Philosophy

with a

Major in Mechanical Engineering

by

Louis William Rogowski

B.S., Mechanical Engineering, Drexel University
M.S., Mechanical Engineering, Southern Methodist University

December 19, 2020

ACKNOWLEDGMENTS

This work would not have been possible without the guidance, patience, and mentorship of my advisor, Dr. Min Jun Kim. I am grateful to my mother, father, and extended family for their generous support and love over the last decade as I went from undergraduate, to masters, to PhD. I would like to thank my committee members: Dr. Pia Vogel, Dr. Edmund Richer, Dr. Ali Beskok, and Dr. David Willis for their participation. I would like to thank my collaborators across the globe with special praise to Dr. Henry C. Fu, for all of his guidance and help formulating the theory for spontaneous symmetry breaking, and to Dr. James N. Wilking, for helping with first and second normal stress difference measurements. I would like to thank the United States and its leadership over the last four years for creating an environment where this research was made possible. I would like to thank Southern Methodist University for all of its resources and support. I would like to thank Dr. Kenneth Berry for all the opportunities to introduce young and bright minds to microrobotics research. I would like to thank my colleagues Dr. Jamel Ali, Dr. Hoyeon Kim, and Dr. U Kei Cheang for all of their support over the years. Finally, I would like to thank my dear friends: Jugal Saharia, Xiao Zhang, Anuruddha Bhattacharjee, Gokhan Kararsiz, Jiannan Tang, Matthew O'Donohue, Micah Oxner, Jung Soo Lee, Nuwan Bandara, Buddini Karawdeniya, and everyone else who left an impact on me over the last four years. Without all of you and your combined support, I would not be who I am today, and none of this would have been possible. Thank you all.

Louis William Rogowski B.S., Mechanical Engineering, Drexel University
M.S.M.E., Southern Methodist University

Microparticle Propulsion for *in vivo* Navigation

Advisor: Dr. Min Jun Kim

Doctor of Philosophy conferred December 19, 2020

Dissertation completed November 2, 2020

Microscale propulsion impacts a diverse array of fields, with simplistic microrobots allowing for novel innovations in microscale surgery and drug delivery. Propulsion at the microscale is constrained by physics, with time-reversal and geometric symmetries limiting available propulsion mechanisms. However, certain fluid environments and surface coatings allow for the propulsion of microparticles through externally applied magnetic fields. Presented here is a detailed analysis of microparticles propelling using spontaneous symmetry breaking, flagella surface coatings, and multi-modal actuation mechanisms. Spontaneous symmetry breaking in nonlinearly viscoelastic fluids is presented for the first time in literature, with two equal and opposite propulsion states existing along a microparticles rotation axis. Flagellated microparticles suspended in Newtonian fluids are demonstrated to have diverse behavior in response to rotating magnetic field frequency and direction. Finally, catalytic Janus particles were developed which could exhibit catalytic propulsion and swimming propulsion interchangeably. The continued exploration of these propulsion mechanisms will be used to further circumvent restrictions on propulsion, helping to revise notions of microrobotic design and control, drug delivery, microscale pumping, and locomotion of microorganisms.

TABLE OF CONTENTS

LIST OF FIGURES

LIST OF TABLES

This work is dedicated to my family, my country, my friends, and my kindred spirits across the globe. May we all find the courage to thrive no matter what future we march towards.

CHAPTER 1

INTRODUCTION

Microrobotics began in 1959 when Dr. Richard Feynman gave his speech 'There's Plenty of Room at the Bottom'[1]. In this short talk he described how technology would one day become so advanced that patients would literally be able to 'swallow the surgeon.' It did not take the entertainment industry to latch onto this idea and present such fantastical technologies in films such as 'The Fantastic Voyage,' 'Innerspace,' 'Big Hero 6,' and a myriad of others. Over the half-century since that speech, multiple researchers around the globe have made progress in developing microscale robots for applications such as minimally invasive surgery and targeted drug delivery. Several microrobots were developed using direct laser writing (DLW) methods[2,3] and were demonstrated to perform cargo transport applications[4-12]. Other helical based microrobots were assembled through templating organic geometries[13-15] and polymers[16,17], while countless other microrobots have been developed to achieve meaningful propulsion utilizing catalytic propulsion[18,19], nonreciprocal actuation of magnetic microparticle aggregates[20,21], and acoustic actuation[22].

While all of these microrobotic platforms are interesting, they all utilize complex fabrication techniques to create specialized geometries in order to achieve swimming propulsion in low Reynolds number environments. At such small scales, the hydrodynamics are described by the viscosity-dominated Stokes equations[23], and propulsion mechanisms are often limited by their geometric symmetries and the physical laws governing Stokesian hydrodynamics. For example, in Newtonian fluids force- and torque-free biological swimmers have been analyzed in terms of time-

reversal symmetry of Stokes flow, with the resulting Scallop theorem[24] requiring that kinematic reversibility be broken by non-reciprocal strokes to achieve propulsion[25,26]. The same principle applies to microrobotic propulsion, where kinematic reversibility must be broken either through non-reciprocal flexible response to reciprocal actuation, or by non-reciprocal actuation, such as steady rotation *via* magnetic fields – the type focused on throughout the remainder of this thesis. For these, the analysis of hydrodynamic mobility matrices reveals that geometries more symmetric than a flat triangle do not couple torque to linear translation[27,28] and hence cannot be propelled by rotation; furthermore, symmetry analyses of the entire dynamical system, including actuating fields and moments, have shown that there is no average propulsion of rotated microrobot populations that are symmetric under combined charge conjugation and parity[29].

Due to three-dimensional symmetry, spherical microparticles cannot convert torques produced by externally applied rotating magnetic fields into translational motion. Microparticles are unique, however, in that they are already utilized in a great deal of medical applications including hyperthermia, magnetic resonance imaging, and enhanced drug delivery. Additionally, microparticles are easy to fabricate and can be functionalized with a variety of chemical surface coatings that can be used to either attach drug delivery agents or improve diffusivity through specific fluids. The development of simple and efficient propulsion mechanisms for microparticles will further improve their utility in existing medical applications and can be transitioned quickly for use in new procedures. This thesis will experimentally demonstrate several propulsion mechanisms that have been developed at Southern Methodist University by myself and collaborators to enable microparticle propulsion with rotating magnetic fields; many of which were achieved for the first time. These techniques include: 1) a novel spontaneous symmetry breaking propulsion mechanism from microparticles in nonlinearly viscoelastic fluids, 2) the guided

propulsion of microparticles with heterogeneous flagellated surface coatings, and 3) the multi-modal propulsion of catalytic Janus particles that possess both platinum and flagella surface coated hemispheres. The spontaneous symmetry breaking method is demonstrated for the first time in literature, where microparticles propel using hoop stresses generated from first and second normal stress differences in nonlinearly viscoelastic fluids[30,31]. Flagellated microparticles rely on the chemical functionalization of bacterial flagella which explicitly break the geometry of the microparticles; instead of a single flagellum as in other microswimmers, surface coatings are heterogenic and randomly distributed[32]. Finally, catalytic Janus particles are hemispherically coated with platinum and bacterial flagella to enable both catalytic propulsion and swimming propulsion; the first Janus particles developed which can perform two distinct motion modes[33]. All three microparticle based millirobots have enormous potential for *in vivo* operation and in a few years will be used to improve existing medical technologies and procedures. The following chapters will provide a brief introduction to each propulsion method, their experimental results, a brief discussion summarizing the contents, and a methods section associated with each chapter. Several experimental procedures and set ups are used interchangeably between each chapter and will be referred to as needed. A conclusion at the end of the thesis will summarize the major results from each propulsion mechanism and a future work section will be used to examine the next steps of this research. All of the research presented here has been published, presented at conferences, or is currently under consideration by reputable scientific journals.

CHAPTER 2

SYMMETRY BREAKING PROPULSION OF MAGNETIC MICROSPHERES IN NONLINEARLY VISCOELASTIC FLUIDS

2.1 Introductory Remarks

In non-Newtonian fluids, time-reversal symmetry is explicitly broken and kinematic reversibility does not hold, allowing reciprocal strokes to achieve propulsion[34-36]; however, geometrical symmetry analyses still apply. Of particular importance here is fore-and-aft symmetry relative to the direction of propulsion. It is usually thought that propulsion is not possible in a fore-aft symmetric system; for if there is a single state with propulsive velocity, upon fore-aft reflection the velocity [U, Fig. 2.1 (a)] must be simultaneously reversed [to U', Fig. 2.1 (a)] and equal to the original, and hence be zero[37]. For example, experiments achieving propulsion by reciprocal actuation of dumbbells in nonlinearly viscoelastic fluids[38] instead explicitly break fore-aft symmetry by employing either dumbbells with two different sized beads, or a boundary nearby symmetric dumbbells. In a theoretical analysis of axisymmetric swimmers rotated along their axis of symmetry in nonlinearly viscoelastic fluids, fore-aft symmetry led to the conclusion that the simplest shapes capable of propulsion are "snowmen" constructed of two differently-sized spheres[39]. The same symmetry considerations suggest that it is not possible for a steadily rotating sphere to be propelled along its rotation axis.

Symmetry analysis in nonlinear low Reynolds regimes neglect the possibility of spontaneous symmetry breaking, in which a pair of translating states exists with equal and opposite propulsion velocities, rather than a single state with zero velocity. Here, we report the spontaneous symmetry breaking propulsion of rotating spherical magnetic microparticles within two different non-Newtonian fluids: a low concentration polyacrylamide solution and a synthetic mucus

solution. Application of a static magnetic field can select between the two states, enabling control of the propulsion direction. We propose a physical mechanism for symmetry breaking that arises from nonlinear viscoelastic effects in rotating flows, similar to the rod-climbing effect, which pushes the sphere along its rotation axis. The mechanism is corroborated by comparison to existing theoretical analyses of rotating and translating spheres in generic third-order fluids[40]. Thus, for the first time we demonstrate that spontaneous symmetry breaking can be used to propel and control rigid spherical magnetic microparticles without requiring magnetic gradients, geometry-altering surface coatings, or catalytic propulsion. Our results will enable improved applications of microparticles, especially biomedical, as well as insights into locomotion of living and artificial microswimmers in complex fluids. This work was performed in collaboration with Dr. Henry C. Fu of the University of Utah and Dr. James N. Wilking of Montana State University.

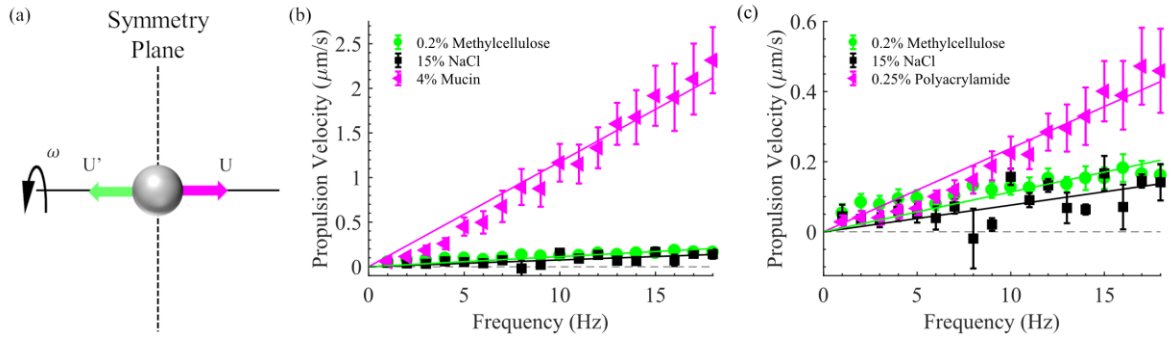

Fig. 2.1. Propulsion characteristics of microparticles. (a) Reflection about the symmetry plane leaves the geometry and rotation unchanged but reverses the propulsion velocity U to U'. If there is only one state, U = U' = 0, but spontaneous symmetry breaking results in two propulsive states with equal and opposite velocities U and U'. Propulsion velocity vs. rotational magnetic field frequency for 10 μm diameter microparticles in (b) 4% mucin and (c) 0.25% polyacrylamide. Control experiments using 10 μm diameter microparticles were performed in two Newtonian fluids: 15% NaCl and 0.2% methylcellulose; both were plotted in both (b) and (c) to compare with the propelling microparticles. The coefficient of determination (r^2) values for the linear fit in 4% mucin solution and 0.25% polyacrylamide solution were 0.9650 and 0.9449, respectively, indicating a strong linear correlation of velocity and frequency. In contrast, the r^2 values for the linear fits to controls in 15% NaCl and 0.2% Methylcellulose solution were 0.3773 and 0.2036, respectively, indicating little correlation with frequency. Error bars represent standard error.

2.2 Results

Spherical magnetic microparticles were observed to translate while exposed to uniform rotating magnetic fields in both a 4% mucin solution and a 0.25% polyacrylamide solution. Motion both perpendicular (transverse) to and along the field's rotation axis were observed within both non-Newtonian fluids. We attribute the transverse motion to the well-understood rolling motion along the boundary caused by the particles rotation[41,42], since the transverse velocity weakened as the distance from the boundary increased, reversed upon reversal of the rotation direction, and had a linear relationship with frequency nearby the boundary (Fig. S1-S3). On the other hand, the motion along the rotation axis was surprising since it is symmetry-prohibited [Fig 2.1 (a)]. In the rest of this chapter we focus on this symmetry-prohibited motion, hereafter referred to as propulsion. All experiments reported were conducted far from the substrate surface (> 100 μm) to minimize boundary effects (Fig. S1) unless otherwise stated.

When the magnetic field rotated in a plane, the propulsion direction was seemingly randomly oriented either along or opposite the rotation axis (perpendicular to the plane) and independent of the rotation direction. However, we found that imposing a symmetry-breaking static magnetic field (2 mT) along the rotation axis fixed the direction of propulsion and we used this to investigate the dependence of propulsion velocity on rotational frequency [Fig. 2.1 (b-c)]. Both 4% mucin and 0.25% polyacrylamide are viscoelastic and shear thinning at the applied shear rates[36,43-45] and possessed significant first and second normal stress effects (2.4 Methods, Fig. 2.5). Polyacrylamide solutions are known to have first and second normal stress differences[46,47], and we were able to measure normal stress differences in 10% mucin solutions (see 2.4 Methods, Fig. 2.5 and Appendix Section 10). In both fluids there was a nearly linear relationship between propulsion velocity and frequency. Note that the propulsion decreased to almost zero as the rotational

frequency approached zero, implying that static magnetic field gradients are not responsible for propulsion; see Appendix Section 8 for further experiments that rule out this possibility. In control experiments using the Newtonian fluids 0.2% methylcellulose[48] and 15% NaCl, we observed small, nearly vanishing, propulsion velocities that were not correlated with frequency. Since this small propulsion velocity was observed even without any actuation (at near zero frequency) we attribute it to an internal flow within the sample chambers. Propulsion was ubiquitous among rotated microparticles; it was observed for beads of several different diameters (2, 4, 8 μm) in mucin solutions of various concentrations (2%, 3%, 4%) and in the polyacrylamide solution (see Appendix Section 9). Propulsion was observed for >90% of beads in mucin solution, and >60% of beads in polyacrylamide solution.

The observed propulsion was repeatable and could be controlled under both open-loop and closed-loop feedback control schemes (see 2.4 Methods for details, see Appendix). Figure 2.2 (a) shows an open-loop trajectory in which the microparticle was directed to create a square shape. Transverse rolling slightly skewed the trajectory in Fig. 2.2 (a) and was influenced by the microparticles' rotation direction (Appendix Section 2). During these experiments the microparticles sometimes encountered localized regions of hindered propulsion, as seen in Fig. 2.2 (b), where the microparticle could not perform the desired trajectory during the first downward segment; further examples can be seen in Fig. S1 (b) where propulsion velocity varies with location in the mucus medium. We suspect that these localized regions correspond to elevated concentrations of mucin glycoprotein entanglements as they were far less common in the homogeneous polyacrylamide solution. Given enough time, microparticles usually navigated around these regions and completed their intended trajectories. Closed-loop feedback control was used to navigate microparticles along trajectories, such as those in Fig. 2.2 (c-g), where the target

points and desired trajectories are shown as magenta dots and dashed lines, respectively. Microparticles usually generated trajectories relative to the intended paths with small levels of

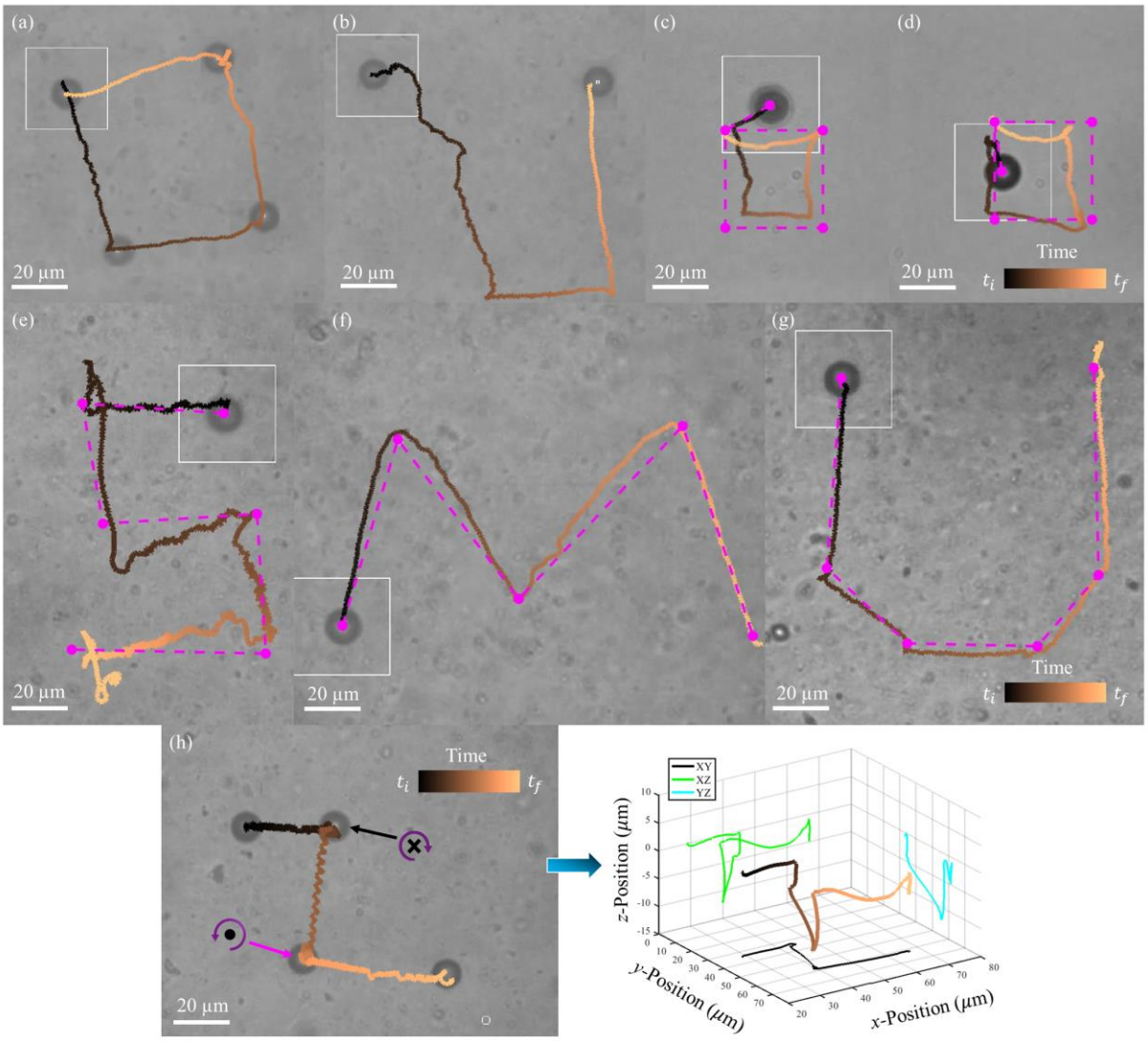

Fig. 2.2. Path planning of microparticles in nonlinearly viscoelastic fluids. (a) Open-loop control of a microparticle performing a square trajectory in 4% mucin. (b) Open-loop control of a microparticle in 4% mucin, which encounters a region of relatively high fluid resistance, disrupting its initial downward motion. Selected trajectories of a microparticle under closed-loop feedback control in 0.25% polyacrylamide (c-d) and 4% mucin (e-g), where magenta dots represent the intended targets and dashed lines represent shortest path. The times associated with each trajectory are (a) 80 seconds, (b) 95 seconds, (c) 156 seconds, (d) 145 seconds, (e) 94 seconds, (f) 60 seconds, and (g) 43 seconds. (h) Left: a simple 3D trajectory that was achieved using open-loop control. At the points indicated by the arrows, the microparticle translated downwards in the negative *z*-direction (black arrow) and then upwards in the positive *z*-direction (magenta arrow); the circular purple arrow signifies rotation direction from behind the heading vector, while the black circle and 'X' represent out of the page and into the page respectively. Right: the estimated 3D trajectory of the microparticles path and superpositions along the different planes; the total time of the trajectory was 114 seconds. Microparticles were rotated at (a-c, e-g) 19 Hz, (d) 40 Hz, and (h) 15 Hz.

error (Fig. S8). Finally, open-loop control in 3D was achieved [Fig 2.2 (h), details in Appendix Section 4] during which the microparticle was directed to propel along the positive *x*-direction, along the negative *z*-direction (into the page), along the negative *y*-direction, along the positive *z*-direction (out of the page), and then finally along the positive *x*-direction again. Although simple, this trajectory shows that 3D control is feasible using these microparticles and trackable by correlating the pixel area of the microparticle to its *z*-position above or below the focal plane [Fig. S9 (a-c)]. Appendix Section 4 details 3D propulsion of a microparticle within 0.25% polyacrylamide. Notably, since propulsion generally continued as microparticles translated through the fluids, rather than being limited to specific regions, these demonstrations of control rule out interactions with specific heterogeneities as the origin of the propulsion[49].

In the above experiments, application of a magnetic field controlled propulsion to occur in the direction of the static magnetic field, so we next investigated the dependence of propulsion on the static magnetic field. We gradually changed the applied static magnetic field from -5 mT to 5 mT in 1 mT increments while rotational frequency remained constant, and observed the average propulsion velocity of 10 μm diameter microparticles at each increment [Fig. 2.3 (a), details in 2.4 Methods]. As the static magnetic field approached 0 mT, the average propulsion velocity switched direction, from negative to positive, while remaining nearly constant for larger positive and negative fields. To further understand this phenomenon, the static magnetic field was varied at smaller 0.2 mT increments [Fig. 2.3 (b)], revealing that the switching field strength depends on the increment size; for smaller increments the average propulsion direction did not switch until the static field reached 0.8 mT for this particular microparticle in 4% mucin. Furthermore, upon tracking the velocity of individual microparticles in 4% mucin [Fig. 2.3 (c)], we found that each particle switches propulsion direction at drastically different static fields with only a slight variance

of the switching field observed between individual trials [Fig. S4 (a)]. When performing the same

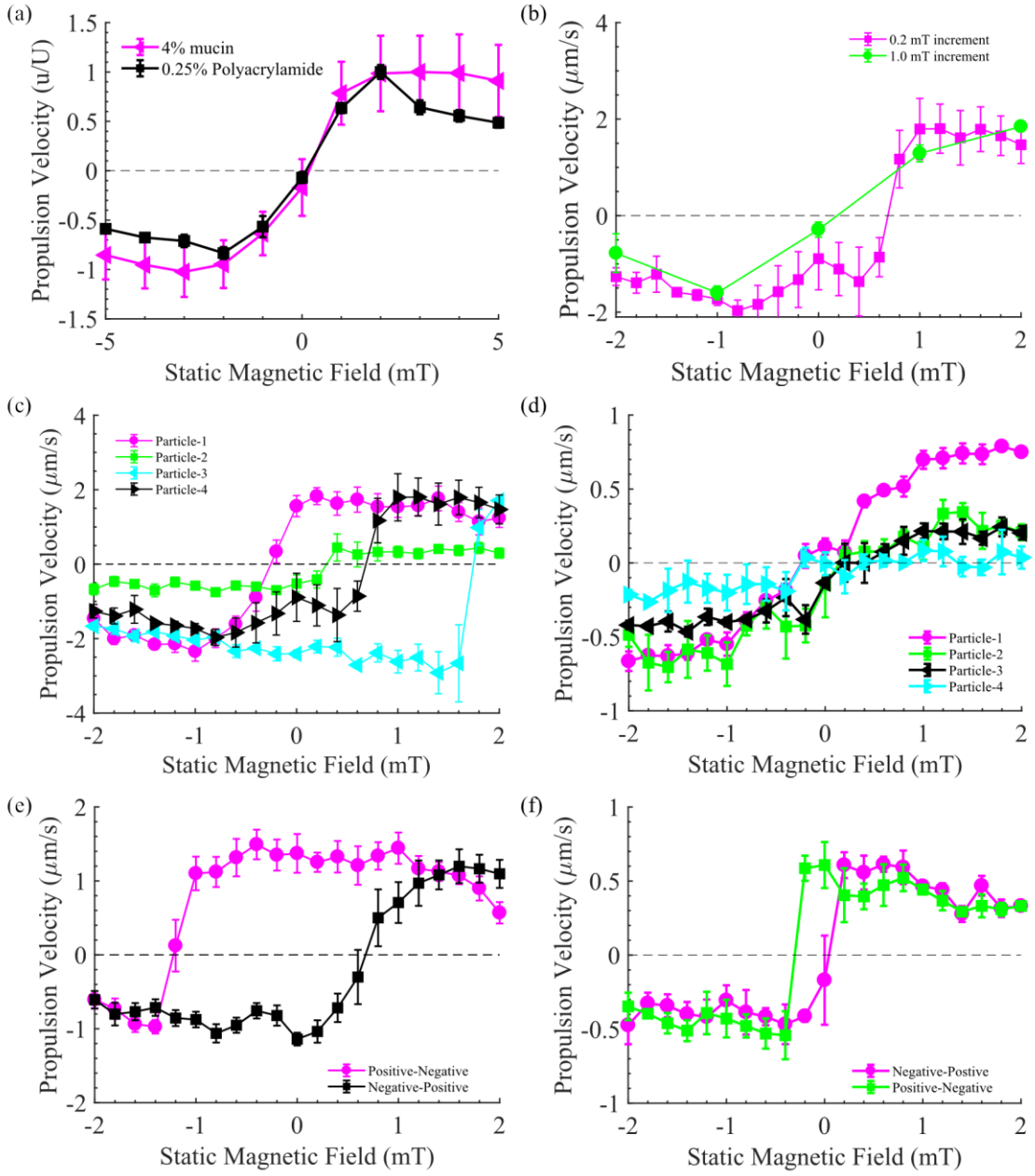

Fig. 2.3. Effect of static magnetic field on propulsion. Velocity vs. static magnetic field for 10 μm diameter microparticles for: (a) static field swept at 1 mT increments between the range of -5 and 5 mT, with the microparticles rotated at 15 Hz. Four microparticles were examined and each had at least 3 trials in each fluid. (b) Static magnetic field swept in 0.2 mT increments and 1 mT increments for the same microparticle in 4% mucin. (c-d) Static magnetic field swept in 0.2 mT increments for 4 different particles for 4% mucin and 0.25% polyacrylamide, respectively. (e-f) Propulsion hysteresis in response to static magnetic field sweep at 0.2 mT increments for a single microparticle in 4% mucin and 0.25% polyacrylamide, respectively. The frequency for (f) was 40 Hz with the rotating magnetic field amplitude set to $|B_r| = 0.175f$, where f is the frequency in Hz. In all scenarios, velocities of microparticles remained relatively constant at larger positive and negative fields, but the field at which velocity switched direction depended on static magnetic field history, increment size, and specific particle characteristics. Dashed lines in graphs represent zero propulsion velocity while lines between points in (a)-(f) were added to act as a guide to the eyes. Error bars represent standard error.

experiments in 0.25% polyacrylamide (15 Hz), the variation between individual microparticles was lost [Fig. 2.3 (d)] and instead all microparticles switched directions close to 0 mT. Thus, we consistently observe the existence of propulsion and switching of propulsion direction as the static field is swept, although there is strong variability in the propulsion velocity and switching frequency for different static field histories and increment sizes (see Appendix Section 2), which could be due to factors such as interparticle variation and medium heterogeneity (see Appendix Section 9). In the remainder of the chapter we focus on understanding the robust existence of propulsion and whether the static magnetic field is necessary for propulsion to occur.

To elaborate on how a static field might be able to control the propulsion direction of a rotating microparticle, first consider that in a Newtonian fluid standard analytic solutions indicate that a sphere rotated by an external torque will not translate[50], consistent with the results in Fig. 2.1 (b-c). When the magnetic field rotates in a plane, the magnetic dipole of the sphere also rotates in the same plane and the sphere rotates along the same axis as the field. If there is also a static field along the rotation axis, the magnetic dipole tilts towards the static field and continues to rotate with the field, but now there is an additional rotation of the sphere along the axis of the magnetic dipole (see Appendix Section 5). Despite the more complicated rotational dynamics, the microparticle in a Newtonian fluid will not translate. Remarkably, we have observed the consistent translation of such spheres in synthetic mucus and polyacrylamide. The more complex rotation and the static field explicitly break the fore-aft symmetry, but due to the robust observation of propulsion combined with variability in switching of propulsion direction we hypothesized that there is an underlying spontaneous symmetry-breaking translation for a force-free sphere rotated by an external torque in a nonlinearly viscoelastic fluid. Such symmetry-breaking leads to pairs of translational states with equal and opposite velocities in the rotation direction, consistent with

our observations above. The behavior observed with a symmetry-breaking static field can be thought of as selecting one symmetry-broken state over the other. To test if we could instead observe *spontaneously* (not explicitly) broken symmetry, we swept the static magnetic field from 2 mT to -2 mT and then back to 2 mT in 0.2 mT increments. As seen in Fig. 2.3 (e), the propulsion velocity in 4% mucin has a hysteretic response to the field strength, switching direction at around -1.2 mT (from positive to negative) and then switching back at around 0.8 mT (from negative to positive). The experiment in 0.25% polyacrylamide showed much sharper changes between propulsion states [Fig. 2.3 (f)] but at 0 mT two separate propulsion states could still be achieved, although only at a higher rotational frequency (40 Hz). In the Appendix [Fig. S4 (b), S5] we show that the switching points depend on magnetic field increment and frequency. Thus, in both fluids, at an applied static field of 0 mT, we could observe both directions of propulsion for both fluids (on the downward and upward sweeps), corresponding to truly spontaneously symmetry-broken propulsive states. We were consistently able to demonstrate symmetry broken propulsive states in microparticles that showed propulsion. In mucin solution, all particles tested showed hysteresis when subjected to negative and positive sweeps of the magnetic field. In polyacrylamide solution, all 4 particles tested showed hysteresis (see Appendix Section 2, Fig. S6), although we note that the strength of hysteretic effects was dependent on frequency; when actuated at 15 Hz very little hysteresis was observed and microparticles switched propulsion direction at close to zero static field for both positive and negative sweeps.

The hysteretic behavior of propulsive velocity is reminiscent of those seen in other spontaneously symmetry breaking phenomena, such as ferromagnetism, but ferromagnetic behavior cannot explain our observations, since the coercive fields of 68 mT[51] required to magnetize and demagnetize our beads are much larger than the magnitudes of combined rotational

and static fields used in our experiments (3.11–15.87 mT). Instead, we propose that the symmetry breaking mechanism is caused by nonlinear viscoelastic stresses that arise in rotating flows, similar to those responsible for the "rod-climbing" effect. Around a vertical rotating rod in a polymeric fluid, nonlinear first normal stress differences cause excess circumferential hoop stresses along the circular streamlines, while second normal stress differences cause excess radial stress; both can squeeze the fluid upwards around the rod[47]. We note that both polyacrylamide and mucin solutions display first and second normal stress differences that lead to rod-climbing-like effects (see 2.4 Methods, Fig. 2.5, and Appendix Section 10). For a rotating and translating sphere, fluid material also advects past the sphere, so that fluid elements at the back of the sphere have spent more time circling the sphere than those at the front; thus, the back of the sphere has larger nonlinear viscoelastic stresses than the front, producing a net squeezing force that propels the sphere forward. A force-free symmetry-breaking translational state occurs when this propulsive force balances the drag force from translation.

To theoretically test this idea, we analyze the force on a sphere rotating with angular frequency Ω and translating with velocity U using a retarded motion expansion in a generic third-order non-Newtonian fluid[47] (detailed in Appendix Section 6). The force F along the rotation axis was calculated as a perturbation expansion in the Deborah number $\mathrm{De} = \lambda\Omega$, where λ is a timescale for fluid relaxation,

$$F = F^{(0)} + \mathrm{De}F^{(1)} + \mathrm{De}^2F^{(2)} + \cdots \tag{2.1}$$

The zeroth order velocity field is that of a rotating and translating sphere in a Newtonian fluid, and the zeroth order force $F^{(0)}$ is given by Stokes' law for the drag of a translating sphere, $F^{(0)} = -6\pi\mu aU$, where a is the microparticle diameter and μ is the fluid viscosity. The first correction

to the force arises at order De^2, and contains terms proportional to $\Omega^2 U$ and to U^3. The former term, $F_{thrust}^{(2)} = C\Omega^2 U$, where C is a constant that depends on the parameters of the constitutive law, corresponds to the symmetry-breaking propulsive thrust since it couples rotation and translation in a way that is independent of rotation direction[27]. If $C > 0$, then there is a nonlinear thrust in the same direction as translation which could stabilize a translating symmetry-broken state, i.e., a rotating non-translating sphere could become unstable to translation; while if $C < 0$, then nonlinear effects stabilize the zero-velocity state. Due to the instability of the non-translating state, upon rotating an initially stationary sphere any small perturbation would lead to the symmetry-broken translating state. The sign of the force contribution depends on the parameters specifying the third order fluid, which are known for common fluid models. As detailed in the Appendix Section 6, we have found that the force contribution is positive for many model constitutive laws, implying that nonlinear fluid response can lead to symmetry-breaking propulsion in many types of non-Newtonian fluids. The form of $F^{(2)}_{thrust}$ suggests that there may be a critical rotation rate at which it balances the drag $F^{(0)}$, and symmetry-breaking propulsion becomes possible. Finally, we note that although in a second-order fluid, rod climbing is directly related to the first and second normal stress coefficients that specify the constitutive law[47], our propulsive force is a higher order effect that can only be consistently described using all the parameters that specify a third order fluid, implying that nonlinearities beyond the normal stress differences impact symmetry breaking propulsion.

To support this proposed symmetry breaking mechanism, we used microscale particle image velocimetry (μPIV) to visualize the flow fields of microparticles within 4% mucin. These experiments were performed using a different experimental set up, but with operating parameters identical with the previous experiments (see 2.4 Methods). Figure 2.4 (a-i) shows instantaneous

snapshots of the μPIV velocity flow fields in the *x*-*y* plane and their indicated component velocities for: (a-c) a microparticle that could not propel, (d-f) a microparticle propelling, and (g-i) a microparticle propelling along the positive *z*-direction. In Fig. 2.4 (a) the propulsion velocity flow fields to the left and right of the microparticle cancel each other out, while the transverse velocities in (b) are unidirectional; this results in (c) having no net propulsion along the propulsion axis. In

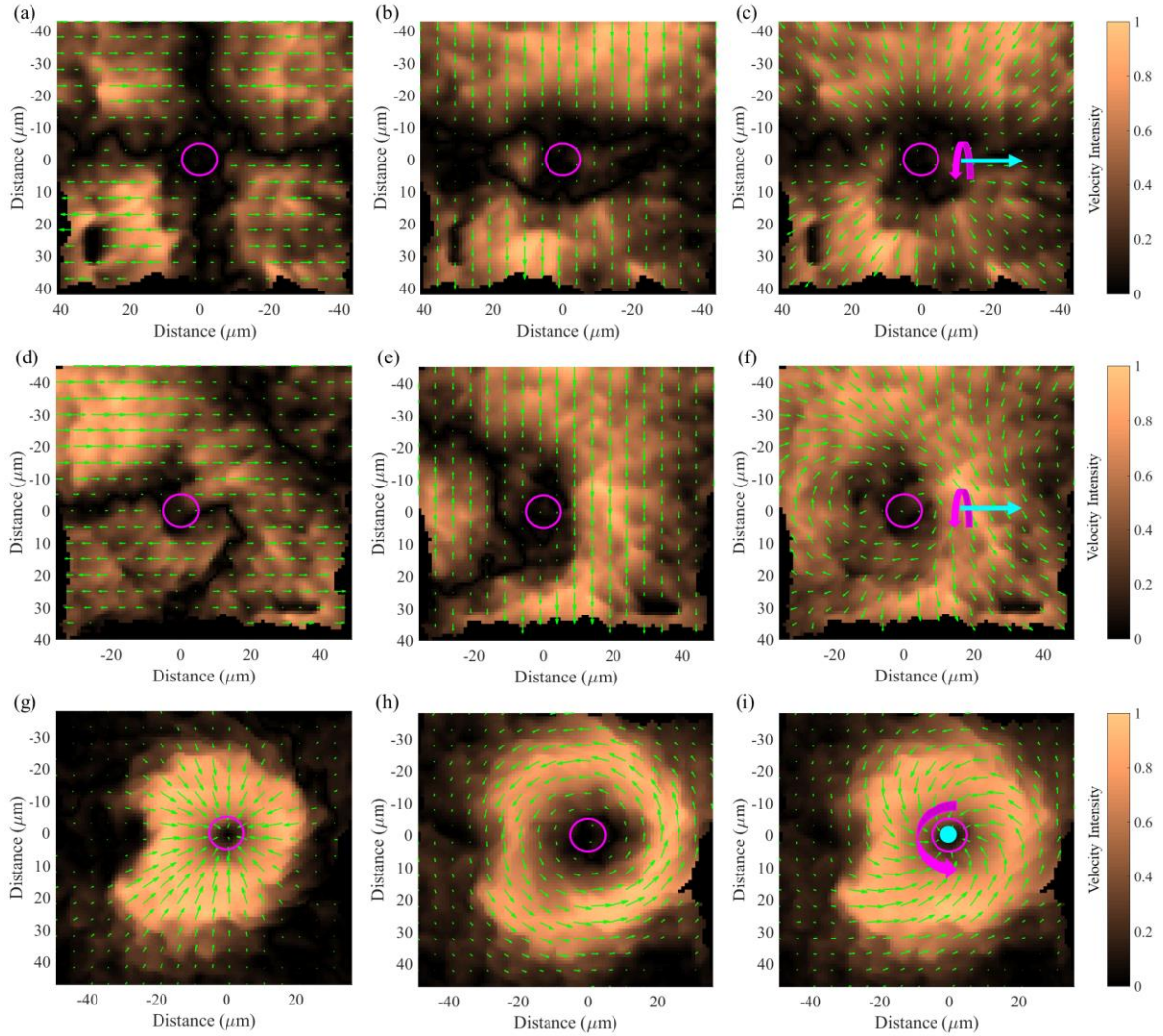

Fig. 2.4. μPIV in *x*-*y* plane of microparticles in 4% mucin. The (a) propulsion direction, (b) transverse direction, and (c) total velocity flow field for a microparticle not propelling. The (d) propulsion direction, (e) transverse direction, and (f) total velocity flow field for a microparticle that is propelling. The (g) radial, (h) azimuthal, and (i) total velocity flow field for a microparticle propelling away from the substrate (positive *z*-direction). Inward radial flow is consistent with secondary flows generated by hoop stresses. All μPIV experiments were performed close to the boundary (< 100 μm, see 2.4 Methods). Cyan arrows represent propulsion direction and magenta arrow represents rotation direction. Magenta circle is the microparticle. Color bars to the right represents percentage of velocity magnitude with respect to the maximum velocity magnitude.

Fig. 2.4 (d) the velocity flow fields do not cancel each other out, and the transverse velocity in (e) to the left of the microparticle is no longer unidirectional; this results in (f) having a net propulsion velocity. When examining a microparticle propelling in the positive *z*-direction, we found that in addition to a persistent azimuthal component [Fig. 2.4 (h)], there is a radial component [Fig. 2.4 (g)] that converges towards the microparticle, resulting in the velocity flow field shown in Fig. 2.4 (i). Notably, in contrast to the flow around a rotating sphere in a Newtonian fluid, which is purely azimuthal[50], the significant inward radial flow is consistent with the secondary flows expected from our hypothesized propulsion mechanism involving rod-climbing-like effects. Supporting our proposed flow mechanism, we found that the observed radial flow closely agreed with the secondary flow predicted by the theoretical perturbation expansion described above (see Appendix Section 11 for details). Similar μPIV experiments for 0.25% polyacrylamide were also performed and can be found in Section 12 of the Appendix.

2.3 Discussion

Microrobots with geometry and actuation that obey fore-aft symmetry are often thought to be incapable of propulsion, but we have demonstrated that a spherical magnetic microparticle steadily rotated by a magnetic field spontaneously breaks symmetry to develop a pair of states with propulsion in opposite directions along the rotation axis. We proposed a mechanism for the symmetry breaking by which rod-climbing-like effects due to nonlinear viscoelasticity around the rotating sphere provide a propulsive force by squeezing at the rear of the sphere. A theoretical analysis shows that such propulsive forces develop quite generically in a range of fluids with nonlinear constitutive laws, and flow visualization reveals inward radial flows consistent with this mechanism. The two symmetry-broken states, and hence direction of propulsion, can be selected between by application of a static magnetic field along the rotation axis, enabling guided 3D

propulsion. This type of propulsion may be ubiquitous in nonlinear fluids; we demonstrated it in two different fluids that have normal stress differences which can lead to rod-climbing-like effects. We have also observed that microswimmers composed of two beads with similar diameters can propel through mucus solutions[35], thus we expect many other symmetric geometries to behave similarly.

In this chapter we focused on the existence and mechanism for symmetry breaking propulsion; further work is needed to completely understand the conditions (geometry, rotation frequency, fluid properties) required for symmetry breaking to occur, the size dependence and effect of boundaries on propulsion velocities, as well as how fluid properties and actuation history control the hysteresis and selection of propulsion direction. In addition, while the static magnetic field selects the propulsion direction, the precise mechanism by which the accompanying dipole tilting and dynamic rotation leads to selection remains poorly understood. The propulsive force we identified here may be related to recently observed reductions in drag on sedimenting and rotating spheres in nonlinear viscoelastic fluids[52] and the mechanism we described has some similarities to elastic instabilities in Couette-Taylor flows[53]; the analogy might shed light on criteria for the instability of the zero propulsion state of our microparticles to symmetry breaking states. Our perturbative analysis cannot find the symmetry-broken state, since that would require the second order nonlinear contribution to cancel the zeroth order drag, which violates the assumptions of the perturbative expansion; additional theoretical work which explicitly identifies symmetry-broken states in specific nonlinear fluids could also shed light on these questions, but would likely require direct numerical simulation.

For applications and broader impacts, the microparticles demonstrated here provide a novel avenue to improve existing medical applications. Spherical microbeads – easily fabricated and

functionalized[54-62] – are already being utilized for tasks including hyperthermia[63,64], delivery of therapeutics[65], magnetic resonance imaging[66,67], and the formation of efficient microswimmers[68]. As mucus is ubiquitous throughout the human body[43] and hinders the transport of medically loaded micro- and nanoparticles[43,69-73], the controllable propulsion of spherical microparticles through mucus solutions opens the door to enhanced efficacy in biomedical applications. The mechanism of nonlinear symmetry breaking may provide insight into microscale pumping and the locomotion of microorganisms, which, along with artificial microswimmers, experience altered and sometimes improved motility in complex fluids[74-79]. Hoop stresses such as we consider have been suggested to stabilize the trajectories of rotating bacteria[80]. In general, our work demonstrates that nonlinearities that do not explicitly break a symmetry may nonetheless enable microscale propulsion via symmetry breaking. Thus, it may be profitable to consider propulsion in other systems where it is seemingly disallowed by symmetry. Such symmetry-breaking propulsion has been predicted in autophoretic propulsion of chemically reactive particles[81], and in purely mechanical systems outside the zero-Reynolds number limit, for heaving flat plates via inertial effects[82]. In microscale systems, we speculate that there may be other nonlinearities that may lead to spontaneously symmetry-breaking propulsion not only for artificial microrobots but also living microorganisms.

2.4 Methods

Fabrication and Characterization of Nonlinearly Viscoelastic Fluids

Human mucus can range in mucin glycoprotein concentration between 2-5%; we chose 4% as a baseline value[43]. Synthetic mucus was synthesized using mucin from porcine stomach (Sigma Aldrich, ME2378), by adding mucin to 150 mL of deionized water to produce a 4% mucin w/v synthetic mucus formulation. A stir bar and hot plate set to 60°C was used to agitate the mixture

for 30 minutes. The mucus was then transferred to three 50 ml centrifuge tubes and centrifuged for 10 minutes at 1200 relative centrifugal force (rcf) to remove any large aggregates (> 5 μm) of undissolved mucus particulates from the sample. The supernatant was then transferred to fresh tubes and stored at 4°C until used in experiments. Scanning electron microscopy (SEM) was used to visualize the heterogeneous mesh fibers and the porous voids that make up mucins overall structure [Fig. 2.5 (a)]. Using a TA Instruments Discovery Hybrid Rheometer (DHR-3) the mucus samples were characterized using stress sweeps, which were performed using a 40 mm parallel plate under an incremental shear rate from 1 to 100 (1/s) with 30 seconds of averaging time used at each data point, with 5 points collected per decade. The averaged results for different mucin concentrations (at least 3 trials each) and 0.25% polyacrylamide are reported in Fig. 2.5 (b) where all samples possessed a clear and consistent shear thinning effect. As the concentration of mucin increased, the overall viscosity increased monotonically and the resulting viscosity curves were in good agreement with previous experimental studies reported in literature[45]. Additionally, it was found that the centrifugation step only moderately affected the overall rheological behavior of the mucus, as can be seen in Fig. 2.5 (c) which compares centrifuged and uncentrifuged 4% mucin formulations. Interestingly, mucin concentration was also demonstrated to positively effect microparticle propulsion as concentration increased (see Appendix Section 9). Oscillation experiments performed on the DHR-3, using a 40 mm parallel plate with a frequency of 10 Hz, for 4% mucin revealed that at low oscillation strains the storage and loss moduli (Pa) had similar magnitudes [Fig. 2.5 (d)]. As the oscillation strain increased the storage modulus decayed sharply, resulting in the mucus behaving more like a liquid once the loss modulus was dominant; this is consistent with the documented viscoelastic behavior of biological mucus[43]. Biological human mucus was not used in experiments because it had inconsistent rheological properties (which vary

between humans) and was difficult to store for long periods of time. While this synthetic mucus

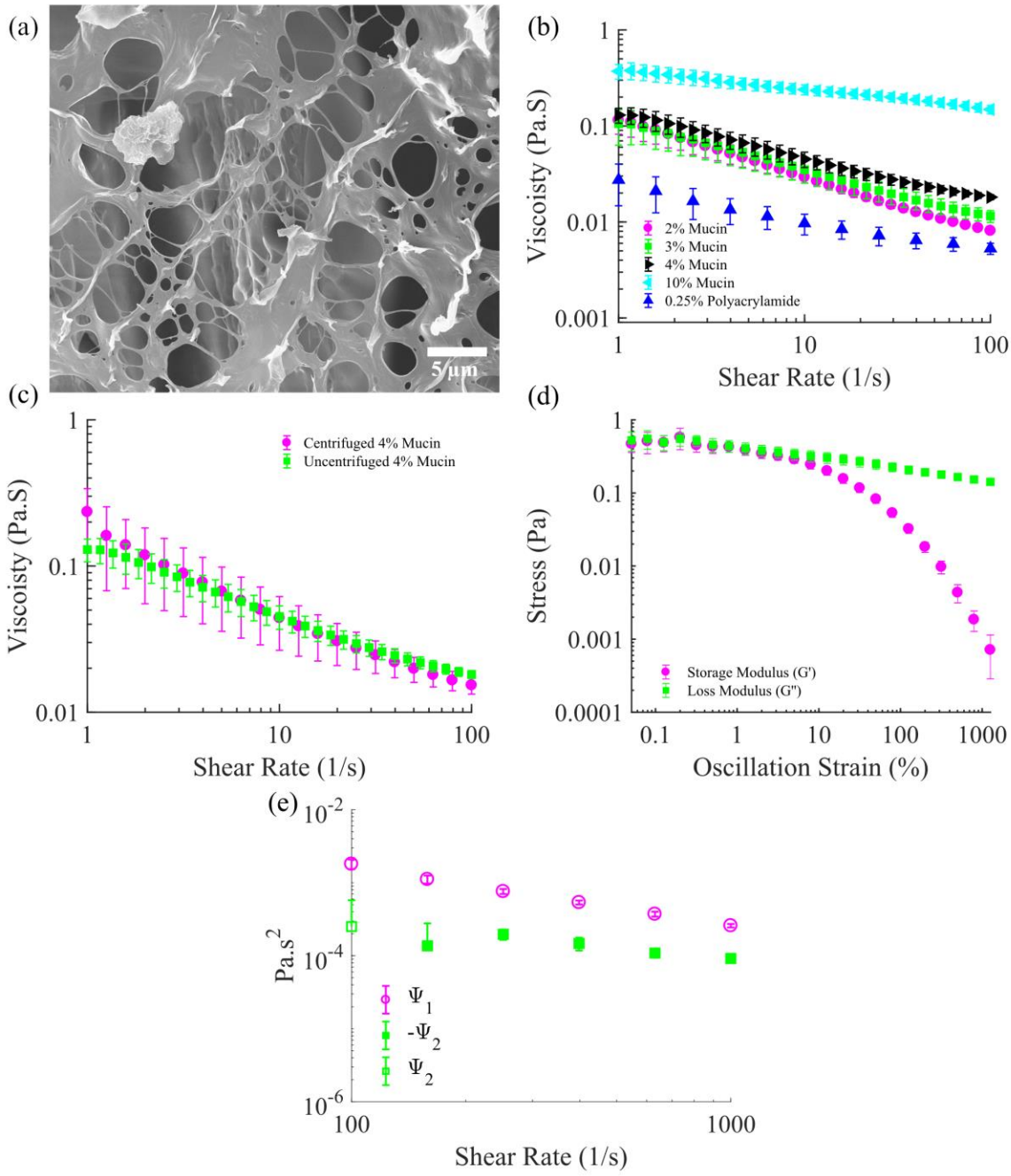

Fig. 2.5. Rheological characterizations of synthetic mucus and polyacrylamide. (a) Scanning electron microscopy (SEM) image of synthetic mucus. (b) Viscosity vs. shear rate curves for different concentrations of mucin and 0.25% polyacrylamide. (c) Comparison of centrifuged and uncentrifuged 4% mucin formulations. (d) Evolution of storage modulus (Pa) and loss modulus (Pa) with increasing oscillation strain for 4% mucin; frequency was fixed at 10 Hz during this experiment. (e) First (Ψ_1) and second (Ψ_2) normal stress coefficients for 10% mucin with theoretical inertial correction (see Appendix Section 10). Error bars represent standard deviation.

formulation lacks many components typically found in human mucus (lipids, salts, DNA, proteins, etc.), literature suggests that mucus viscoelastic behavior is completely dominated by mucin glycoprotein concentration, whereas the other components only marginally contribute to these properties[43]. The saline solution used in control experiments was created by mixing deionized water and NaCl (Sigma Aldrich, S5886) into a 15% w/v ratio. Polyacrylamide solutions were fabricated by mixing polyacrylamide (Sigma Aldrich, 92560) with deionized water in a 0.25% w/v ratio. The polyacrylamide mixture was agitated overnight using a magnetic stir bar and heated at a temperature of 30°C. The 0.25% polyacrylamide was analyzed rheologically with a cone-and-plate geometry (40 mm diameter, 4° angle) using the same experimental procedure described previously for mucus; the results were similar to those reported in literature[45]. Methylcellulose (Sigma Aldrich, M0512) at a 0.2% concentration was synthesized using directions provided by Sigma Aldrich. It is known that polyacrylamide solutions develop first and second normal stress differences under applied shear[46,47]. We also measured the first and second normal stress differences developed by high concentration mucin solutions under shear from the axial forces measured by an TA Instruments AR-G2 rheometer using cone-and-plate (60 mm diameter, 2° angle) and parallel plate (60 mm diameter) geometries[83,84] (see Appendix Section 10 for details). The measured first and second normal stress coefficients for 10% mucin solution are shown in Fig 2.5 (e), with a positive first normal stress coefficient and smaller negative second normal stress coefficient. Such normal stress differences are known to lead to rod-climbing effects. We also measured first and second normal stress differences in 2.5% polyacrylamide with results comparable to literature (Appendix Section 10). Note that the strain rate expected nearby a rotating sphere is equal to the angular velocity of the sphere; for our experiments this varies between 0-120 s^{-1}.

Control System Setup

Avidin-coated 10.6 μm ferromagnetic particles (Spherotech, SVFM-100-4) were suspended inside synthetic mucus or polyacrylamide solutions and were used for the majority of the experiments. Other microparticles utilized included 2 μm (SVFM-20-5), 4 μm (SVFM-40-5), and 8 μm (SVFM-80-4) diameters. Samples were prepared such that 0.5-1 μl of the ferromagnetic particle suspension of the selected diameter was added to 1.5 ml of either mucus or polyacrylamide solution. The sample was then vortexed slightly and placed on a permanent magnet for 15 seconds to magnetize the particles. Afterwards, 40 μl of the sample was added to a polydimethylsiloxane (PDMS) chamber, approximately 2 mm in diameter and 1 mm in height, that was situated on a number 1.5 glass coverslip (25 × 30 mm^2). An 18 × 18 mm^2 coverslip was then placed on top of the chamber to seal it, minimizing both evaporation and internal flows. The chamber was then loaded into an approximate Helmholtz coil system mounted to a Leica DM IRB inverted microscope (Type 090-132.701); a full description of the approximate Helmholtz coil system and it's magnetic field profiles can be found in Appendix Section 7. The Helmholtz coils do not produce any significant magnetic field gradients and Appendix Section 8 demonstrates that only rotating magnetic fields can propel a microparticle. A 63× objective was used to visualize microparticle motion within the sample chamber. A complementary metal oxide semiconductor (CMOS) camera (Point Grey, FL3-U3-13Y3M-C) was used to record experiments at 30 frames per second (fps) with a pixel resolution of 512 × 640 (0.152 μm/pixel). A customized LabVIEW program was developed to control signal outputs to interfaced digital acquisition (National Instruments, DAQ) control boards which then directed those signals to the attached power supplies (KEPCO, BOP-20-5M). There was one power supply per coil pair within the approximate Helmholtz coil system. The magnetic fields generated by this system are mostly uniform and no

meaningful magnetic field gradients are produced. A magnetic field was generated that is described by,

$$\vec{B} = \begin{bmatrix} -B_s \cos\theta + B_r \sin\theta \cos\omega t \\ B_s \sin\theta + B_r \cos\theta \cos\omega t \\ B_r \sin\omega t \end{bmatrix}, \quad (2.2)$$

$$\vec{n} = [-\cos\theta \quad \sin\theta \quad 0], \quad (2.3)$$

where B_s is the static magnetic field amplitude, B_r is the rotational magnetic field amplitude, ω is the rotational frequency (rad/s), t is the time (seconds), and θ is the heading angle of the propulsion direction. In experiments, B_r was adjusted to be proportional to the applied frequency ($|B_r| = 0.5f$, where f is the frequency in Hz) in order to prevent the magnetic microparticle rotation from desynchronizing with the rotation frequency of the magnetic fields[27]. The propulsion direction is defined to be along the rotation axis and corresponds to the heading vector ($\vec{n}$). When looking from behind the heading vector ($\vec{n}$), rotation can be defined as counterclockwise with positive ω and clockwise with negative ω. In a Newtonian fluid, when there is no static field ($B_s = 0$) and the rotational frequency is below a critical step-out frequency, a spherical microparticle with a permanent dipole moment rotates about the heading vector ($\vec{n}$) at the same rotational frequency as the field, and its dipole moment is in the plane perpendicular to $\vec{n}$ [28]. When there is an additional static field, the moment is tilted at a constant angle out of the plane perpendicular to $\vec{n}$, and the moment and microparticle rotate about $\vec{n}$ at the same frequency as the field, which makes the moment co-rotate with the field. This rotation is combined with an additional rotation of the particle about the moment direction (see Section 5 of the Appendix for details).

Experiment Details

The first set of experiments involved rotating microparticles suspended within fluids under incrementally increasing rotational frequencies. The rotation axis ($\vec{n}$) and propulsion direction were set to be along the positive *x*-direction, with the *z*-direction (height) oriented to be perpendicular to the coverslip. The transverse velocity was found to be a function of distance [Fig. S1 (b)-S2] from the substrate of the sample chamber and rotation direction (Fig. S3) of the rotating magnetic field; this motion corresponds to well-understood rolling motion along the nearest boundary[41,42]. As mentioned previously, in this paper we focus on propulsion along the rotation axis ($\vec{n}$) which is related to the fore-aft symmetry. For the experiments in Fig. 2.1, the static field (B_s, Eq. 3) was set to 2 mT, the heading angle (θ) was set to 0°, while the frequency (ω), was incremented from +1 to +18 Hz at 1 Hz increments ($\omega = 2\pi f$, where f is the frequency in Hz) counterclockwise when viewed from behind the heading vector. The time between each increment during the experiments was variable, but the video frames captured by the CMOS camera during the experiments could be precisely correlated to each increment, allowing for the accurate extraction of velocity data. All experiments described involve particles >100 μm from boundaries and at least three trials were conducted per microparticle with at least six microparticles examined per fluid; the results of all microparticles were then averaged together. Velocities were calculated by dividing the displacement of a particle between frames by the sampling time (1/30 s). While the velocities plotted in Figure 2.1 represent the average of the data, it is important to note that microparticles moved faster or slower depending on uncontrollable factors (location in mucin, diameter variations, etc.) and leads to some differences in velocities for Figure 2.3. This same experimental procedure will also used in experiments shown in Chapter 3 and 4.

To test open-loop directional control of microparticles, the rotational frequency was fixed as a constant (counterclockwise when viewed behind the heading vector, see Fig. 2.2), B_s was set to 2 mT, and θ was incremented by 90° at user-specified time intervals. The proportional controller for 2D closed loop control used the same parameters for frequency and B_s, but θ was governed by,

$$\dot{\theta} = k\Phi, \tag{2.4}$$

$$\Phi = \varphi - \theta, \tag{2.5}$$

where $\dot{\theta}$ is the time derivative of the heading angle, k is the gain parameter, Φ is the difference between the direction of the desired position relative to the microparticle (φ) and the heading angle of the microparticle (θ). For all experiments, in order to ensure a fast response from the controller, k was set to 5. More advanced proportional–integral–derivative (PID) controllers and 3D closed loop controllers will be explored in future work.

For experiments involving static magnetic field incrementation, rotational frequency was fixed at 15 Hz (or 94.25 rad/s unless specified otherwise), the rotation direction of the magnetic field was selected to be counterclockwise when viewed from behind the rotation vector, and θ was set to 0° to ensure propulsion along the x-direction. The static magnetic field, B_s, was swept between -5 to 5 mT in 0.2 mT and 1 mT increments; again, the times between these increments were variable but the individual frames of the recorded videos could be matched to the experimental parameters being incremented. Hysteresis experiments were performed at the same incrementation, but between 2 mT to -2 mT and then back to 2 mT. All microparticles were examined over a minimum of at least 3 trials.

The μPIV data was collected using a Nikon Eclipse TI inverted microscope with a 100× total internal reflection (TIRF) objective. An electron-multiplying charge-coupled device

(EMCCD) camera (iXon 897, Andor Technology) was used to collect video captures at 60 fps. The experimental parameters were the same as the directional control experiments such that B_s = 2 mT and the frequency was 15 Hz under counterclockwise rotation (when viewed from behind the rotation vector). Tracer particles with 200 nm diameter (Thermo Scientific, Fluoro-Max, G200) were mixed in a ~0.2 mg/ml concentration with the mucus medium and dispersed through vortexing. Due to experimental limitations, most of these experiments were performed close to the boundaries of the sample chamber, which led to both exaggerated transverse rolling translation (Fig. S3) and reduced propulsion velocity [Fig. S1 (b), Fig. S2]. The videos and extracted velocity flow fields were analyzed using both LaVision DaVis PIV software and MATLAB. Individual videos were converted into a series of still images where each image represents a single frame in the video. First, a PIV time series operation was performed to create velocity vectors for each individual frame. The velocity vectors from the individual frames were averaged over frames over the time periods of the videos up to a selected time (usually 20 seconds). Flows for the selected times of the experiments are presented in Fig. 2.4 and in Appendix Section 12; numerical information for all μPIV experiments is tabulated in Appendix Section 13. Magnetic fields used to rotate the microparticles for these experiments were generated by a MagnebotiX magnetic field generator (MFG-100-i), which could produce rotating magnetic fields and static magnetic fields comparable to the approximate Helmholtz coil system discussed.

CHAPTER 3

HETEROGENEOUSLY FLAGELLATED MICROSWIMMER BEHAVIOR IN VISCOUS FLUIDS

3.1 Introductory Remarks

The rotation and bundling of flagellar filaments are the primary means of locomotion by several types of bacteria[85]. Flagellin subunits, which make up the flagellar filaments, are naturally self-assembling and can polymorphically transform[86,87] based on external stimuli such as pH[88], physical stress[89], and physiochemical changes within the surrounding environment[90]. Utilizing these flagella to create simple and efficient artificial microswimmers will allow for environmental adaptation and sensing. Without the onboard motors commonly found in bacteria, flagella have to be chemically attached to magnetic microparticles so they can be rotated using externally applied magnetic fields; these fields induce a torque analogous to the ones produced by the onboard motors. Microparticles by themselves are incapable of propelling by pure rotation within Newtonian fluids as demonstrated in Chapter 2, since they lack the flexibility and chirality necessary for propulsion in low Reynolds number environments[24,25,91]. The addition of a flagellar surface coating explicitly breaks the symmetry of the microparticle and allows for meaningful propulsion when exposed to rotating magnetic fields.

Significant research has already been done documenting the isolation and repolymerization of bacterial flagella[92,93]. In previous work, polymorphic transformations were induced to understand how nanoswimmers, attached with a single flagellum, propelled using different coil forms[94]. These same nanoswimmers were also templated with nickel and titanium to improve responsiveness to applied magnetic fields and demonstrate biocompatibility[95]. Bacteria-inspired dumbbell microswimmers were fabricated by linking a microparticle with a magnetic nanoparticle

using a flagellar filament[96]. As opposed to having a single flagellum attached to a magnetic microparticle, a surface coating of flagella can be more advantageous, allowing for reliable fabrication of microswimmers and enabling diverse motion modes. The work presented here will investigate the propulsion characteristics of microswimmers formed by functionalizing 2 μm diameter magnetic microparticles (SVFM-20-5) with a surface coating of flagellar filaments. These microswimmers were investigated for their responsiveness to rotational magnetic field actuation, their comparative performance in Newtonian solutions of different viscosity, their

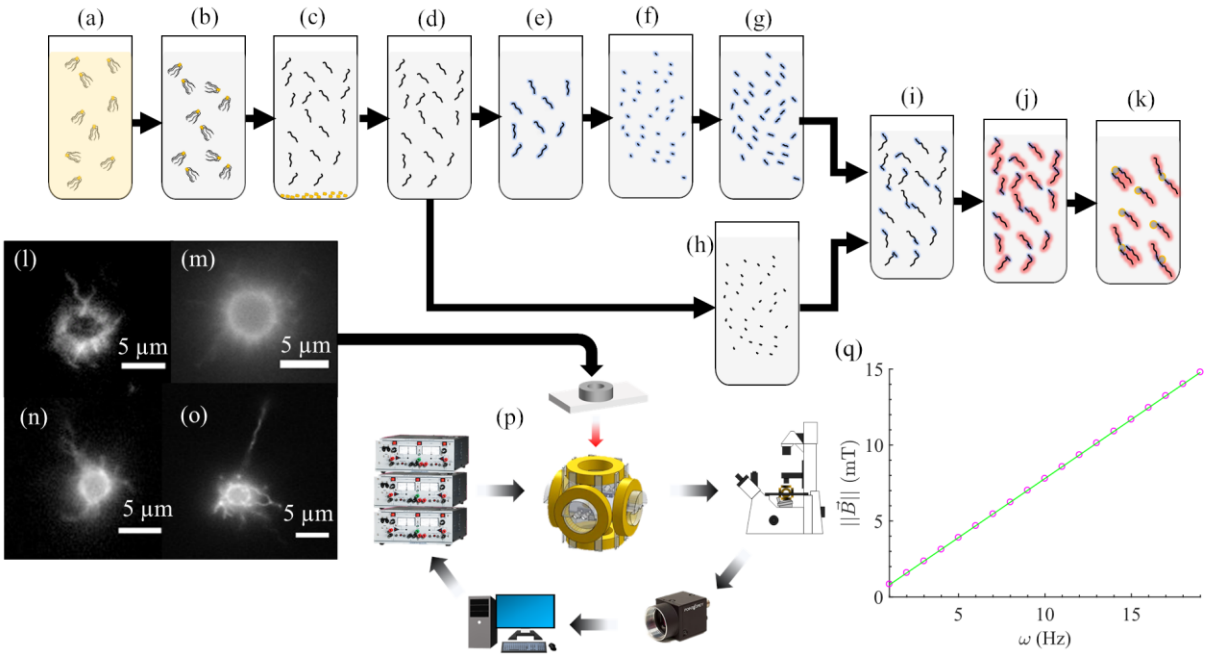

Fig. 3.1. Fabrication of flagellated microparicles. (a) *S. typhimurium* were concentrated from a 10 L culture medium into a single solution through repeated centrifugation and resuspension. (b) *Salmonella* are pelleted and resuspended in polymerization buffer. (c) Flagella were sheared from the bacterial bodies and bacterial bodies were pelleted through centrifugation. (d) Flagella were purified through centrifugation. (e) About 20% of flagella were separated and coated with a NHS-Biotin complex. (f) Biotinylated flagella and (h) non-biotinylated flagella were depolymerized into flagellin monomers. (g) Biotinylated flagella were concentrated into seeding particles. (i) Biotinylated seeding particles were combined with non-biotinylated flagellin monomers and repolymerized into long flagella with biotinylated tips. (j) Flagella were fluorescently labelled using Cy3 dye. (k) Avidin-coated iron oxide particles (2 μm diameter) were introduced and chemically combined with flagella to form microswimmers. (l-o) Microswimmers with different distributions of flagella captured by an EMCCD camera; entire surfaces of microparticles were usually coated with flagella, with the average length of flagella along the surfaces being approximately 8 μm. (p) Overview of experimental setup, with approximate Helmholtz coil systems and computer controlled power supplies that respond to feedback from a camera. (q) Total magnetic field strength graph and its relationship to frequency used during experiments ($|B_r| = 0.5f$). Reproduced from Rogowski, Louis William, et al. "Heterogeneously flagellated microswimmer behavior in viscous fluids." *Biomicrofluidics* (2020) with the permission of AIP Publishing.

ability to perform simple trajectories, and their unique motion modes that occurred as a function of applied magnetic field rotation handedness. An illustration of the fabrication process for the microswimmers can be seen in Fig. 3.1 (a-k), with select heterogeneously flagellated microswimmers shown in Fig. 3.1 (l-o). The experimental set up [Fig. 3.1 (p)] and the magnetic field strength vs. frequency ratio used for these experiments [Fig. 3.1 (q)] are also provided. The processes associated with Fig. 3.1 are elaborated further in the 3.4 Methods section at the end of this chapter. A full description of the magnetic field controller can be found in the Appendix and in the 2.4 Methods section.

3.2 Results

For this study microswimmers were suspended inside 30% NaCl, 0.2% methylcellulose, and 0.4% methylcellulose solutions and then actuated at different rotational frequencies to generate generalized velocity profiles for each medium. The 30% NaCl solution was used to create a neutrally buoyant fluid medium for the microswimmers while replicating fluid properties similar to water. Methylcellulose solutions are well known polymer fluids which increase in viscosity as concentration increases;[48,97] while methylcellulose is known to exhibit non-Newtonian shear thinning behavior at high shear rates, under low shear rates it maintains a Newtonian plateau.[48] For the purposes of these experiments microswimmers were only examined within the Newtonian regime. Using documentation from Sigma Aldrich, the viscosities were estimated to be ~9 and ~19 centipoise (cP) for 0.2% and 0.4% methylcellulose concentrations, respectively. The density of the methylcellulose solutions was high enough to allow microswimmers to remain suspended in bulk solution for prolonged periods of time without noticeable gravity-driven sedimentation. The viscosity of the 30% NaCl solution was assumed to be ~1 cP from literature.[98] Prior to experiments, litmus paper was used to verify that each solution had a neutral pH (~7) to ensure flagellar

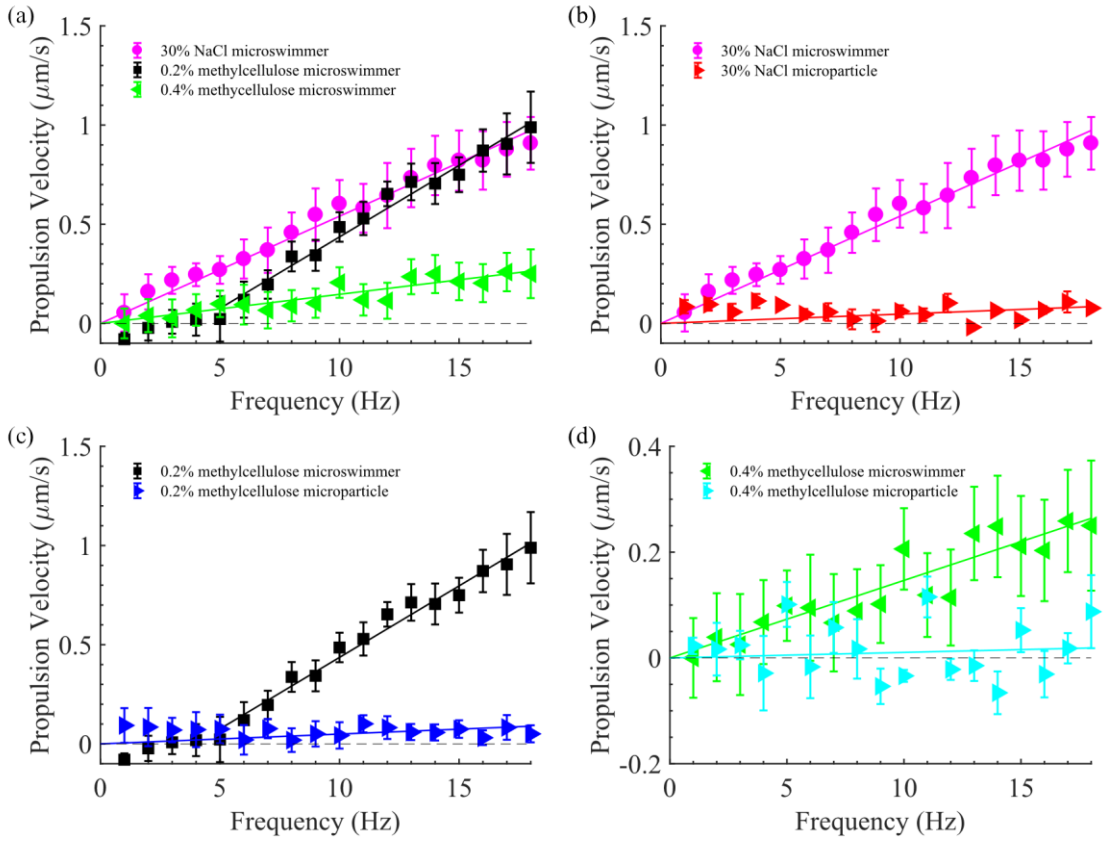

Fig. 3.2. Propulsion characteristics in viscous fluids. (a) Propulsion velocity vs. frequency curves for microswimmers in different fluid mediums. Microswimmers were compared with non-flagellated microparticles under the same frequency range in (b) 30% NaCl, (c) 0.2% methylcellulose, and (d) 0.4% methylcellulose. Error bars represent standard error. Reproduced from Rogowski, Louis William, et al. "Heterogeneously flagellated microswimmer behavior in viscous fluids." *Biomicrofluidics* (2020) with the permission of AIP Publishing.

polymorphic changes did not occur due to pH variations and that all flagella remained normal form in solution. From previous work, flagella were not observed to change coil forms through shear stress during magnetic actuation.[99] Since flagella often coated the entire microparticle surface the exact number of flagella (short and long) was difficult to visually determine; however, through visual estimation, there were usually 12-24 long flagella on each microswimmer, with each having an average length of ~8 μm. The governing equations used to navigate these microswimmers are the same as the ones used in Chapter 2 (Equations 2.2 and 2.3) and can be found in 2.4 Methods. For all experiments, B_s was fixed at a constant value ($\pm$0.2 mT), ω was increased at 1 Hz increments (or 6.28 rad/s), θ was fixed at zero degrees, $\vec{B}$ was rotated in the counterclockwise

direction, and both B_r and $\|\vec{B}\|$ increased linearly with increasing ω ($|B_r| = 0.5f$, where f is the frequency in Hz); a graph of the relationship for $\|\vec{B}\|$ to ω can be seen in Fig. 3.1 (q). The results of these rotation experiments produced the velocity vs. frequency curves found in Fig. 3.2.

The propulsion velocity of microswimmers suspended in 30% NaCl increased linearly with frequency. Microswimmers tested inside the 0.2% methylcellulose solution experienced a consistent propulsion velocity lag at frequencies below 5 Hz, causing velocity to plateau; beyond 5 Hz, however, the velocity of the microswimmers increased linearly with frequency. The 0.4% microswimmers had a linear relationship along the examined frequency range, but their overall velocity was greatly reduced in comparison with the other two fluids. The cause of the velocity lag in 0.2% methylcellulose microswimmers was speculated to be the result of the fluids increased viscosity and possible hindrances from polymer fibers at frequencies below 5 Hz (at this concentration), as it was repeatable between different microswimmers in the same fluid. After this critical point of 5 Hz, the slope of the 0.2% methylcellulose microswimmers velocity profile suggests that if frequencies were to continue to increase, they would overtake the propulsion velocities of microswimmers in 30% NaCl fluid. The most likely reason for this improved performance is the increased interaction with polymer fibers at higher rotational frequencies in 0.2% methylcellulose, as similar performance increases are documented in other low concentration polymer fluids by both microorganisms and artificial microswimmers.[74-76,100-102] To ensure microswimmer propulsion was the result of flagellar coatings, velocity vs. frequency curves for non-flagellated microparticles were also produced. Microswimmers and microparticles rotated in each medium can be seen in Fig. 3.2 (b-d) for 30% NaCl, 0.2% methylcellulose, and 0.4% methylcellulose, respectively. Microparticles displayed no linear velocity relationship with increasing frequency for any of the fluids; with the near constant residual velocity observed being

the result of drift produced by external disturbances. From this, it can be concluded that only microswimmers (microparticles with flagellar coatings) could actively propel inside each fluid medium.

To complement the results of the microswimmer velocity profiles, a two-dimensional mean squared displacement analysis was performed to analyze the behavior of microswimmers under rotating and non-rotating cases. The mean square displacement (MSD) was calculated using,

$$< r_\tau^2 > = \frac{1}{N-\tau} \sum_{i=1}^{N-\tau} [r(t_i + \tau) - r(t_i)]^2 \quad (3.1)$$

where $< r_\tau^2 >$ is the MSD, N is the number of time steps for a given trajectory, τ is the lag time, r is the position vector, and t_i is the i^{th} time increment.[103] For both the rotating and non-rotating cases the MSD profiles were modeled using,

$$< r_\tau^2 > \propto 4D\tau^\alpha \quad (3.2)$$

where D is generalized diffusion and α is the anomalous diffusion exponent; fittings were produced from the ensemble averaged MSD data over multiple rotating microswimmers (at least 3 microswimmers per fluid medium with at least 3 trials each) and non-rotating microswimmers (dozens of individual microswimmers per fluid). Microswimmers were rotated at 19 Hz, while no externally applied magnetic field (static or rotating) was applied during the non-rotating cases. The N for Equation 3.1 was at least 600 for all trials. The smallest increment of τ was 1/30th of a second. The lag time intervals over which the nonlinear fittings were performed for rotating and non-rotating cases were different; the time interval for the rotating case was between 2 and 5 seconds, while for the non-rotating case the interval was between 1/30th of a second and 3 seconds. These intervals were chosen because the MSD for the rotating cases tended to become homogeneous within this range and the MSD for non-rotating cases tended to display unreliable

behavior at larger lag times. A delayed rejection adaptive Metropolis (DRAM) Markov chain Monte Carlo technique was utilized to estimate the coefficients of Equation 3.2 for both rotating and non-rotating cases (see 3.4 Methods).[104] The parameters estimated using this DRAM technique can be found in Table 3.1 and the results of the experiments can be visually seen in Fig. 3.3 for both the rotating and non-rotating cases.

Table 3.1: Coefficients for Fig. 3.3.

Test	$\omega\ (Hz)$	$D\left(\frac{\mu m^2}{s^\alpha}\right)$	α
30% NaCl microswimmer	19	1.16	1.98
30% NaCl microswimmer	0	0.021	0.99
30% NaCl microparticle	0	0.0256	0.97
0.2% methylcellulose microswimmer	19	0.21	1.87
0.2% methylcellulose microswimmer	0	0.0096	0.97
0.2% methylcellulose microparticle	0	0.0127	0.93
0.4% methylcellulose microswimmer	19	0.0418	1.86
0.4% methylcellulose microswimmer	0	0.0033	0.99
0.4% methylcellulose microparticle	0	0.0029	0.88

The behavioral differences between rotating and non-rotating microswimmers can be seen in Fig. 3.3 (a-c) for (a) 30% NaCl, (b) 0.2% methylcellulose, and (c) 0.4% methylcellulose respectively. Microswimmers rotated at 19 Hz displayed ballistic behavior at short lag times with high diffusivity constants and α's much greater than 1, indicating superdiffusive behavior.[105] The non-rotating microswimmers displayed linear behavior in each fluid medium, with low generalized diffusivity coefficients and α's close to 1, indicating diffusive behavior. However, as fluid viscosity

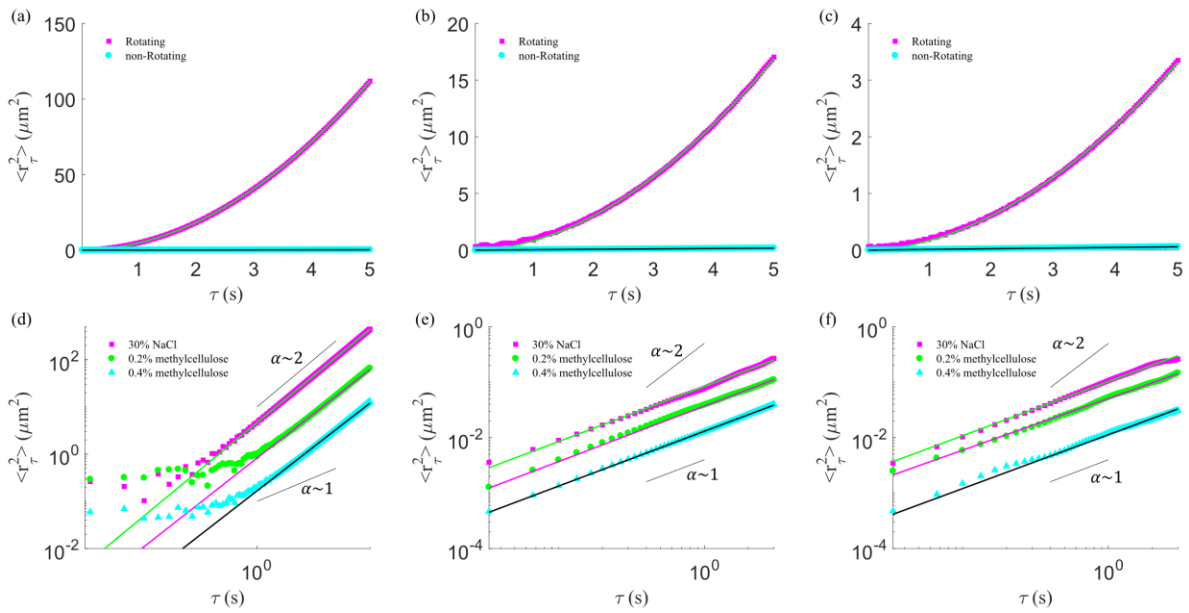

Fig. 3.3. Mean square displacement analysis of flagellated microparticles. (a-c) Mean square displacement curves for microswimmers in (a) 30% NaCl, (b) 0.2% methylcellulose, and (c) 0.4% methylcellulose under both rotating (19 Hz) and non-rotating cases. (d) The mean square displacement of the rotating microswimmers from all three fluid mediums. (e) Mean square displacement of non-rotating microswimmers in each fluid medium. (f) Mean square displacement of non-rotating microparticles (non-flagellated) in all three mediums. The contrasting solid colored lines represent the fits produced from the coefficients estimated in Table 3.1; in (a-f) the green, magenta, and black solid lines correspond to the magenta, green, and cyan data points, respectively. Short solid black lines in (d-f) represent curves showing superdiffusion ($\alpha > 1$) and normal diffusion ($\alpha = 1$), respectively. Reproduced from Rogowski, Louis William, et al. "Heterogeneously flagellated microswimmer behavior in viscous fluids." *Biomicrofluidics* (2020) with the permission of AIP Publishing.

increased, the generalized diffusivity of the rotating microswimmers decreased by almost an order of magnitude; this can be seen graphically when all three microswimmers are plotted together in Fig. 3.3 (d), where each microswimmers MSD curve shifted downward for more viscous fluid mediums. The same effect can be seen in the non-rotating microswimmers in Fig. 3.3 (e) and Table 3.1, where the diffusion coefficient decreased as viscosity increased; while the α's also varied in each fluid medium, they were all consistently very close to 1. Non-flagellated microparticles were also examined in Fig. 3.3 (f) and while their diffusivities tended to be slightly higher in 30% NaCl and 0.2% methylcellulose than those measured for microswimmers, experiments in 0.4% methylcellulose only showed a negligible difference between the diffusivities of microswimmers and microparticles (Table 3.1).

Directional responsiveness of microswimmers was explored to understand the viability of performing user selected trajectories. A proportional controller was used to change the heading angle (θ) in order to properly align the microswimmer with a desired user selected target destination. The proportional controller is the same as the one used in Chapter 2 to investigate the microparticles suspended within synthetic mucus (see 2.4 Methods). For all experiments, in order to reach the desired θ quickly, k was selected to be 5, while the parameters B_s, B_r, $\left\|\vec{B}\right\|$, and ω, were fixed throughout the experiments. Figure 3.5 shows the results of microswimmers performing the trajectories of S, M, and U, the initials of Southern Methodist University, inside a 30% NaCl solution (similar to the experiments in Fig. 2.2). While the microswimmers do not perform each trajectory perfectly, this was expected due to fluidic disturbances and the constant adjustments being made to θ at a sampling time of 30 frames per second (fps). However, the microswimmers did indeed manage to come close to most of the specified points and ultimately generated the

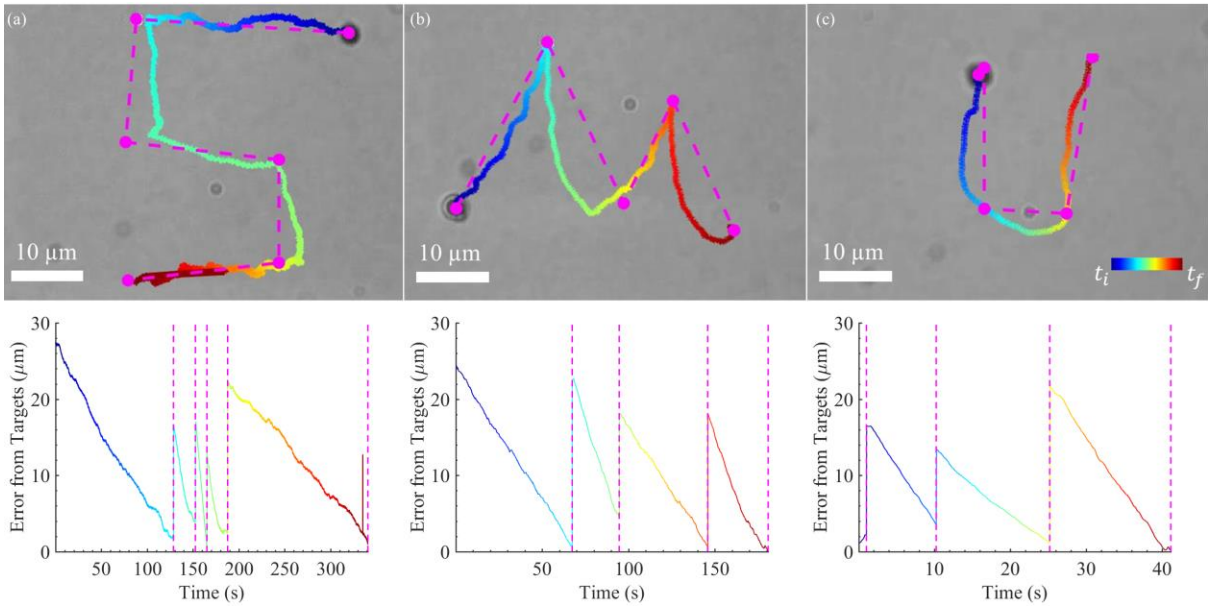

Fig. 3.4. Trajectories of flagellated microparticles. (a-c) User selected path trajectories for S, M, and U. Magenta dots represent the goal position for the microswimmer, while the dashed line represent direct paths between each point. The timings for each trajectory were 360, 180, and 40 seconds for (a-c), respectively. The positional error from the target positions and the microswimmer can be seen in the graphs beneath each trajectory. Vertical magenta dashed lines in the error plots represent target locations from the respective trajectories. Reproduced from Rogowski, Louis William, et al. "Heterogeneously flagellated microswimmer behavior in viscous fluids." *Biomicrofluidics* (2020) with the permission of AIP Publishing.

desired shapes. The positional error of the microswimmers as they approached each of the target points (magenta dots) was plotted below each trajectory in Fig. 3.4. All error graphs show that positional error decayed as the microswimmer approached each respective target point in all three trajectories. The largest error measured between a microswimmer and a target position, before proceeding to the next target position in the trajectory, was ~5 μm.

The magnetic dipoles of the microparticles making up each microswimmer always orient themselves to align with the magnetic field vector ($\vec{B}$) in Equation 2.2 and propel themselves along the direction vector ($\vec{n}$) in Equation 2.3 (see 2.4 Methods). The dipoles were made to rotate clockwise and counterclockwise in the plane perpendicular to the $\vec{n}$ of each microswimmer by changing the sign of ω from positive to negative [see inset of Fig. 3.5 (a)]. While the performance of microswimmers under counterclockwise rotation was consistent (and used for all previous experiments) in causing microswimmers to propel linearly with frequency, clockwise rotation imparted notably diverse frequency responses between microswimmers. Figure 3.5 (a-d) shows the behavior of four microswimmers inside 30% NaCl, examined under both counterclockwise and clockwise rotation, where ω was increased at 1 Hz increments; the microswimmers were first rotated counterclockwise for multiple trials (at least 3) and then switched to clockwise rotation for the remaining trials (at least 3). In all four cases, counterclockwise rotation resulted in a linear velocity profile, while clockwise rotation created anomalous swimming behavior. In (a) and (d) of Fig. 3.5, clockwise rotation resulted in a reduced swimming velocity along the intended direction (positive *x*-direction), while (b) and (c) resulted in frequency induced reversals of swimming direction (FIRSD),[106] which was repeatable between multiple examinations of these microswimmers. These anomalies and FIRSD effects were determined to be related to the bundling and unbundling of long flagella attached to the microswimmers during clockwise rotation. Normal

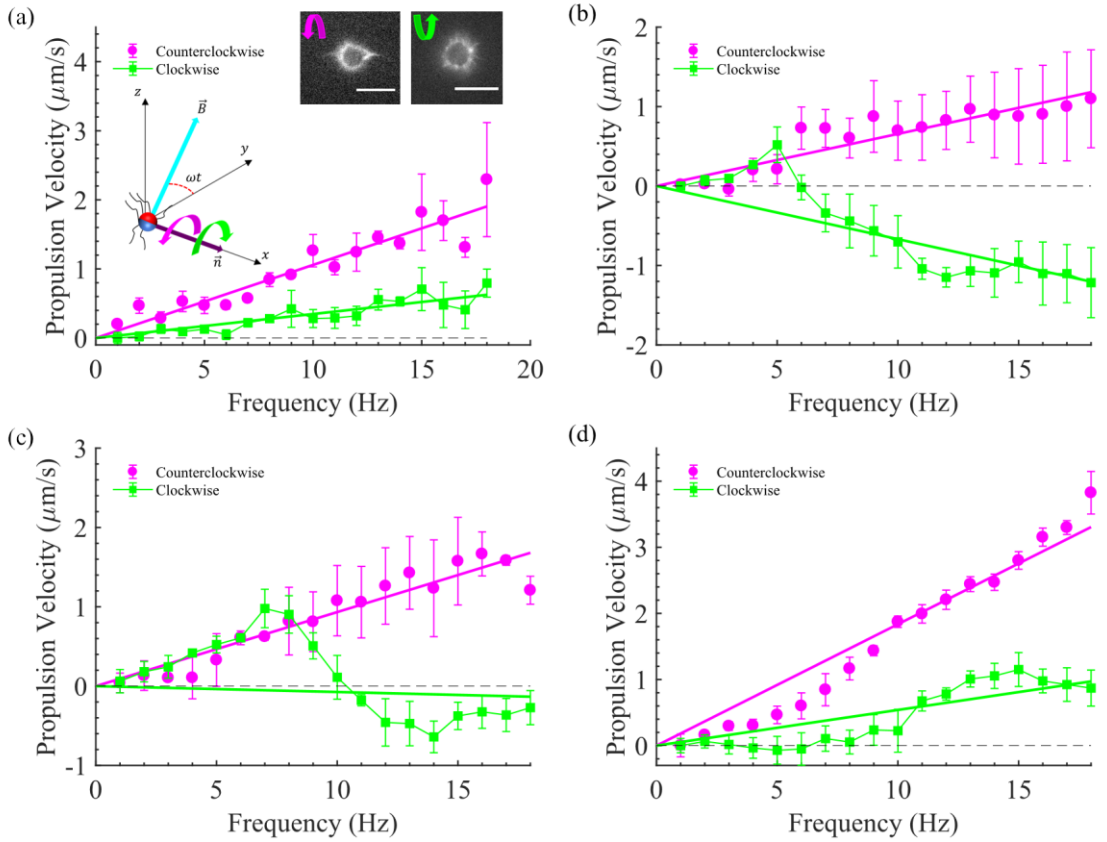

Fig. 3.5. Frequency induced reversal of swimming direction. (a-d) Individual microswimmer performance under both counterclockwise and clockwise rotation. The inset of (a) shows how microswimmers interact with magnetic fields produced from Equations 2.2 and 2.3, where $\vec{B}$ rotates around the *x*-axis, $\vec{n}$ is the direction vector, red and blue hemispheres represent magnetic dipoles, and the magenta and green arrows represent counterclockwise and clockwise rotation, respectively. Fluorescence imaging in the inset of (a) shows that under counterclockwise rotation, flagellar bundling occurs, while under clockwise rotation, the flagella unbundled; scale bars in both images are 10 μm. Dashed lines represent the *x*-intercepts, solid lines represent the fits, error bars represent standard error, and the lines between clockwise data points were used to guide the eye. Reproduced from Rogowski, Louis William, et al. "Heterogeneously flagellated microswimmer behavior in viscous fluids." *Biomicrofluidics* (2020) with the permission of AIP Publishing.

form flagella, used throughout these experiments, is naturally left handed and therefore has the same sense as a counterclockwise rotating magnetic field. Under a clockwise rotation, however, the flagella are opposite to the sense of the rotating magnetic field, leading to unbundling and reduced motility. For situations with multiple flagella, it has been shown that normal form flagella will naturally bundle together at a rate proportional to the motor frequency,[107] and behave as though they were a single larger flagella, with a thickness equal to the summed radii of the flagella

within the bundle[108] [this bundling would explain some of the performance increases seen with the microswimmer in Fig. 3.5 (d) under counterclockwise rotation, while (a-c) were all otherwise consistent with Fig. 3.2's predictions for 30% NaCl]. While this is not the same kind of bundling experienced by microorganisms, since they have onboard motors for individual flagella filaments, the bundling of flagella attached to artificial nanoswimmers has been reported previously, with notable performance variations before and after bundling.[99] Using a Nikon Eclipse Ti inverted fluorescence microscope (see 2.4 Methods) and a magnetic field controller (MagnebotiX, MFG-100-i), microswimmers were actuated close to the substrate under both counterclockwise and clockwise rotation (5 Hz) to observe bundling and unbundling behavior; instantaneous snap shots of these experiments are shown in Fig. 3.5 (a)'s inset. From these images, it can be seen that flagellar bundles form under counterclockwise rotation at the front and rear of the microswimmer, but under clockwise rotation the previously observed bundles were no longer present. While there may be other factors at work, flagellar bundling and unbundling reasonably explains the diverse behavior observed during these experiments.

3.3 Discussion

The reliability of heterogeneously flagellated microswimmers inside fluids of different viscosities was demonstrated. Unlike other microswimmers previously developed in literature, which often rely on complex fabrication techniques, the presented microswimmers were stochastically assembled by mixing biotinylated flagella with avidin-coated microparticles. The assembled microswimmers were capable of performing consistently in various fluid mediums despite their inherent heterogeneous flagellar surface coatings. Microswimmers inside both 30% NaCl and different methylcellulose concentrations were demonstrated to be linearly dependent on applied rotational frequency, however, microswimmers in the 0.2% methylcellulose had to first

overcome an initial propulsion velocity lag, present at frequencies below 5 Hz, before being able to maintain a linear velocity profile; this was suspected to be the result of fluid viscosity and hindrances from polymer fibers at these low frequencies. Microswimmers within 0.2% methylcellulose were shown to outperform microswimmers within the 30% NaCl solution at higher rotational frequencies; this kind of performance increase has been observed previously, in polymer fluids of low concentration, by both microorganisms and artificial microswimmers[74-76,100-102].

Microswimmer propulsion was verified to be caused solely by the attachment of flagella, since non-flagellated microparticles displayed no velocity relationship with increasing frequency. Using a two-dimensional mean square displacement (MSD) analysis, both rotating (19 Hz) and non-rotating (0 Hz) microswimmers were observed. Rotating microswimmers had ballistic motion at short time scales and had significantly higher generalized diffusion coefficients than non-rotating microswimmers. The diffusivity of the rotating microswimmers decreased proportionally as the viscosity of the surrounding fluid medium increased. Interestingly, during the non-rotating scenario, microswimmers had reduced diffusivity compared to non-flagellated microparticles, but this will require more dedicated research in the future to fully understand. Based on these results, the flagellar coatings were shown to allow for ballistic behavior under rotation but hindered the diffusivity of microswimmers when experiencing only purely diffusive behavior (Brownian motion).

Microswimmers were demonstrated to perform selected trajectories under proportional feedback control, with the positional error between the microswimmer and the target locations decaying throughout each experiment. Differences between the desired trajectories and the actual trajectories performed by the microswimmers (or other positional errors), can be attributed to

instabilities in the fluid medium and the sampling time of the controller. Finally, microswimmers were shown to exhibit diverse behavior under clockwise rotating magnetic fields, with frequency induced reversals of swimming direction (FIRSD) occurring in some microswimmers. Flagellar unbundling was identified as the cause for this FIRSD behavior and was visualized using fluorescence microscopy. While these FIRSD effects were not always guaranteed, they did display remarkable repeatability between individual microswimmers. Likewise, the guarantee of a linear velocity relationship to frequency of microswimmers under counterclockwise rotation was also demonstrated. Future work will be dedicated to further visualizing the bundling behavior of artificial microswimmers and comparing them with their bacterial counterparts, as well as continuing to modulate the surface distribution of flagella to initiate more controlled FIRSD effects. Additional polymorphic forms of flagellar will also be analyzed to understand the performance differences of microswimmers induced by the different coil forms.

3.4 Methods

Flagella Isolation

The flagella were isolated from *S. typhimurium* (SJW 1103) and repolymerized using methods adapted from Asakusa's original procedures[92,93]. First, *S. typhimurium* was cultured in approximately 10 liters of a modified Luria-Bertani (LB) broth recipe (1.00% yeast extract, 1.00% tryptone, 0.30% glucose, 0.66% dipotassium phosphate and 0.03% monopotassium phosphate in percent by weight). After a 12-16 hours incubation-shaking process (36°C, 130 rpm). The culture media was centrifuged at 3500 relative centrifugal force (rcf) for 35 minutes, where the bacteria in suspension were pelleted to the bottom of the centrifuge tubes; this centrifugal process was then repeated until all the culture media was used. The pelleted bacteria were then resuspended into a 0.01 M potassium phosphate buffer (pH 6.5, polymerization buffer) with a 150 mM of NaCl, and

concentrated together into a single tube with a final volume of 50 ml. This concentrated solution of bacteria was then vortexed for 20 minutes to shear the flagella from the bacterial bodies. The concentrated solution was then centrifuged for 15 minutes at 16,000 rcf, where afterwards the pelleted bacterial bodies were disposed of, while the supernatant containing the flagella was transferred to a new tube. The flagellar solution was then centrifuged at 100,000 rcf for one hour and the flagella were pelleted. The purified flagellar pellet was then resuspended in the polymerization buffer with a final volume of 1.5 ml per pellet; further purifications at 100,000 rcf for one hour were performed as needed. About 20% of the isolated flagella were taken and mixed with EZ-Link^{TM} NHS-Biotin (Thermo Fisher Scientific, 20217) using the standardized process outlined by Thermo Fisher. After 30 minutes, the biotin complex was completely bound to the flagella. The solution was then centrifuged at 16,000 rcf for 15 minutes to remove any excess biotin from the solution. Both the biotinylated and nonbiotinylated flagellar solutions were then placed in a water bath at 65°C for 10 minutes; this step depolymerized the flagella into its constituent flagellin monomers. Both solutions were then centrifuged at 150,000 rcf for one hour to remove any excess proteins or debris. The supernatants containing the monomers were then transferred to new centrifuge tubes. The biotinylated monomers were then introduced into a 2 M sodium phosphate solution of an equal volume (750 µl each) and incubated for 30 minutes in order to turn the monomers into short flagella (seeding particles). The seeds were then introduced into the non-biotinylated monomers, in a 1:5 ratio, and uniformly mixed by vortexing for 5 minutes; they were then left to incubate for 48 hours at room temperature. The resulting repolymerized flagella were between 10-25 µm in length with one of their end points being biotinylated. The repolymerized flagella were then centrifuged at 100,00 rcf for one hour and resuspended using a 0.01 M potassium phosphate (pH 7.5, conjugation buffer) with 150mM of NaCl solution for a total

volume of 1.5 ml. Cy3 dye (Sigma Aldrich, GEPA23001) was reconstituted in conjugation buffer (1.5 ml) and then mixed in a 1:1 ratio with the flagellar solution; 1 M of sodium bicarbonate was added (5% of the final volume) to help the dye attach to the flagella. After 2 hours, the Cy3 labeled flagella were centrifuged at 100,000 rcf and resuspended using the conjugation buffer to a total volume of 1.5 ml. Approximately 5-20 µl of flagellar solution was then placed in a 5 ml centrifuge tube. Avidin coated microparticles were added to the tube in a 1-2 µl solution and gently shaken for 5 minutes within the flagellar solution to ensure flagellated microparticle formation. The avidin-biotin bonding, between the microparticle and the flagellar ends, is the strongest non-covalent bond found in nature[109]. A detailed outline of this process can be found in Fig. 3.1 (a-k). Flagellated microparticles were visualized using fluorescence microscopy and shown in Fig. 3.1 (l-o). The distribution of flagella along the hemisphere was highly random, but it was visually estimated that anywhere from 12-24 flagella were present along the surfaces of the particles with average lengths of about 8 µm. After the fluid medium of interest is added to bring the total volume of the centrifuge tube to 750 - 1000 µl, a portion of the fluid is loaded into a polydimethylsiloxane (PDMS) chamber 3 mm in diameter and 1 mm in height situated on a No. 1.5 glass cover slide (25 $\times$ 30 mm^2). The chamber was then sealed using a smaller No. 1.5 glass cover slide (18 $\times$ 18 mm^2) and placed in the center of the approximate Helmholtz Coil system where it was ready for experimentation (see 2.4 Methods and Appendix).

Fitting of Mean Square Displacement Data

Fittings for mean square displacement graphs (Fig. 3.3) were calculated using a delayed rejection adaptive Metropolis (DRAM) Markov chain Monte Carlo algorithm.[104] Markov chains had a length of 50,000 and only the last 10% of the chain was used to estimate the parameters shown in Table 3.1. A burn-in of 10,000 was used before adaptation occurred using the DRAM

process. No prior distributions or limits were placed on the algorithm as it calculated the parameters for Equation 3.2. The range of data used in the algorithm was 1/30th to 3 seconds for the non-rotating experiments and 2 to 5 seconds for the rotating experiments. The MSD data for 0.2% methylcellulose microswimmer in Fig. 3.3 (e) and the 30% NaCl microparticle in Fig. 3.3 (f) used a modified mean square displacement analysis in order to remove small internal flows; where the process outlined in literature[110] was implemented to equate the start position with the end position. Aside from the two modified cases, the MSD analysis outlined by Equations 3.1 and 3.2 were uniformly applied.

CHAPTER 4

FLAGELLATED JANUS PARTICLES FOR MULTI-MODAL ACTUATION AND TRANSPORT

4.1 Introductory Remarks

Janus particles are typically composed of two materialistically different hemispheres[111,112], allowing for diverse physical interactions and responses to stimuli from the surrounding fluid[113]. For these reasons Janus particles have displayed surprising versatility as enhanced minimally invasive drug delivery platforms[18,114], made strides towards manipulating the processes of biological organisms[115], and have successfully navigated in *in vivo* environments[116]. Most Janus particles rely on chemical catalyzation[113,117] to propel within viscous force dominated low Reynolds number fluid regimes, where specific chemical concentrations are needed to guarantee propulsion[24]. Multiple catalysts exist in literature with one of the most common being platinum (Pt), which is used to greatly accelerate the naturally occurring decomposition reaction of hydrogen peroxide (H_2O_2),

$$2H_2O_2 \xrightarrow{\text{Pt}} 2H_2O + O_2. \tag{4.1}$$

The propulsive force generated from H_2O_2 decomposition is sufficient to propel Janus particles through bulk fluids and at boundaries[117-121]. Catalytic Janus particles were found to have their propulsion velocities inversely proportional with their diameter[122] and proportional to the concentration of H_2O_2 in the surrounding fluid[123]. The morphology of the platinum surface coating and the physical geometries of the Janus particles (and respective surface coatings) were also found to play a role in influencing propulsion direction during catalysis[124,125]. Other methods for propelling Janus particles include light actuation[126], bacterial actuation[127], enzyme enabled

catalysis[128], hydrophobic-hydrophilic interactions[129], and multi-fueled catalyzation[130,131]. While H_2O_2 is toxic in high concentrations (> 9%), the effects from short term exposure are greatly outweighed by the benefits catalytic Janus particles can impart in medical scenarios, and the side effects of exposure can be easily alleviated using intravenous medicine[132-134]. Even so, chemical actuation by itself is not always viable, particularly in regions of the body that possess viscosities much higher than water[121,135], such as in the gastrointestinal tract[136]. In such high viscosity regions, it would be beneficial to have access to another motion mode that is more reliable and can be activated remotely without the presence of specific chemical agents. Rotating magnetic fields have been the actuation method of choice for microrobotics due to their biocompatibility and long-range wireless transmission. Several microswimmers have been developed including achiral magnetic particles[137], flagellated nanoswimmers[94,96,138], helical microswimmers[13], and soft microrobots[139] which have been successfully propelled using rotating magnetic fields. While all these microrobots each have unique performance characteristics, they are all limited to a single mode of actuation. As previously discussed in Chapter 2, a perfectly spherical microparticle cannot self-propel using purely rotational magnetic fields due to their geometric symmetry preventing the necessary time irreversible strokes to swim in low Reynolds number environments[24]. However, by applying a simple geometric surface coating onto the surfaces of Janus particles like we did in Chapter 3, we can create multi-modal Janus particles that can propel using both chemical catalysts and rotating magnetic fields.

Presented here are catalytic Janus particles that were chemically functionalized with bacterial flagella from *Salmonella typhimurium* (SJW 1103). The attached flagella explicitly break the apparent symmetry of the spherical Janus particles and allow for mobility matrices that can efficiently convert applied rotational torques into linear translation[25,32]. These multimodal

microrobots, dubbed flagellated Janus particles (FJPs), can be propelled using either catalytic propulsion from H_2O_2 or through swimming motion induced by rotating magnetic fields. Figure 4.1 (a) presents a generalized schematic of the FJPs while Figure 4.1 (b) shows a compressed *z*-stacked image of an actual FJP observed using an Olympus confocal laser scanning microscope (FV3000) with a 60× objective, where several flagella are attached along its right surface. The distribution of flagella was found to vary heavily between Janus particles due to the stochastic nature of this self-assembly and the non-uniform avidin surface coating that remained after Janus particle fabrication (see 4.4 Methods). Despite this, propulsion was ubiquitous and easy to achieve for FJPs under both motion modes. This is the first time Janus particles possessing both catalytic and swimming propulsion mechanisms have been developed. Janus particles that were physically attached to live bacteria have been explored previously, however, these had to rely on either the random run and tumble of bacteria[140] or chemotaxis[127] to distribute the Janus particles. The FJPs presented here were fabricated to have magnetic properties and were directly controlled using externally applied magnetic fields from an approximate Helmholtz coil system. The subsequent

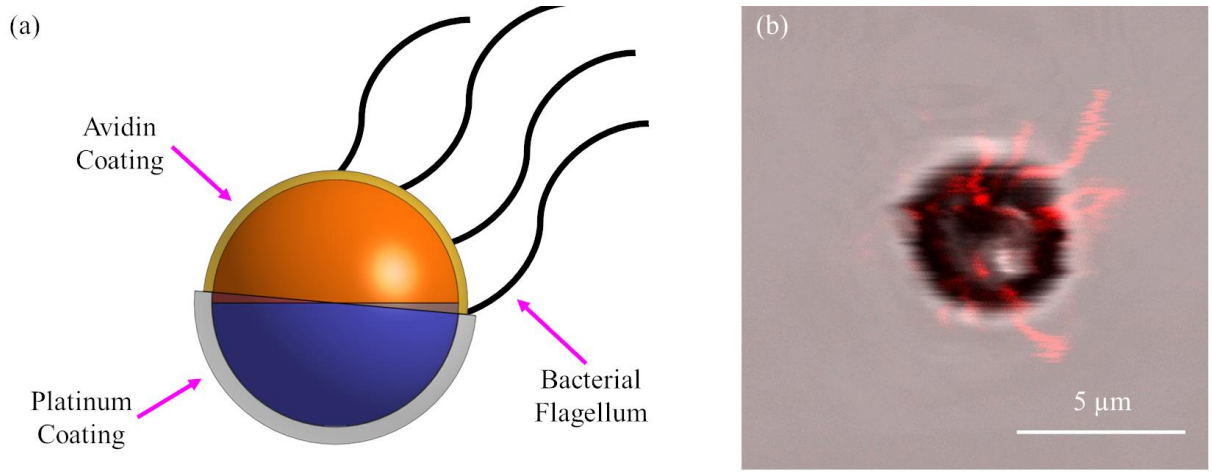

Fig. 4.1. Morphology of flagellated Janus particles. (a) Schematic of flagellated Janus particle. Platinum coating enables catalytic propulsion, while the flagella allow for swimming propulsion. Blue and orange hemispheres represent the magnetic dipoles of the Janus particle. (b) Flagellated Janus particle with flagella distributed along its surface. Flagella are attached through an avidin-biotin chemical functionalization.

sections will demonstrate both the reliable velocity responses and directional control under both motion modes in both Newtonian and non-Newtonian fluids. A full description of the magnetic field controller and FJP fabrication process can be found in the 4.4 Methods section at the end of this chapter.

4.2 Results

After fabrication, both swimming and catalytic propulsion modes of FJPs were investigated separately to quantify their behavior. The FJPs were first suspended inside a deionized water solution, containing 5% H_2O_2 and 5% Tween 20 by concentration, to examine their velocity under catalysis; the Tween 20 was added to prevent FJPs from sticking to the substrate surfaces of the sample chamber and reduce contact friction. Catalytic propulsion was limited to surface motion throughout these experiments due to gravity driven sedimentation from the weight of the particles. The 5% concentration of H_2O_2 was chosen in order to reduce the amount of bubbles that formed within the sample chamber [see Equation (4.1)] and allowed for prolonged experimentation before serious microscopy visualization issues occurred. Once a catalytic propelling FJP was located, it was tracked using image processing (see 4.4 Methods) and its instantaneous velocity was calculated. Using the magnetic field controller [see 4.4 Methods, Fig. 4.7 (b)] the FJPs were directed to follow along a user-determined trajectory within the *x*-*y* plane. Due to heterogeneous differences during fabrication, an offset between the magnetic dipoles and the platinum coating created a randomized propulsion offset angle (Ψ) relative to the static field direction [see 4.4 Methods, Fig. 4.7 (b)]. This offset angle did not noticeably affect the propulsive capabilities of the FJPs during experiments. The results of this analysis produced graphs like the one seen in Fig. 4.2 (a), which shows the moving average velocity (30 point window) over a 52 second time interval for six different FJPs; each FJP had at minimum three independent trials. While each FJP had

slight variations in its velocity as time progressed due to changes in contact surface friction, the velocity profiles were relatively constant overall. For the six different FJPs examined under catalytic propulsion, Fig. 4.2 (b) shows a bar graph displaying their average velocity and standard deviation over a 30 second time period; the average velocity, μ, and the standard deviation, σ, for each observed FJP can be seen in Table 4.1. While the average velocity tended to vary between different FJPs, either because of friction along the substrate or differences in the platinum coatings, they all maintained stable velocities between multiple trials and were able to propel for prolonged periods of time. While the velocities achieved by the FJPs under catalytic propulsion were relatively slow, these velocities can be improved by increasing the H_2O_2 concentration in the surrounding fluid as was shown in previous work[123].

Table 4.1 Average Velocity and Standard Deviation under Catalytic Propulsion

FJP	1	2	3	4	5	6
μ ($\frac{\mu m}{s}$)	0.98	0.69	0.92	1.00	1.19	1.22
σ ($\frac{\mu m}{s}$)	0.049	0.04	0.037	0.039	0.037	0.051

FJPs were next suspended inside of 15-30% NaCl solution, without H_2O_2 present in the medium, in order to test the efficiency of their swimming propulsion. The 15-30% NaCl gave the Janus particles a neutral buoyancy and allowed them to remain far from the boundaries of the sample chamber (≥100 μm). The same approximate Helmholtz coil system was used to generate rotating magnetic fields to actuate the FJPs in conjunction with a superimposed static field [see 4.4 Methods, Fig. 6 (a)]. To understand velocity as a function of rotating magnetic field frequency (f), the superimposed static field was fixed at a constant value during each experiment, while the

rotating magnetic field was increased proportionally with frequency in order to prevent step out ($|B_r| = 0.175f$, see 4.4 Methods)[27]; the frequency range selected for these experiments was between 5 and 50 Hz. Only the velocity along the intended propulsion direction (*x*-axis) was analyzed during these experiments; hereafter this is referred to as propulsion velocity. The tangential velocity was found to be significantly smaller in magnitude, constant between experiments, and had no correlation with frequency; we attribute this to small thermal fluctuations or slight internal flows in the sample chamber (like in Chapter 3). As was discussed in previous

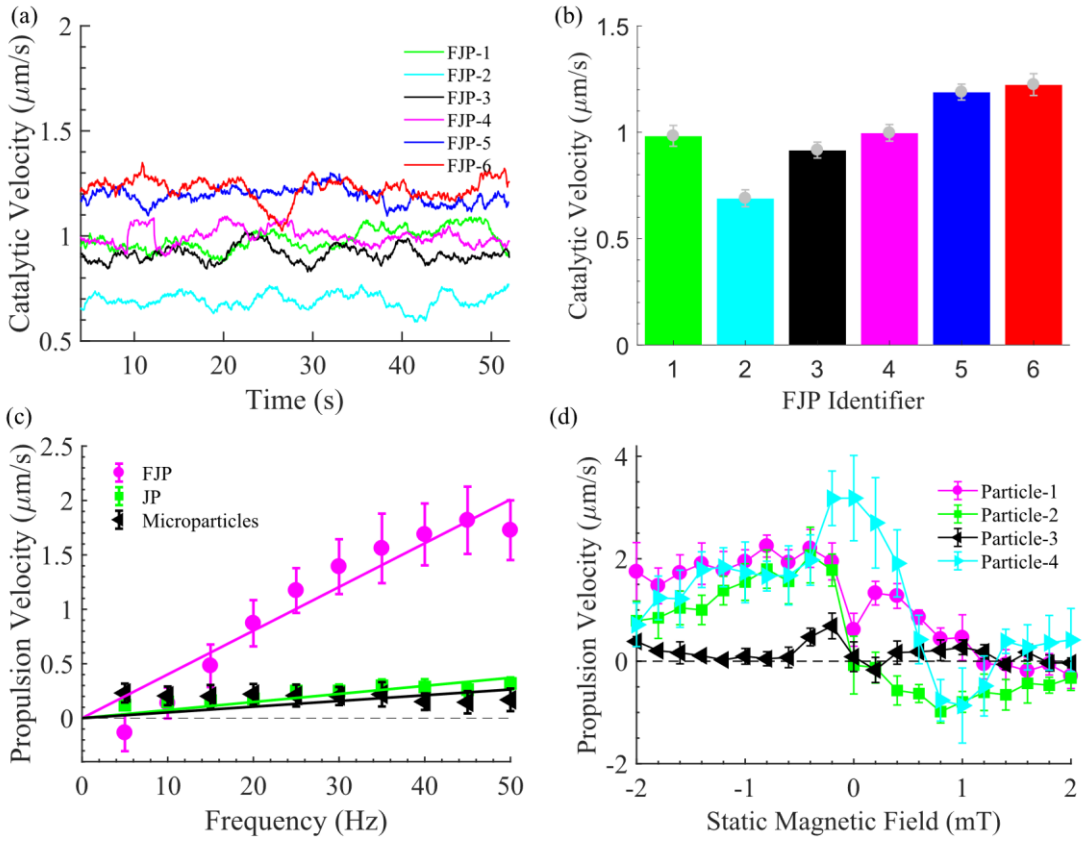

Fig. 4.2. Propulsion characterization of flagellated Janus particles. (a) The moving averaged velocity for an FJP undergoing catalytic propulsion within a 5% H_2O_2 solution (window size of moving average was 30 points). (b) Velocities from six different FJPs [same ones examined in (a)], from at least three trials, with each being 30 seconds long under catalytic propulsion. (c) Velocity vs. frequency curve for FJPs (magenta), un-flagellated Janus particles (JP, green), and microparticles (black) that were actuated using rotational magnetic fields; the solid line represents a fit to the velocity data points and the dashed line represents the *x*-intercept. The coefficients of determination (r^2) were 0.92, 0.33, and -14.52 for FJPs, JPs, and microparticles, respectively. (d) FJPs were rotated between 40-45 Hz under different static magnetic fields. As static magnetic field is altered, the propulsion velocity of each FJP is affected differently, with some being able to switch propulsion directions and others experiencing reduced velocities.

work (Chapter 3), the coil forms of the attached flagella remained normal[89] in these salt concentrations and did not change form as shear rate increased[32]. The random distribution of flagella along the hemisphere of the FJPs caused microswimmers to swim either along or against the heading vector [Fig. 4.7 (a)] and was corrected in post processing data analysis such that all FJPs had swimming velocities with the same sign along the rotation axis. The averaged velocity results between six different FJPs, each with at least three trials each, is shown in Fig. 4.2 (c) and the solid green line represents a linear fit of the data. To confirm that propulsion was being caused solely by the attached flagella (same as in Chapter 3), control experiments involving magnetic microparticles and un-flagellated Janus particles of 4 μm diameter were performed. The magnetic microparticles did not exhibit any correlation with frequency but did experience a small and near constant velocity, which we can attribute to slight internal flow; this is in good agreement with literature predicated symmetry limitations[24,25] and with the results presented in previous chapters. Examining un-flagellated Janus particles did reveal that some Janus particles could propel even without a flagellar surface coating being present, but these were rare occurrences; the most likely explanation for this is that during the fabrication process (see 4.4 Methods), small non-uniform platinum geometric irregularities fixed themselves onto the microparticle surfaces', and thereby explicitly breaking symmetry. While this can result in a weak correlation with frequency, the application of a flagellar functionalization guaranteed the propulsion of FJPs under rotating magnetic fields and created a stronger correlation with frequency during the same experiments. The extra source of geometric irregularity increases the probability of propulsion among individual flagellated Janus particles.

While swimming behavior was achievable for all FJPs examined, with their overall velocity profile being mostly linear with frequency, they all tended to develop a velocity plateau

at higher frequencies. This nonlinearity can be seen at after 40 Hz where the individual velocity points have a different slope than the rest of the data set. One reason these nonlinearities could be present is due to the offset of the flagellar hemisphere from the magnetic dipoles, which is randomly caused during the fabrication process (see 4.4 Methods). To verify this, a superimposed static field was iterated between -2 to 2 mT in 0.2 mT increments while the FJP was rotated constantly at 40 or 45 Hz. The static field altered the pitch of the FJPs dipoles about the heading vector [Fig. 4.7 (a)] and induced a small secondary rotation about the axis of the dipoles. As seen in Fig. 4.2 (d), the velocity behavior of FJPs rotating at a constant frequency changed significantly under different static fields. In some cases, the FJPs reversed swimming direction or achieved optimal propulsion at different static fields. These velocity vs. static field curves varied considerably between individual FJPs. The static field can be used as a parameter in the future to allow for the optimization of individual propulsion velocities or could enable non-homogeneous swimming behavior within swarms of FJPs being actuated under the same globally applied rotating magnetic field input. This is not the same effect that was documented in Chapter 2 [Fig. 2.3] for spontaneous symmetry breaking propulsion, as the propulsion velocity of the FJPs in Fig. 4.2 (d) dynamically changed as the static field was iterated instead of switching between one of two different propulsion states.

A two-dimensional mean square displacement (MSD) analysis was performed to compare both catalytic and swimming propulsion modes of FJPs. The two-dimensional mean square displacement was calculated using,

$$< r_\tau^2 >= \frac{1}{N-\tau}\sum_{i=1}^{N-\tau}\big(r(t_i+\tau)-r(t_i)\big)^2 \qquad (4.2)$$

where $<r_\tau^2>$ is the MSD, N is the number of time steps for a given trajectory, τ is the lag time, r is the position vector, and t_i is the i^{th} time increment[103]. For both the rotating and catalytic propulsion cases the MSD profiles were modeled using,

$$< r_\tau^2 > \propto \ 4D\tau^\alpha \tag{4.3}$$

where D is generalized diffusion and α is the anomalous diffusion exponent; both terms were fitted from positional data collected from FJPs under both swimming and catalytic propulsion, using a delayed rejection adaptive Metropolis (DRAM) Markov Monte Carlo technique[104]. These are the same equations used in Chapter 3 but are re-stated here for clarity purposes. The smallest lag time was 1/30th of a second and N was at least 300 for both propulsion modes during experiments. Fittings for both propulsion modes were obtained with a range of lag times between 1 and 5 seconds using the DRAM technique, where no prior distributions were set for either D or α, and a chain length of 100,000 iterations was utilized with no burn in time; the average of the last 10%

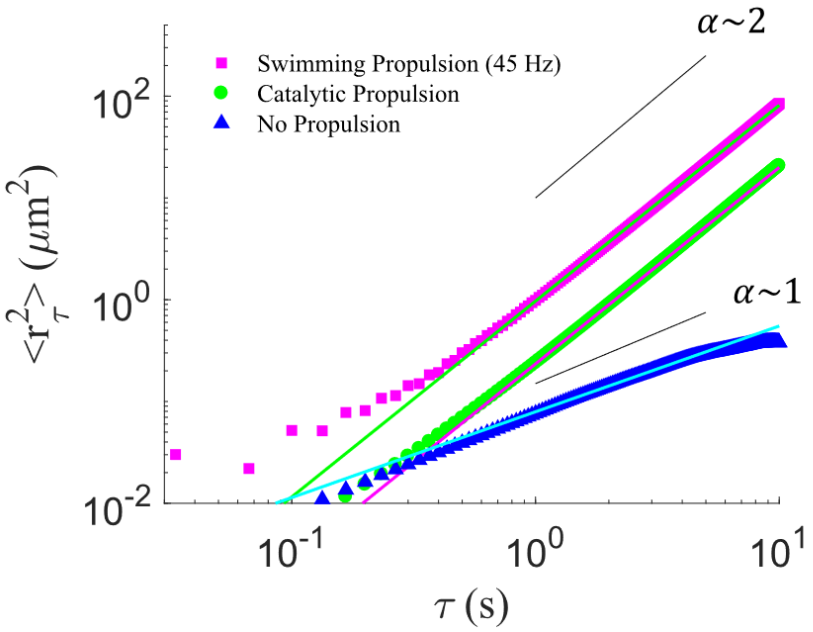

Fig. 4.3. Mean square displacement for a flagellated Janus particle under both rotating and catalytic propulsion. Colored solid lines represent fittings to Equation 4.3 for swimming propulsion (FJPs, green), catalytic propulsion (FJPs, magenta), and no propulsion (microparticles, cyan), respectively. Short black lines represent example MSD profiles for the indicated anomalous diffusion exponents.

of the chain was used to estimate the two parameters for each propulsion mode. The results of the MSD analysis can be seen graphically in Fig. 4.3, which shows the MSD profiles for both swimming (45 Hz) and catalytic propulsion, as well as the results from non-propelling microparticles. Three FJPs were examined under rotation, six FJPs were examined under catalytic propulsion [same ones used in Fig. 4.2 (a-b)], and seven ferromagnetic microparticles (4 μm diameter) were examined under pure Brownian motion conditions with no applied magnetic fields to compare as a control; all particles examined had at least 3 independent trials each.

The estimated generalized diffusion coefficient for the swimming propulsion was 0.24 $\left(\frac{\mu m^2}{s^\alpha}\right)$ and the anomalous diffusion exponent was 1.92. The estimated generalized diffusion coefficient for the catalytic propulsion was 0.06 $\left(\frac{\mu m^2}{s^\alpha}\right)$ and the anomalous diffusion exponent was 1.93. The estimated generalized diffusion coefficient for the zero-propulsion scenario for microparticles was 0.02 $\left(\frac{\mu m^2}{s^\alpha}\right)$ and the anomalous diffusion exponent was 0.85; this slight subdiffusive behavior occurred from post processing used to account for slight tracking errors and drift[141]. Both motion modes had comparatively similar anomalous diffusion exponents but had almost an order of magnitude difference between generalized diffusion coefficients. The MSD for the catalytic propulsion was consistent at both short and large lag times; while the swimming propulsion displayed a smaller sloped MSD at short lag times and then would later separate from the estimated fit as lag time increased. Despite these differences, both motion modes displayed ballistic behavior since their anomalous diffusion coefficients were greater than 1 and is consistent with the results presented in the previous sections.

FJPs were next examined to determine whether or not consistent directional control was possible using both propulsion modes. For this experiment only the heading angle (θ) was of

interest, with other parameters kept constant. The heading angle (θ) was manipulated using the proportional controller,

$$\dot{\theta} = k\Phi, \tag{4.4}$$

$$\Phi = \phi - \theta, \tag{4.5}$$

with $\dot{\theta}$ being the time derivative of θ, k is the gain, ϕ is the desired heading angle relative from the FJP's current position to the target position, and Φ is the angular difference between the desired heading angle (ϕ) and the actual heading angle of the particle (θ). This is the same controller used in Chapter 2 but is re-stated here for clarity purposes. The equations for this proportional controller are transferable between both motion modes as described by Equations 4.6, 4.7, 4.8, and 4.9 (see 4.4 Methods). The gain, k,was chosen to be 5 throughout the experiments to ensure that θ achieved steady state quickly. The results of four FJPs can be seen in Fig. 4.4, with (a-b) showing the trajectories under rotational magnetic fields with superimposed static fields (50 Hz and 2 mT, 19 Hz and 0.2 mT and $|B_r| = 0.5f$, respectively), and (c-d) showing trajectories under catalytic propulsion with two different offset angles (~ 45° and ~ 0°) guided by a 2 mT static field; the magenta points and dashed lines represent the target destinations and shortest paths, respectively. After the displacement error between the propelling FJPs' centroid and the target point (magenta point) became small, the target point was manually iterated to the next location in the sequence and the FJP would attempt to reach it. FJPs under swimming propulsion were found to easily follow the intended trajectories repeatably and quickly. FJPs under catalytic propulsion were also highly consistent but were prone to experiencing significant variation due to their heterogeneous

propulsion offset angles (Ψ). An example of this can be seen in Fig. 4.4 (c), where the FJP, with a

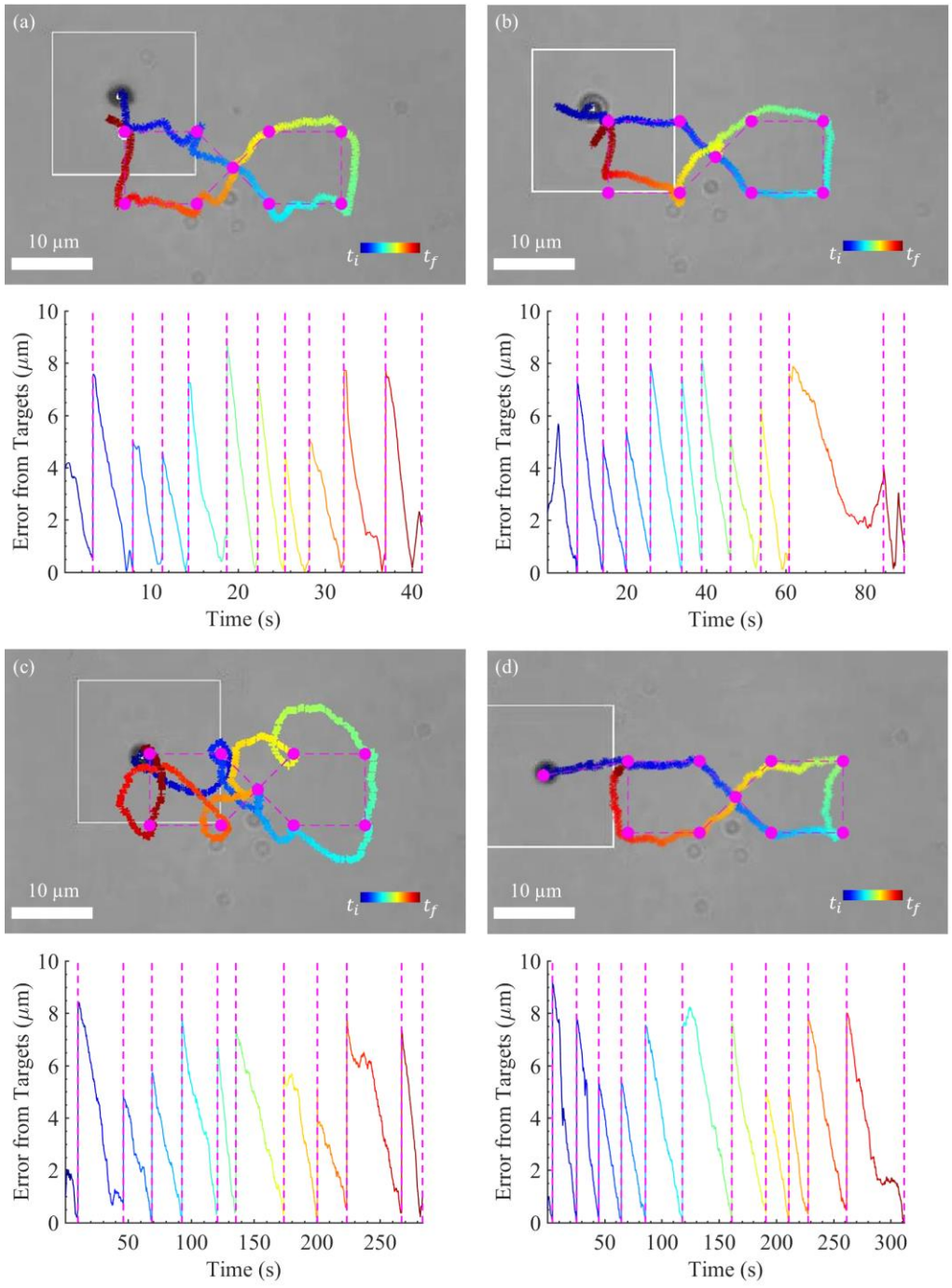

Fig. 4.4. Feedback control and performance of flagellated Janus particles. (a-d) Selected trajectory of a FJP under feedback control using (a-b) rotating magnetic fields and (c-d) chemical catalyzation. Magenta colored dots represent the desired destination points of the FJP, while the dashed magenta line represents the most direct path between points. Included with (a-d) are the error curves with magenta dashed lines separating the target points. The rotation frequency and static magnetic field for (a) was 50 Hz and 2 mT; $|B_r| = 0.175f$. The rotation frequency and static magnetic field for (b) was 19 Hz and 0.2 mT; $|B_r| = 0.5f$. The offset angles for (c) and (d) were ~ 45° and ~ 0°, respectively. The window size for the moving averaged velocity was 100 points for all trajectories.

Ψ of ~ 45°, performed exaggerated parabolic trajectories as it proceeded to each target destination. An FJP with a small Ψ (~ 0°), as seen in Fig. 4.4 (d), could perform the intended trajectory equivalently to the FJPs actuated under rotating magnetic fields [Fig. 4.4 (a-b)]. The FJPs under swimming propulsion in Fig. 4.4 (a-b) took 42 seconds (50 Hz) and 95 seconds (19 Hz), respectively, while under catalytic propulsion in (c-d) the trajectories took 287 seconds and 316 seconds, respectively.

Using the trajectories from Fig. 4.4 (a-d) the error was quantitatively measured as a distance from the intended target magenta points and the actual trajectory performed by the FJPs are displayed as a color bar (same as previous chapters). In all four scenarios the error between the FJPs and each respective target location always decayed to near zero, except for one case in Fig. 4.4 (b) where it could not reach one of the target locations. It is important to reiterate that, despite the missed target point in Fig. 4.4 (b)'s trajectory, the FJP still came within a small error of the other target points within a reasonable amount of time. Consistent with previous work, the FJP with a $\Psi \cong 45°$ could still reach all of the target locations, although having largely curved trajectories [Fig. 4.4 (c)]; however, if an FJP was ever encountered that had a $\Psi > 90°$, the target points would never be reached, as was demonstrated in previous work[142].

Flagellated Janus particles were deployed inside 1% poly (ethylene oxide) solution (PEO, Sigma Aldrich, 189464-250G) to understand their behavior within a known nonlinear fluid. Unlike the Newtonian fluids used previously (saline solution, deionized water), non-Newtonian fluids have viscosities that are shear rate dependent. Using a Discovery Hybrid Rheometer (DHR-3, TA Instruments), a shear sweep was performed using a 40 mm 4° cone-plate geometry under an incremental shear rate of 1 to 1000 (1/s) over three independent trials. The rheology characterization of 1% PEO is shown in Fig. 4.5 (a-b) where both the viscosity vs. shear rate and

the shear rate vs. stress are shown, respectively. Interestingly, the viscosity vs. shear rate curve [Fig. 4.5 (a)] indicates that a shear thickening effect occurs after a shear rate of 100 (1/s) and with the stable shear rate vs. stress curve [Fig. 4.5 (b)] indicating that this behavior is genuine and not the result of fluid being ejected from the geometry under the high shear rates. Literature suggests that 1% PEO should be a shear thinning fluid, however the reported molecular weights were several magnitudes higher than the 100,000 molecular weight of the PEO used in these experiments[143]. The FJPs discussed previously could achieve strain rates between 31.4 to 312 (1/s) under respective rotational magnetic field frequencies between 5 to 50 Hz, well within the range of the observed non-linear behavior of the fluid.

FJPs were deployed within the 1% PEO solution (no H_2O_2) and made to replicate the experiments shown previously in Fig. 4.2 (c-d) to understand how frequency and static magnetic field iteration effected their velocity profiles. The results of these swimming experiments can be seen in Fig. 4.5 (c-d) where there is a strong linear relationship trend present in FJPs actuated in 1% PEO; however, the overall velocity of the FJPs was reduced [in comparison to Fig. 4.2 (c)] from 2 μm/s to 0.87 μm/s at 50 Hz. Examining control experiments for bare microparticles (4 μm diameter, no flagella) suspended in 1% PEO, we observe that there is no propulsion velocity relationship with frequency, with the near constant residual velocities at each frequency being the result of Brownian motion. These results indicate that the spontaneous symmetry breaking mechanism (Chapter 2) was not present in 1% PEO, despite its nonlinear fluid properties. However, when examining the propulsive behavior of Janus particles under a rotating magnetic field, without attached flagellar, there was a strong correlation between velocity and frequency. This correlation is highly unexpected, especially considering previously there was only a weak correlation with frequency present in the Newtonian saline solution. One possible explanation is

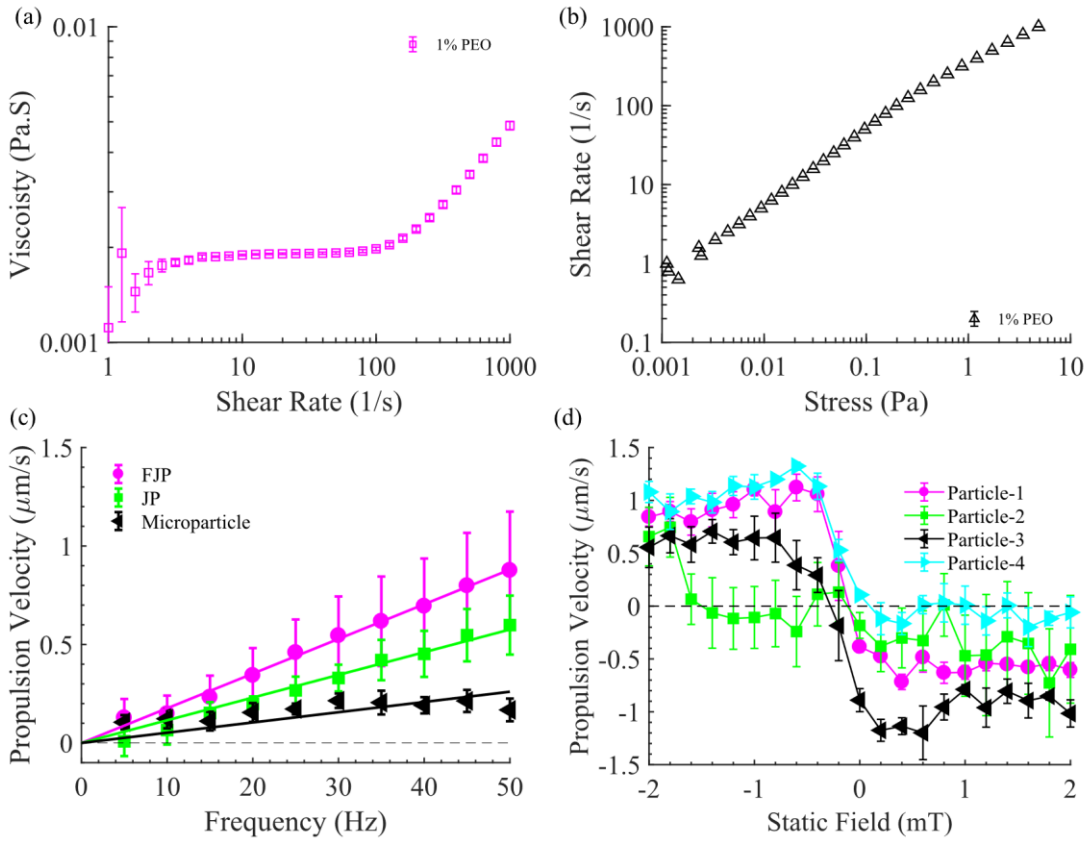

Fig. 4.5. Propulsion in Poly (ethylene oxide) [PEO]. (a) Viscosity vs. shear rate curve and (b) the shear rate vs. stress curve for 1% PEO. (c) Velocity vs. frequency curve for FJPs, JPs, and microparticles actuated in 1% PEO. The r^2 values were 0.99, 0.98, and -0.92 for FJPs, JPs, and microparticles, respectively. (d) Propulsion velocity vs. static field for FJPs rotated at 45 Hz.

that the small propulsive effects from geometric surface deformities on the Janus particles may be being amplified by the nonlinear behavior of 1% PEO, as propulsion was ubiquitous between nearly all Janus particles examined. Catalytic propulsion was not observed in 1% PEO that contained a 5% concentration of H_2O_2; the increased viscosity of 1% PEO was most likely to large for the catalytic propulsion mechanism to overcome.

When examining the static field variation [Fig. 4.5 (d)] for FJPs rotated at a constant frequency (45 Hz), it is clear that FJPs maintain similar relationships with static field variation that were expressed previously in Fig. 4.2 (d), but with a reduced velocity overall, and clear heterogeneities in the curves; most likely the result of differences in the flagella spatial distribution for each respective particle. From these results we can conclude that not only are these FJPs useful

in Newtonian fluids but they can also achieve reasonable performance inside the shear thickening regime of a non-Newtonian fluid; and surprisingly, Janus particles with surface deformities can propel in the 1% PEO solution without the need of flagellar surface coatings.

4.3 Discussion

Flagellated Janus particles (FJPs) were fabricated to have hemispheres consisting of platinum and bacterial flagella; allowing them to be actuated using either catalytic or swimming propulsion. These are the first Janus particles that could be actuated using both fuel and fuel-free propulsion modes interchangeably. Bacterial flagella distributed along one of the FJPs hemispheres allowed for a non-time reversible swimming locomotion to occur when rotated by a magnetic field. When exposed to an H_2O_2 solution, the platinum coating on the other hemisphere of the FJPs acted as a catalyst and initiated catalytic propulsion. It was demonstrated that the velocity of FJPs were mostly linear with rotation frequency, while their velocities under catalytic propulsion were nearly constant with time. Control experiments in Newtonian fluids revealed that bare microparticles had no correlation with frequency while Janus particles (without flagella) only had a weak correlation with frequency, which was most likely the result of surface deformities during fabrication. Under swimming locomotion, a superimposed static magnetic field could be used to adjust the velocity and direction of an FJP rotating at a constant frequency. A mean square displacement analysis was performed to show that both motion modes displayed ballistic behavior at short time scales, with the generalized diffusivity of the swimming propulsion being an order of magnitude higher than the catalytic propulsion during experiments. Using proportional feedback control, FJPs could be made to perform pre-selected trajectories under both motion modes. However, the offset angle of the propulsion vector to the applied static magnetic field could produce exaggerated trajectories for catalytically propelling FJPs. FJPs were suspended inside a

non-Newtonian poly (ethylene oxide) solution [PEO] that was measured to have shear-thickening properties at the actuation frequencies of the FJPs. FJPs were able to propel in PEO using swimming propulsion, retained a linear velocity profile, and could exhibit similar propulsive dependencies on static field like in the Newtonian solutions. While bare microparticles in PEO under the same control experiments did not display any relationship with frequency, the un-flagellated Janus particles did display a high correlation between velocity and frequency. This is almost a direct contradiction between the results shown previously in saline solution but was achievable between all Janus particles examined. Our theory is that the slight surface deformities present on the Janus particles, combined with the nonlinear behavior of the poly (ethylene oxide) solution, are enough to allow free propulsion using rotating magnetic fields. So, in this particular nonlinear fluid, a flagellar surface coating may not be a necessary requirement for swimming propulsion. Catalytic propulsion was not achievable in 1% PEO with a 5% H_2O_2 concentration.

While not fully explored here, flagella are polymorphically transformable under different fluidic conditions, and can allow for different swimming behavior; these differences in performance will be examined in future work for both motion modes. FJPs could eventually be used as an *in vivo* diagnostic tools where fluidic properties are directly related to the conformation of the FJPs flagellar coating. Equipping other surface coatings, such as gold or silver instead of platinum, will allow for thermal propulsion when exposed to laser excitation, and could potentially be used for applications like hyperthermia. Optimizing the flagella distribution along the avidin coated hemisphere will also be investigated. Finally, closed loop 3D control will be explored in future work to expand the capabilities of FJPs for *in vivo* navigation and sensing.

4.4 Methods

Fabrication of Janus Particles

Figure 4.6 (a) gives a brief visual summary of the Janus particle fabrication process, from initial etching of the polystyrene beads, to the multilayer coatings of both platinum (Pt) and cobalt (Co).[144] To start, a 0.5% (w/w) polystyrene bead water solution was prepared using polystyrene beads (Spherotech, IL) that were 5 μm in diameter. The beads were coated as a monolayer on a glass slide whose surface was cleaned using UV-Ozone. The UV-Ozone treatment makes the glass surface hydrophilic, allowing the aqueous solution to spread out evenly along the slide's surface. As the water dried, the beads organized into a monolayer, with each bead touching side by side in a cluster through a self-assembled monolayer (SAM) effect. This can be seen in Fig. 3.6 (b), where the beads were not individually distributed on the surface. Reactive ion etching (RIE) was applied to separate the clustered polystyrene beads from each other by etching the bead surface uniformly [Fig. 4.6 (b)]. O_2 plasma, with a relatively high pressure (250 mTorr) and low power (50 W), was used to gently etch the surface into a round shape;[145] it took about 10 minutes to reduce a 5 μm polystyrene bead diameter to 2.5 μm. To fabricate Janus particles which possessed both characteristics of magnetism and catalytic propulsion, both Co and Pt were coated on the beads using an e-beam thermal evaporator (Temescal CV-8 e-beam evaporator). Multilayer Janus particles were prepared to create stronger magnetism effects [18]; there were five coating layers total in the sequence of Pt 3 nm, Co 3 nm, Pt 3 nm, Co 3 nm, and Pt 3 nm. The Pt and Co were evaporated at a slow rate of 0.02 nm/sec to ensure the high quality deposition. Only half of the surface was coated with platinum, by which the Janus particle decomposes H_2O_2 and causes catalytic propulsion during experiments. The final Janus particles can be seen in Fig. 4.6 (c). The attached beads could be easily detached from the glass surface by gently washing them with water; we also gently stroked the coated surface with a paint brush to help release the particles. The

scanning electron microscopy (SEM) image of the multilayer Janus particles was acquired in Fig. 4.6 (d). The final size of the Janus particles is approximately 2-6 µm.

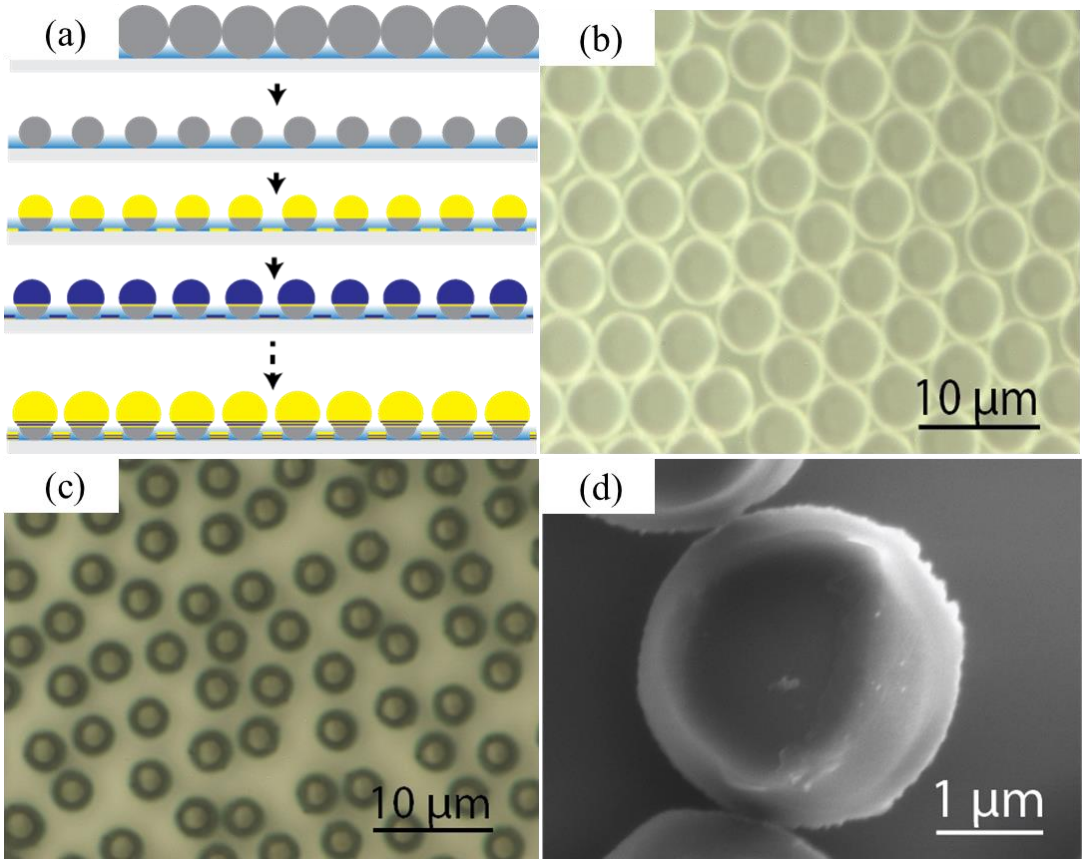

Fig. 4.6: Fabrication of Janus particles. (a) Multilayer Janus particle fabrication steps using Co/Pt layers. (b) Clustered polystyrene beads in a monolayer. (c) Separate multilayer Janus particles after RIE and Co/Pt capping. (d) SEM image of multilayer Janus particle.

Flagellated Janus Particles

An avidin coating along the uncoated hemisphere of the Janus particles remained intact after the fabrication process. While the size of this area was variable, it can still be utilized to chemically attach biotin labeled flagella filaments along the surface of the Janus particles. Likewise, avidin coated microparticles can have entire surface distributions of flagella after chemical functionalization. Using the same technique discussed in Chapter 3 for flagella isolation, the Janus particles were added in a 1-2 µl solution to 5 µl of concentrated flagella and gently

shaken for 5 minutes to ensure Flagellated Janus Particle formation. Flagellated Janus particles were visualized using an Olympus confocal microscope (FV3000) and a *z*-stack was used to produce the image shown in Fig. 4.1 (b). The distribution of flagella along the hemisphere was highly random, but it was visually estimated that anywhere from 1 – 6 flagella were present along the surfaces of the particles with average lengths of about 5 μm, with the longest flagella observed being about 8 μm.

Two control modes for flagellated Janus particles

A triaxial approximate Helmholtz coil system was utilized to generate static and rotating magnetic fields in 3D for all experiments. While the proceeding equations are similar to those in the 2.2 Methods section, they are restated here for comparative and clarity purposes. The swimming locomotion of an FJP relied on rotating and static magnetic fields governed by,

$$\overrightarrow{B_1} = \begin{bmatrix} -B_s \cos\theta + B_r \sin\theta \cos\omega t \\ B_s \sin\theta + B_r \cos\theta \cos\omega t \\ B_r \sin\omega t \end{bmatrix} \tag{4.6}$$

$$\vec{n} = [-\cos\theta \quad \sin\theta \quad 0] \tag{4.7}$$

where $\overrightarrow{B_1}$ is the magnetic field vector, B_r is the amplitude of the rotating magnetic field, B_s is the amplitude of the static magnetic field, ω is the rotational frequency of the field (rad/s), θ is the heading angle in the *x*-*y* plane, t is time (seconds), and $\vec{n}$ is the direction vector. Dipoles of the FJPs align with $\overrightarrow{B_1}$ as it rotates in the plane perpendicular to the direction vector ($\vec{n}$) and can rotate either clockwise or counterclockwise about the direction vector when viewed from behind. Propulsion along $\vec{n}$ indicates swimming is occurring because of the surface coated flagella. As seen in Fig. 4.2 (c-d), the velocity of the FJP can be directly modulated by changing either frequency or the superimposed static magnetic field. To ensure that the dipoles remained in

synchronization with the magnetic field, the amplitude of the rotating magnetic field was scaled with increasing frequency. This scaling was selected to be either $|B_r| = 0.175f$ or $|B_r| = 0.5f$ depending on the what frequency range or magnetic field values are needed for the particular experiment. A lower scaling allowed for frequencies as high as 50 Hz, while the higher scaling allowed for larger magnetic fields but limited frequency to $\leq$ 20 Hz.

When an FJP was undergoing chemical propulsion, the velocity profile of the FJP could not be controlled directly using external stimuli, but the heading direction of the FJP under catalytic propulsion could be controlled by static fields using a simplified version of Equation 4.6 where $\omega = 0$,

$$\overrightarrow{B_2} = \begin{bmatrix} -B_S \cos(\theta) \\ B_s \sin(\theta) \\ B_z \end{bmatrix}, \tag{4.8}$$

$$\vec{p} = [\cos(\theta - \Psi) \quad \sin(\theta - \Psi) \quad 0] \quad . \tag{4.9}$$

The propulsion vector ($\vec{p}$) under catalytic propulsion usually offsets the magnetic field vector ($\overrightarrow{B_2}$) by an offset angle (Ψ), which is randomized during the fabrication process. For all experiments involving closed loop control, Ψ was assumed to be zero, and future work will involve estimating and optimizing Ψ for more accurate control in real time. Figure 4.7 (a-b) show schematics of both swimming and catalytic propulsion modes for Equations 4.6 and 4.7, and Equations 4.8 and 4.9, respectively.

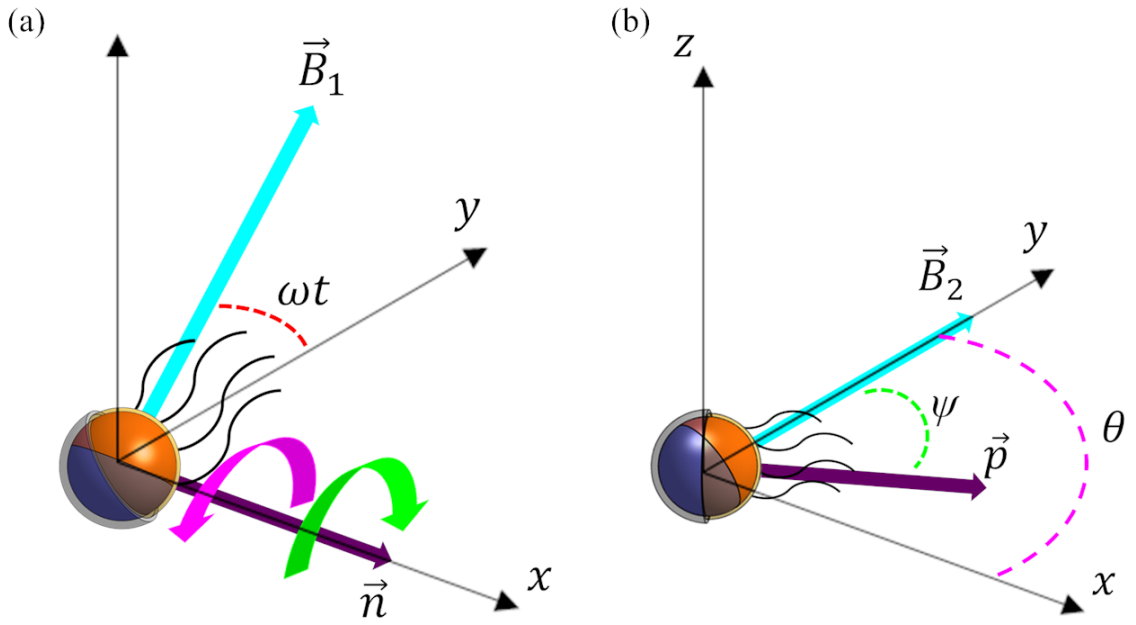

Fig. 4.7. Description of swimming and catalytic propulsion. (a) Janus particle actuated using rotational magnetic fields, where $\overrightarrow{B_1}$ rotates the dipoles around the direction vector $\vec{n}$; attached flagellum will enable swimming motion along $\vec{n}$. When viewed from behind $\vec{n}$, the magnetic field can rotate either counterclockwise or clockwise depending on the sign of the frequency. (b) Janus particle actuated using a chemical catalyzation. The magnetic field, $\overrightarrow{B_2}$, orients the dipoles of the Janus particle, while the chemically induced propulsion propels the particle along $\vec{n}$ at offset angle Ψ, which is the offset of the platinum coating from the magnetic dipoles. The heading angles (θ) were set to 0° and 90° for (a) and (b), respectively.

The Helmholtz coil system was mounted on top of a Leica DM IRB inverted microscope (type 090–132.701) and a 63× objective was used to visualize the FJPs. A complementary metal oxide semiconductor (CMOS) camera (Point Grey, FL3-U3-13Y3M-C) recording at 30 frames per second (fps) was used to record experiments in real time. Programmable power supplies (KEPCO-BOP-5M) were linked to a data acquisition board (National Instruments, DAQ) and interfaced with a customized LabVIEW which could adjust the desired magnetic field parameters. The LabVIEW program could track the centroids of observed particles using image binarization and morphological filters. Post-processing was carried using MATLAB where positional data of the FJPs were converted to velocity data by taking the positional changes of FJPs between individual camera frames. The pixel distance was found to be 0.152 μm/pixel, with the camera resolution being 512 × 640.

CHAPTER 5

CONCLUSIONS

Microparticles are used in a myriad of medical procedures including hyperthermia, magnetic resonance imaging, and targeted drug delivery. In most cases microparticles cannot normally propel using swimming propulsion due to symmetry restrictions in low Reynolds number environments. Demonstrated in this thesis were several mechanisms that enable microparticle propulsion under rotating magnetic fields.

Spontaneous symmetry breaking propulsion was demonstrated to occur in several nonlinearly viscoelastic fluids. Synthetic mucus comprised of mucin from a porcine stomach mimicked a biological fluid and enabled microparticles to propel under rotating magnetic fields. Similarly, a low concentration polyacrylamide solution demonstrated the same spontaneous propulsion behavior. Microparticles suspended in both fluids could propel under both open-loop, closed-loop, and 3D control schemes. By modulating a super imposed static magnetic field, the propulsion direction of the microparticles could be switched between one of two possible propulsive states. The switching behavior of individual microparticles was found to be highly consistent, while interparticle differences were noticeably dependent on the fluid. It is speculated that hoop stresses inside the fluid cause a net squeezing effect that propels the microparticles along their rotation axis, similar to a rod climbing effect; we confirm this experimentally using μPIV and correlate the results with theoretically predicted secondary flows. Rheological characterizations of both fluids indicated that first and second normal stress differences were present at the applied shear rates of the microparticles during rotation. While we have only identified this phenomenon in two fluids thus far, we believe that other fluids with nonlinear viscoelastic properties could

demonstrate this behavior. Likewise, the ubiquity of nonlinear fluids inside the human body makes this propulsion mechanism ideal for improving *in vivo* medical techniques.

Flagellated microparticles with heterogeneous distributions of flagella were demonstrated to propel in different Newtonian fluids with varying viscosities. Since Newtonian fluids do not have the first and second normal stress differences necessary for symmetry breaking, the microparticles geometry had to be broken explicitly. Flagella were isolated from *Salmonella typhimurium* and then chemically attached along the surface of microparticles using an avidin-biotin complex. Flagellated microparticles were shown to have random distributions of flagella but could propel consistently under rotating magnetic fields. Flagellated microparticles were suspended inside saline and methylcellulose solutions, demonstrating decreased propulsion as viscosity increased. A mean square displacement analysis was performed to demonstrate that flagellated microparticles experienced ballistic behavior in all fluids under rotating magnetic fields and purely diffusive behavior without rotation. Flagellated microparticles could propel to user selected target locations under simple proportional feedback control. Finally, depending on the rotation direction (clockwise or counterclockwise) in relation to the coil form of the attached flagella, flagellated microparticles could experience frequency induced reversals of swimming direction (FIRSD). These FIRSD effects were prevalent in flagellated microparticles rotated under clockwise direction and were highly specific to individual microswimmers.

Flagellated Janus particles (FJPs) were next examined which could propel using either catalytic decomposition of hydrogen peroxide or through swimming propulsion using rotating magnetic fields. Unlike flagellated microparticles, flagellated Janus particles only had a small hemispherical distribution of flagella, while the other hemisphere had a platinum surface coating. Under catalytic propulsion, FJPs could propel along the surface of a substrate and propel at a

relatively constant velocity; although velocity could be effected by surface friction. Under the swimming propulsion, FJPs had a mostly linear relationship to frequency and could propel in bulk fluid. Under proportional feedback control, both the propulsion mechanisms could be easily directed to user-specified target locations, and had decaying positional error. Catalytic propulsion often had an offset angle from the applied magnetic field direction which caused the FJPs to experience parabolic trajectories; however, this did not prevent the FJPs from reaching the target points in a reasonable amount of time. FJPs were then introduced into a nonlinear poly (ethylene oxide) solution with measured shear thickening properties; while catalytic propulsion was not achievable, swimming propulsion could still occur, but with a reduced overall relationship to applied frequency. Interestingly, while bare microparticles could not propel in the poly (ethylene oxide) solution using spontaneous symmetry breaking, non-flagellated Janus particles were found to propel under rotating magnetic fields. This is surprising since un-flagellated Janus particles only had a weak correlation with frequency in the Newtonian fluids examined. This indicates that while flagella help the FJPs propel in both fluids, the flagella may not be necessary in some nonlinear fluids, with the non-uniform geometry of the platinum surface coating being just enough to enable propulsion. With these results, the FJPs are the first Janus particles developed that can exhibit two unique propulsion modes that can be used interchangeably.

The simplicity of these propulsion mechanisms makes them readily applicable for *in vivo* operation and can be mass produced easily and cheaply. The spontaneous symmetry breaking propulsion is the most novel of the three, since it relies on fluid properties rather than geometry, and has been previously unobserved in literature up to this point. The flagella surface coatings and catalytic propulsion on the other hand can be used in Newtonian fluids and close to boundary conditions, respectively. These techniques will expand fundamental medical technology,

mechanical engineering, and fluid dynamics research in the years to come. I personally have no doubt that in a few short years this technology will be implemented into life save procedures and expand fundamental concepts; revolutionizing both medicine and having broad societal impact in both the United States and throughout the world.

Future work

While the propulsion mechanisms presented in this thesis are powerful tools for microparticle navigation *in vivo*, the next step will be to apply them into animal models. We have developed a large-scale nested Helmholtz coil system at Southern Methodist University which can produce magnetic fields up to 40 mT and has a working space of $12\times15\times8$ cm^3, large enough to house a sedated full sized rat. Animal tissues and mucus extracted from mice and rats can be used as further proof of concept models to demonstrate each of these propulsive modes. Applying drug carrying compounds (anti-cancer drugs) along the surfaces of the microparticles can be used to demonstrate tumor treatment either *in vivo* or *in vitro*. Finally, a coordinated swarm control mechanism will need to be developed to take advantage of the heterogenic propulsion capabilities of each microswimmer discussed.

APPENDIX

Section 1: Propulsion and Transverse Velocities

In Chapter 2 we observed the propulsion of microparticles through synthetic mucus and polyacrylamide. The propulsion direction is parallel to the rotation axis of the magnetic field. Microparticles were observed to move in both the propulsion direction and the transverse direction perpendicular to the rotation axis. The transverse velocity was influenced by proximity to the boundaries of the sample chamber (2 mm in diameter × 1 mm in height) and was proportional to the rotational frequency of the microparticle. For simplicity, transverse velocity can be thought of as the microparticle rolling like a wheel on a nearby surface as it rotates. Figure S1 (a) shows the propulsion and transverse velocities of 10 µm diameter microparticles for different frequencies in both fluids, with the inset of (a) showing the propulsion and transverse directions. While the

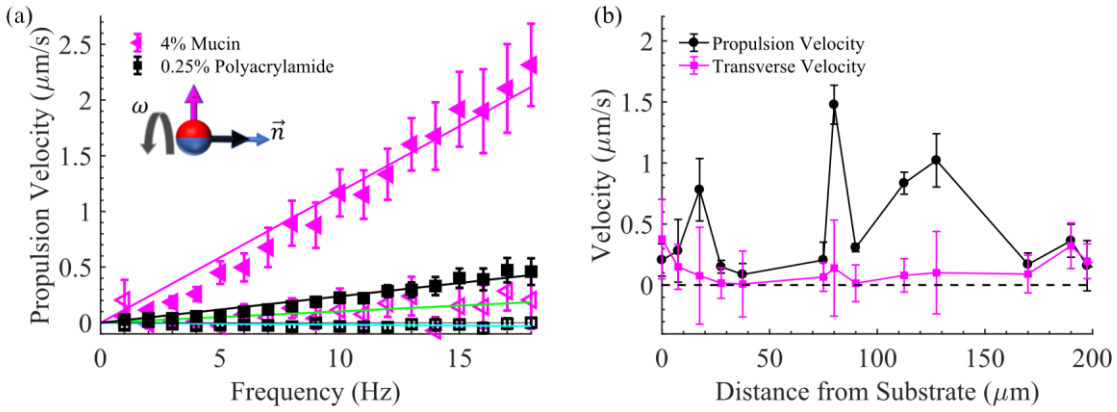

Fig. S1. Propulsion of microparticles in a sample chamber. (a) Propulsion velocity and transverse velocity vs. rotational frequency in 4% mucin and 0.25% polyacrylamide. The inset of (a) shows a microparticle (red and blue hemispheres represent dipoles) rotated under a constant frequency (ω) along a heading direction ($\vec{n}$); black and magenta arrows represent propulsion direction and transverse direction, respectively. Filled symbols represent propulsion velocity while open symbols represent transverse velocity for each fluid. The coefficient of determination (r^2) for the propulsion and transverse fittings (magenta and green solid lines) of 4% mucin were 0.965 and 0.24; the propulsion and transverse velocity fittings of 0.25% polyacrylamide (black and cyan solid lines) were 0.945 and -0.3417. Microparticles were rotated counterclockwise when viewed from behind the heading vector. Error bars represent standard error. (b) Propulsion and transverse velocity vs. distance from the substrate in 4% mucin. Transverse propulsion was significantly increased when the microparticle was in contact with the boundary of the sample chamber; however, transverse propulsion is present at all distances but highly variable at larger distances. Random variations in propulsion and transverse velocity at larger distances are likely due to heterogeneities within the mucus hindering microparticle translation. One particle was tracked at each depth in (b) over a single experiment, with the standard deviation error bars representing the instantaneous propulsion velocity over the course of the experiment.

transverse effect could become significant in the mucin solution, its effect was negligible in the 0.25% polyacrylamide solution. All particles examined were > 100 μm from the boundaries of the sample chamber and six particles were averaged together per fluid with at least 3 trials each. Twenty microparticles had their propulsion and transverse velocities analyzed at different distances away from the bottom of the chamber in 4% mucin [Fig. S1 (b)]. A sharp increase in transverse velocity can be seen when the microparticles were in contact with the bottom of the chamber. Transverse velocity was significantly reduced when the microparticle was in the bulk fluid medium >20 μm from the boundary. Due to the heterogeneous viscoelastic nature of mucus and mucin glycoprotein entanglements, this rolling effect can be experienced by microparticles even if they are far from the surface of the sample chamber, as localized regions of mucus can act as deformable surfaces. The velocity along the transverse direction was considerably less than the propulsion velocities, especially when far from the boundaries of the chamber. Distance from the substrate did not appear to systematically affect the propulsion velocity of individual microparticles, instead we attribute variations in the propulsion velocity to heterogeneities within the mucus.

For rolling motion close to the boundary, it is expected that the transverse velocity should increase linearly with frequency. We therefore tested the frequency dependence of transverse velocity for particles near the boundary (~1 μm). The results are shown in Fig. S2 which compares the transverse velocities of microparticles in both 4% mucin and 0.25% polyacrylamide; each fluid had at least 5 particles averaged together, each with at least 3 trials. Unlike the results shown previously for transverse velocities in bulk fluid [Fig. S1 (a)], microparticles near the surface experienced a linear increase in transverse velocity as frequency increased and at much higher magnitudes. We note that for these microparticles very near the boundary, we generally observed

much smaller propulsion velocities than in bulk fluid, but we did not further explore how boundary effects influence propulsion velocities.

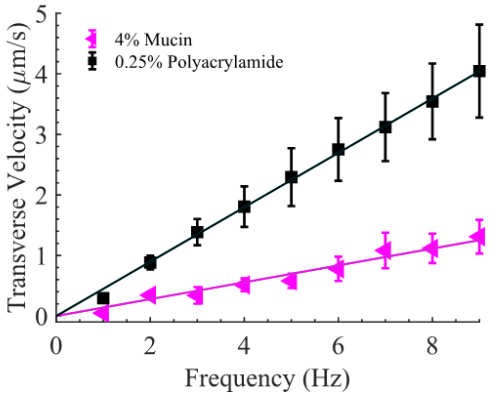

Fig. S2: Transverse velocity vs. frequency for microparticles close to the substrate of the sample chamber. The r^2 values were 0.9634 and 0.9973 for 4% mucin and 0.25% polyacrylamide, respectively. Frequency range was reduced from other experiments to prevent microparticles from rolling out of the field of view. Error bars represent standard error.

Section 2: Static Magnetic Field Manipulation of Microparticles

As discussed in detail in the Chapter 2, the application of a static magnetic field changes the propulsion direction of the microparticles, however, the static field's effect on transverse velocity was not significant. Figure S3 (a) shows a sample experiment of a microparticle rotated at 15 Hz while the static magnetic field increased from -5 to 5 mT in 1 mT increments, during which it initially propelled along the negative *x*-axis and then along the positive *x*-axis after the static field became positive. The transverse velocity caused the microparticle in this experiment to

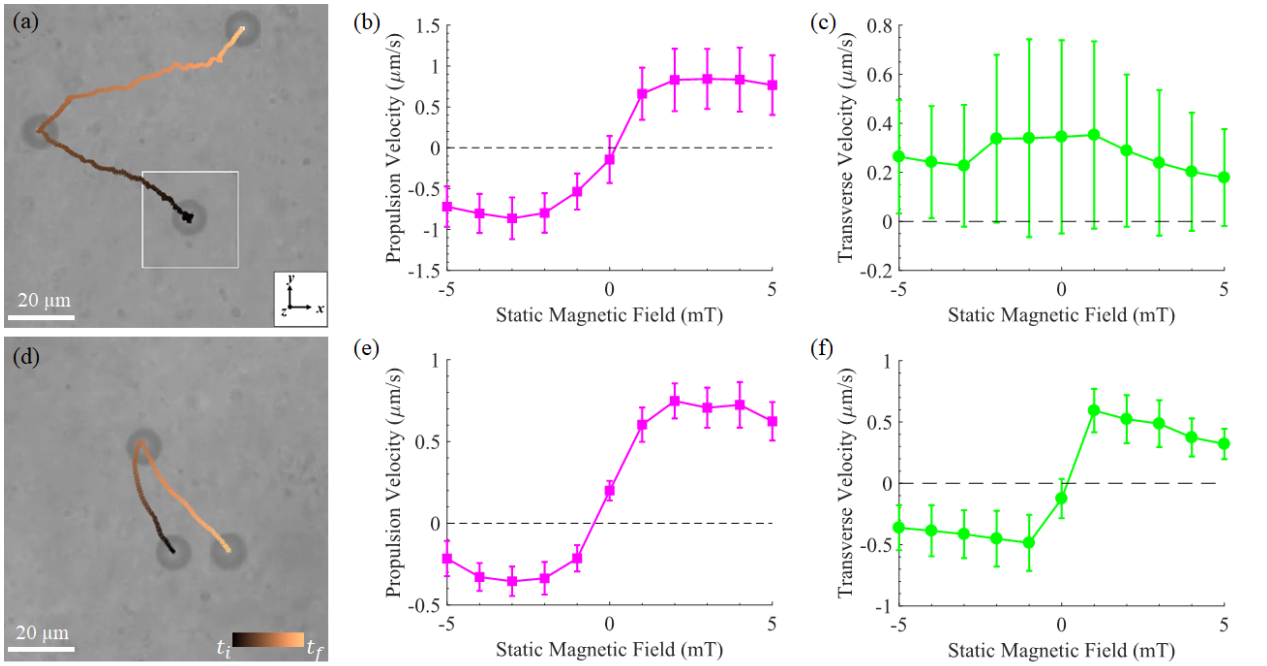

Fig. S3. Combined effect of static field and rotation direction on velocity of 10 µm diameter microparticles. (a) Static magnetic field increased from -5 to 5 mT at 1 mT increments along the heading direction of 0°. (b) The propulsion velocity for microparticles and (c) the transverse velocity for microparticles during experiments like the one shown in (a). While the propulsion velocity is directly related to the static magnetic field, the transverse velocity was unaffected. (d) Same experiment as (a), but at 0 mT the rotation of the magnetic field was switched from counterclockwise to clockwise from behind the heading vector of 0° in the *x*-*y* plane. (e) The propulsion velocity and (f) the transverse velocities for the experiments like the one shown in (d). In this situation, both propulsion and transverse velocities are now affected, with the propulsion velocity only affected by the static magnetic field, while the transverse velocity is affected by the change in rotation direction of the rotating magnetic field. The dashed lines in (b), (c), (e), and (f) represent a propulsion velocity of 0 µm/s. Total time of experiments in (a) and (d) were 67 seconds and 46 seconds, respectively. Error bars represent standard error.

gradually move in the positive *y*-direction and was not affected by the change in static magnetic field. These results are quantified in Fig. S3 (b), which shows the propulsion velocity, and Fig. S3 (c), which shows the transverse velocity as functions of static field; these graphs show the averaged results of four microparticles with each tested under at least three trials. As the static field increases, the average propulsion velocity changes direction at 0 mT [Fig. S3 (b)] but the transverse velocity remains the same. When the rotating magnetic field was switched from a counterclockwise direction to clockwise from behind the heading vector at 0 mT [an example experiment can be seen in Fig. S3 (d)], it was found that the propulsion velocity in Fig. S3 (e) remains similar to Fig. S3 (b), while the transverse velocity in Fig. S3 (f) now changes direction with the change in rotation direction. Together these results clearly show that transverse velocity direction is directly related to the direction of rotation.

When the static magnetic field was increased in 0.2 mT increments, the exact static field at which the propulsion direction flips is revealed to be variable between different microparticles. While the averaged velocities were shown in Fig. 2.3 (c) of Chapter 2, the individual trials can be

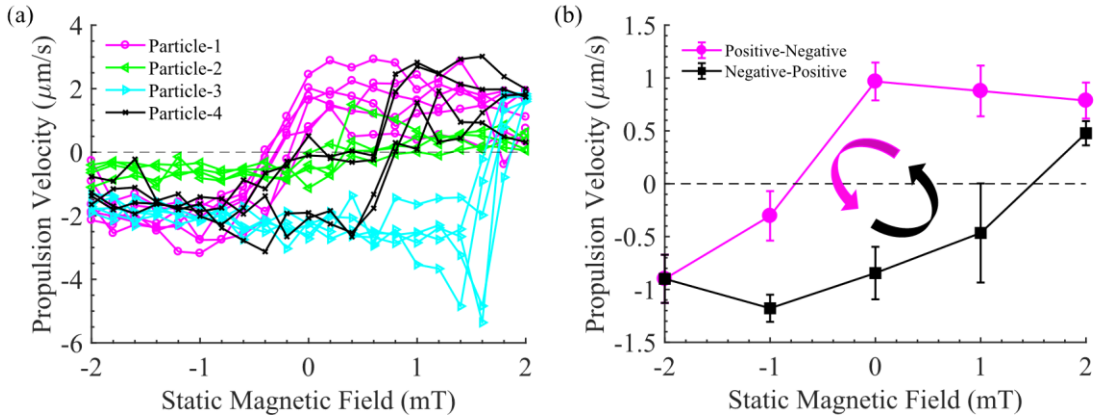

Fig. S4. Comparing velocity profiles under different trials and field increments. (a) Individual trials for microparticles investigated in Fig. 2.3 (c) of the Chapter 2. The static magnetic field flux density necessary to cause a flipping of the propulsion direction was dependent on the specific microparticle as well as its local environment. (b) The hysteresis under 1 mT incrementation for the same microparticle as in Fig. 2.3 (e). Rotational frequency was 15 Hz in both cases. Error bars represent standard error.

seen in Fig. S4 (a), with each microparticle flipping direction at different static magnetic fields. We attribute variations between each trial to heterogeneities present within the fluid and conclude that the switching field also depends on the microparticle's environment. To complement the 0.2 mT incrementation shown in Fig. 2.3 (e) of Chapter 2, the effect of a 1 mT increment on the same microparticle is shown in Fig. S4 (b) over 7 trials. For 1 mT increments, the switching fields of the hysteresis are at -1 mT and 1 mT, while for the 0.2 mT increments shown in Chapter 2 [Fig. 2.3 (e)] they are -1.2 mT and 0.8 mT, respectively.

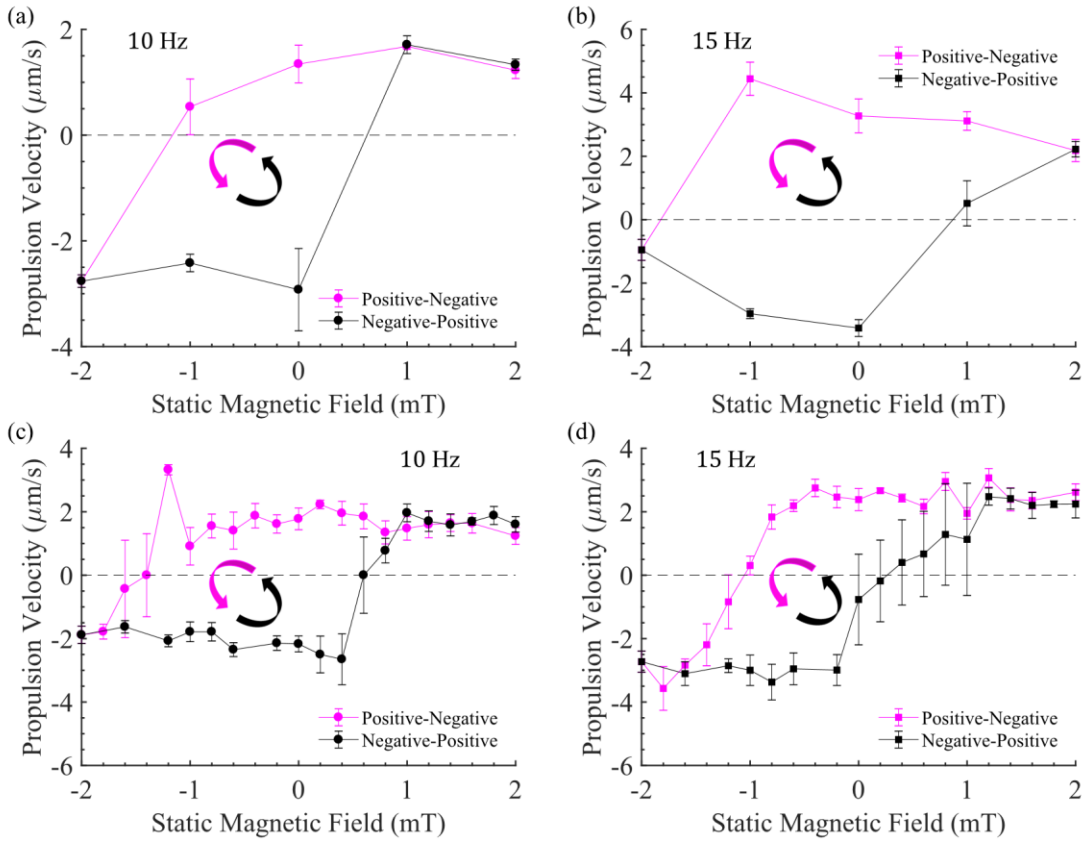

Fig. S5. Hysteresis of a microparticle at different frequencies. The propulsion velocity vs. static magnetic field for a 10 μm diameter microparticle, under 1 mT increments from 2 to -2 to 2 mT, while rotating at (a) 10 Hz and (b) 15 Hz. The propulsion velocity vs. static magnetic field for the same 10 μm diameter microparticle under 0.2 mT increments, while rotating at (c) 10 Hz and (d) 15 Hz. The crossover points (where propulsion of the microparticle flips direction) in each graph were (a) -1 and 1 mT, (b) -2 and 1 mT, (c) -1.2 mT and 0.6 mT, and (d) -1.2 and approximately 0 mT. Error bars represent standard error.

It was observed during experiments that the frequency at which the microparticles rotated affected when their propulsion direction would flip during static field incrementation. In all experiments performed in mucin solution presented in Chapter 2, the microparticles were rotated at a constant frequency of 15 Hz as the static magnetic field was incremented. Here, we describe comparative experiments where the frequency was reduced to 10 Hz. The propulsion velocity exhibited by the microparticle was lower and the behavior of the hysteresis curve from the static field sweep was significantly altered. Figure S5 shows the static magnetic field incrementation from 2 mT to -2 mT to 2 mT under both 0.2 mT and 1 mT increments for two different rotational

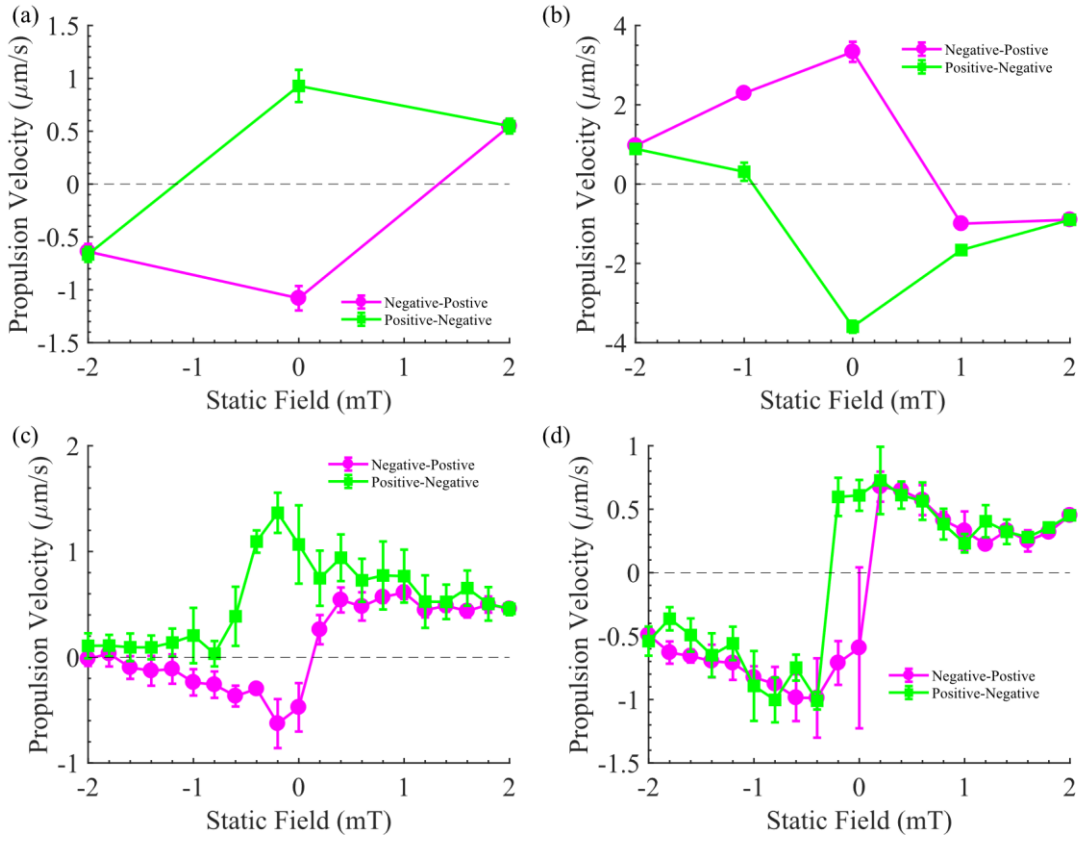

Fig. S6. Hysteresis in 0.25% polyacrylamide. (a-b) Microparticles undergoing a static field hysteresis at 2 mT and 1 mT increments, respectively. (c-d) Two different microparticles undergoing a static field hysteresis at 0.2 mT increments. All microparticles were 10 μm in diameter and rotated at 40 Hz. Error bars represent standard error.

frequencies for the same microparticle [a different microparticle then Fig. 2.3 (e) and S4 (b)], over at least 4 trials per frequency and increment. Thus, rotation frequency can influence the microparticle's response to changing static magnetic fields. We expect that there are heterogeneities within the fluid medium that are also influencing the microparticles behavior, but these are not easily quantifiable at this time.

Static field experiments involving microparticles within 0.25% polyacrylamide did not always result in a hysteresis. This appears to be a frequency dependence as microparticles actuated at 15 Hz could not produce a hysteretic effect, while microparticles actuated at 40 Hz [see Fig. 2.3 (f)] could produce uniform and repeatable behavior. For five microparticles rotated at 15 Hz (4 trials each), no hysteresis was observed, and the behavior was similar to the unidirectional static sweeps in Fig. 2.3 (d). At higher frequencies (40 Hz, where $|B_r| = 0.175f$) hysteresis effects were observed in 4 of 5 particles tested, and for these particles two symmetry breaking propulsion states occur at 0 mT. Figure S6 shows four microparticles, one under a 2 mT increment, one under a 1 mT increment, and two under 0.2 mT increments, each with at least three trials each. In Fig. S6 (a-b) we see there are two distinct propulsive states at 0 mT for each particle that are nearly equal and opposite to each other during hysteresis. In Fig. S6 (c-d) we see that the hysteresis patterns are different for different particles under 0.2 mT increments and were consistent between multiple trials; both also had two unique propulsive states for 0 mT. Thus, consistent with our observations in mucus solution, frequency and static field incrementation are interlinked and can influence how the hysteresis forms (if at all). However, even at a high frequency, some particles did not exhibit two symmetry breaking states; an example of this can be seen in Fig. S7, where a microparticle in 0.25% polyacrylamide had the same propulsion direction at 0 mT static magnetic field on both the forward and backward sweeps.

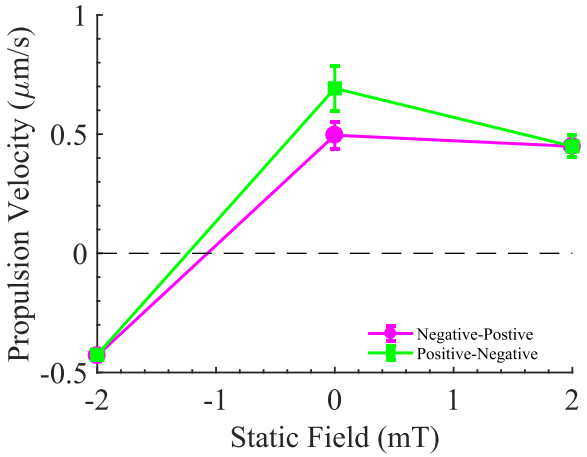

Fig. S7. Attempted hysteresis of a 10 µm diameter microparticle in 0.25% polyacrylamide. This microparticle did not display hysteresis or pair of symmetry broken states when rotated at 40 Hz while magnetic field was changed in 2 mT increments. Error bars represent standard error.

Section 3: Performance Statistics of Selected Trajectories

Microparticles were propelled in the trajectories presented in Chapter 2 [Fig. 2.2 (c-g)] using proportional feedback control described in Eq. 2.4 and Eq. 2.5 of Chapter 2. In the case of these experiments, we targeted two box-shaped trajectories for the microparticles in polyacrylamide, and the letters 'S','M'', and 'U' were targeted, in homage to Southern Methodist University, for microparticles in 4% mucin. Each of the trajectories was defined by several target positions which the microparticle had to reach in order to complete the trajectory. Connecting all of these target positions together in sequence creates the shortest path the microparticles could trace; these paths can be seen as magenta dashed lines in Fig. 2.2 (c-g) with the magenta colored dots representing the target positions. The distance between the microparticle's centroid and the target positions was measured during each frame of the recorded experiment to produce the positional error graphs presented in Fig. S8 (a-e) for Fig. 2.2 (c-g), respectively. In all experiments

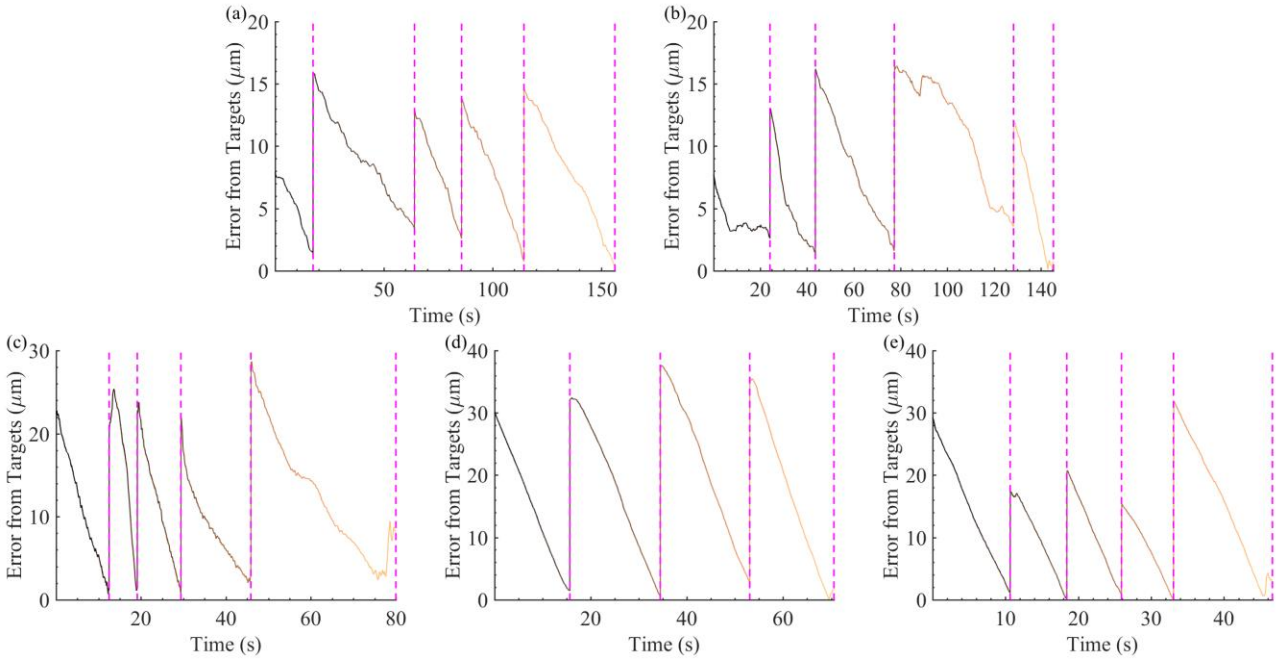

Fig. S8. Feedback control trajectories and performance statistics. (a-e) Represent the error of the microparticles form the target positions (magenta dots) for each trajectory shown in Fig. 2.2 (c-g) of Chapter 2, respectively. The dashed magenta lines in (a-e) indicate the target point the microparticle was attempting to reach.

the error from the target points decayed and the microparticles could come reasonably close to each target position (< 5 μm).

Section 4: 3D Propulsion and Tracking

To approximate the displacement of a microparticle translating in 3D, two different methods were utilized: (1) directly measuring using a microscope focusing knob and (2) measuring the change in pixel area of a microparticle as it changes focal planes. The first method was used to measure a microparticle's distance and velocity as it translated from the bottom of the substrate into the bulk fluid during the µPIV experiments discussed in Chapter 2. The microscope was a Nikon Eclipse-Ti which could precisely track the focal plane in micrometers via a visual display at the front of the microscope. A microparticle, the same one that was examined in the µPIV experiment in Fig. 2.4 (i), was rotated for 10 seconds in the *x*-*y* plane at 15 Hz with a 2 mT static magnetic field using a MagnetbotiX (MFG-100-i) field controller; the distance traveled by the microparticle was recorded from which the velocity was calculated. The results of this experiment are shown in Fig. S9 (b), where the bar graphs show both the distance traveled and the average velocity of the microparticle. The microparticle was clearly seen to overcome gravity and achieve meaningful propulsion behavior in a short time frame. In more complex pathing experiments, a Leica (DM IRB) microscope was utilized with our approximate Helmholtz coil system and a CMOS camera was used to visualize the microparticles as they translated through the medium.

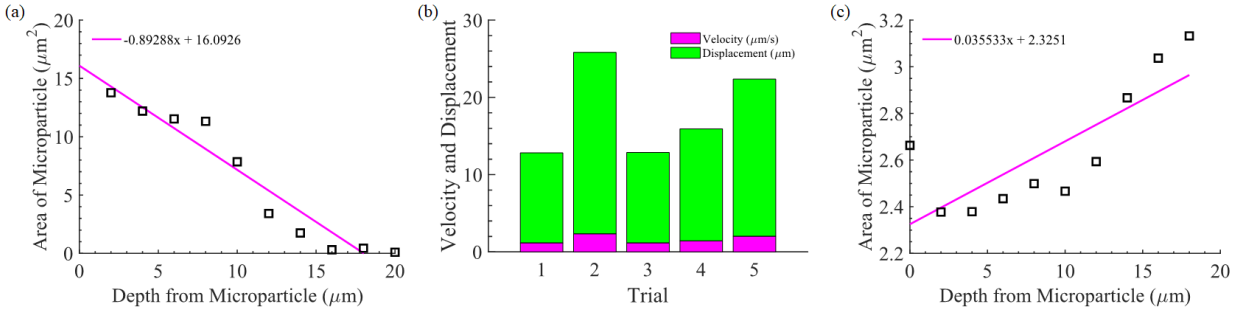

Fig. S9. 3D tracking analysis. (a) Image area of a microparticle as the microparticle translates in the negative *z*-direction. (b) Velocity and distance measured for a microparticle propelling along the positive *z*-direction. (c) Image area as a 2 µm diameter microparticle translates in the negative *z*-direction in 0.25% polyacrylamide.

These microparticles were tracked in the *z*-direction by tracking changes to the pixel area of the observed microswimmer; decreases in pixel area were correlated with decreases in *z*-direction depth (into the page), and increases were correlated with increases in *z*-direction depth (out of the page). A graph showing this correlation can be seen below in Fig. S9 (a). This correlation was used to generate the positional data for the results shown in Fig. 2.2 (h) of Chapter 2 from pixel areas in the videos. Another correlation for a 2 μm diameter microparticle in 0.25% polyacrylamide can be seen in Fig. S9 (c).

While not shown in Chapter 2, microparticles suspended in 0.25% polyacrylamide were also capable of exhibiting 3D propulsive behavior similar to the kind demonstrated in 4% mucin [Fig. 2.2 (h)]. From experiments it was determined that 2 μm diameter microparticles were not as susceptible to gravity driven sedimentation and were used here for demonstrative purposes. Presented in Fig. S10 is a 2 μm diameter microparticle that performed a user selected trajectory in three dimensions with *z*-position approximated using the correlation shown in Fig. S9 (c). The estimated 3D position with time is also presented along with projections in each plane.

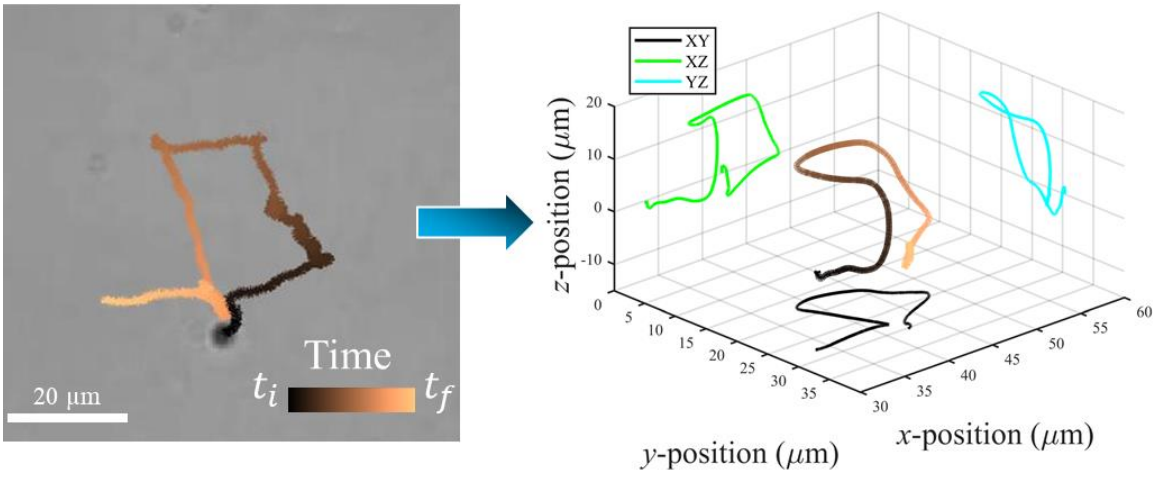

Fig. S10. Three-dimensional tracking of a 2 μm diameter bead in 0.25% polyacrylamide. Total time of experiment was 138 seconds.

Section 5: Rotational Dynamics of Magnetic Spheres with Static Field

Consider a magnetic field that is rotating about the *x*-axis, with static component B_s and rotating component B_r. We work using a basis that is coincident and co-rotating with the magnetic field, so that the magnetic field is $\boldsymbol{B} = (B_s, B_r, 0)$, and its angular velocity is $\boldsymbol{\omega} = (\omega,0,0)$. For a spherical bead with magnetic moment of magnitude m, $\boldsymbol{m} = m(\hat{m}_x, \hat{m}_y, \hat{m}_z)$, the torque exerted on it by the field is $\boldsymbol{N} = \mu_0 \boldsymbol{m} \times \boldsymbol{B}$, where μ_0 is the vacuum magnetic permeability. In the zero-Reynolds number limit, the angular velocity $\boldsymbol{\Omega}$ of a sphere of radius a is proportional to the torque, $\boldsymbol{\Omega} = \frac{3}{8\pi\mu a^3}\boldsymbol{N}$, where μ is the viscosity of the fluid. Combining the above, $\boldsymbol{\Omega} = \frac{3\mu_0}{8\pi\mu a^3}\, \boldsymbol{m} \times \boldsymbol{B}$. Suppose we seek a steady solution, in which the sphere rotates with the field, i.e., $\boldsymbol{\Omega} = \boldsymbol{\omega}$. Since by the properties of the cross product $\boldsymbol{\Omega}$ is perpendicular to $\boldsymbol{B}$, this is only possible if $\boldsymbol{\omega}$ is perpendicular to $\boldsymbol{B}$, i.e., if there is no static component and $B_s = 0$. However, we are interested in the behavior when there is a static component, so we must seek a different solution. It turns out that for $B_s \neq 0$, there exist solutions for which the magnetic dipole $\boldsymbol{m}$ co-rotates with the field, even if the sphere does not. To find these, we set the time evolution of $\boldsymbol{m}$ in the basis rotating with the field to be zero, $0 = \dot{\boldsymbol{m}} = (\boldsymbol{\Omega} - \boldsymbol{\omega}) \times \boldsymbol{m}$, where the relative angular velocity $(\boldsymbol{\Omega} - \boldsymbol{\omega})$ is used since we are expressing $\boldsymbol{m}$ in the basis rotating with angular velocity $\boldsymbol{\omega}$. The result is

$$\dot{\boldsymbol{m}} = m\Omega_s \begin{pmatrix} b_s(1-\hat{m}_x^2) - \hat{m}_x\hat{m}_y \\ -b_s\hat{m}_x\hat{m}_y + (1-\hat{m}_y^2) \\ -b_s\hat{m}_x\hat{m}_z - \hat{m}_y\hat{m}_z \end{pmatrix} + m\omega \begin{pmatrix} 0 \\ \hat{m}_z \\ -\hat{m}_y \end{pmatrix}, \qquad \text{(S1)}$$

where $b_s = B_s/B_r$, and $\Omega_s = \frac{3mB_r\mu_0}{8\pi a^3\mu}$ is the step-out frequency of the sphere when there is no static field.

Solutions for a co-rotating dipole $\boldsymbol{m}$ are obtained by setting Eq. (S1) to zero and solving under the constraint $1 = \hat{m}_x^2 + \hat{m}_y^2 + \hat{m}_z^2$. Typically, there are four solutions, only two of which have purely real components $(\hat{m}_x, \hat{m}_y, \hat{m}_z)$. One of these real solutions has $\hat{m}_x$ pointing in the direction of the static component B_s, and the other has $\hat{m}_x$ pointing in the opposite direction of B_s.

To determine which of these solutions is observed, we evaluate their stability. Denote the direction of the dipole for the solution in question $\hat{\boldsymbol{m}}_0$, which satisfies $\dot{\boldsymbol{m}}(\hat{\boldsymbol{m}}_0) = 0$. Since $\hat{\boldsymbol{m}}_0$ is a unit vector, it has only two degrees of freedom, which we can express in terms of an infinitesimal rotation $\boldsymbol{\sigma}$, such that a perturbation $\delta\hat{\boldsymbol{m}}_0 = \boldsymbol{\sigma} \times \hat{\boldsymbol{m}}_0$, where it is sufficient to consider $\boldsymbol{\sigma}$ in the two-dimensional space perpendicular to $\hat{\boldsymbol{m}}_0$. Then we find that $\dot{\boldsymbol{\sigma}} \times \hat{\boldsymbol{m}}_0 = \dot{\boldsymbol{m}}(\hat{\boldsymbol{m}}_0 + \delta\hat{\boldsymbol{m}}_0)$, or expanding to first order in the perturbation, $\dot{\boldsymbol{\sigma}} \times \hat{\boldsymbol{m}}_0 = -\frac{\partial \dot{\boldsymbol{m}}}{\partial \hat{\boldsymbol{m}}}(\hat{\boldsymbol{m}}_0 \times \boldsymbol{\sigma})$. From this we obtain

$$\dot{\boldsymbol{\sigma}} = -\hat{\boldsymbol{m}}_0 \times \left(\frac{\partial \dot{\boldsymbol{m}}}{\partial \hat{\boldsymbol{m}}}(\hat{\boldsymbol{m}}_0 \times \boldsymbol{\sigma})\right) \equiv \boldsymbol{Q\sigma}, \tag{S2}$$

where the last equivalence serves to define the linear operator $\boldsymbol{Q}$. To be explicit, in indicial notation

$$Q_{ij} = -\epsilon_{ikl}\hat{m}_k \frac{\partial \dot{m}_l}{\partial \hat{m}_n} \epsilon_{npj}\hat{m}_p, \tag{S3}$$

where all the components are evaluated at $\hat{\boldsymbol{m}}_0$, and ϵ_{ijk} is the Levi-Civita antisymmetric tensor. $\boldsymbol{Q}$ has one zero eigenvalue (corresponding to the $\hat{\boldsymbol{m}}_0$ direction) and two other eigenvalues. The solution $\hat{\boldsymbol{m}}_0$ is stable if the two other eigenvalues both have negative real parts. We find that the solution with $\hat{m}_x$ pointing in the direction of the static component B_s is stable, and the other is unstable.

Physically, the kinematics of the stable solution involves the magnetic dipole tilting towards the static component of the magnetic field, the sphere rotating about the *x*-axis such that the magnetic dipole rotates at the same rate as the rotating field, and the sphere additionally rotating about the magnetic dipole direction (which is itself changing in the lab frame). Thus, only the magnetic dipole undergoes steady rotation at the field angular velocity, while the sphere itself undergoes a more complex time-dependent rotation. In Fig. S11, we plot the tilt angle β between the *y*-*z* plane and the dipole ($\hat{m}_x = \sin\beta$) for increasing static field, and various field rotation rates. For zero static field, $\beta = 0$, but as the static field component increases so does the tilt angle.

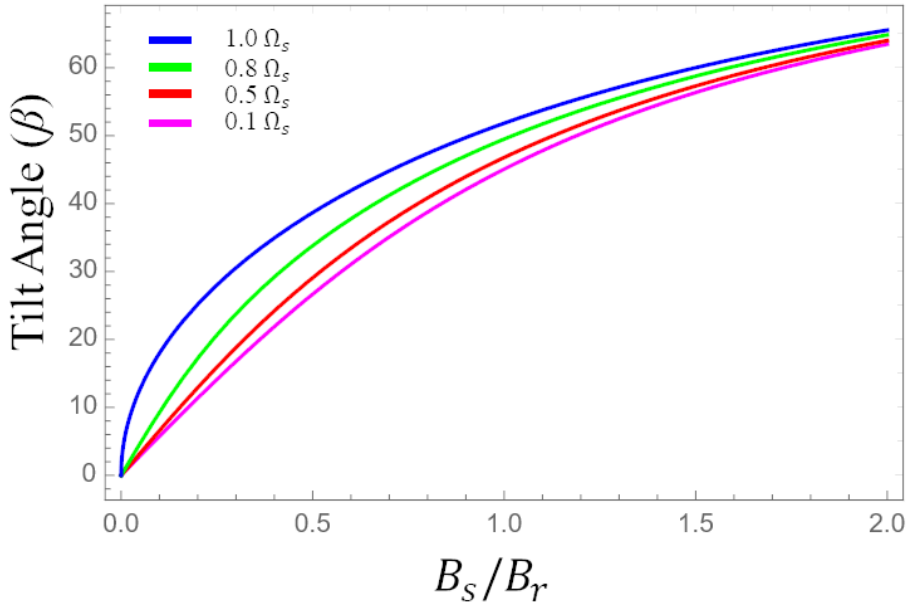

Fig. S11. Change in tilt angle in response to applied static magnetic field component B_s. Each curve is produced for the indicated value of rotation frequency (ω).

Section 6: Symmetry Breaking Propulsion Force

The force on a simultaneously rotating and translating sphere in the zero Reynolds number limit in a nonlinear third-order fluid was calculated using a retarded motion expansion[47] by Giesekus[40]. For a sphere translating in the *z*-direction and rotating with angular velocity Ω about the *z*-axis, up to second order in Deborah number the force in the *z* direction takes the form:

$$F = -6\pi\mu aU + DU^3 + C\Omega^2 U, \tag{S4}$$

where *D* and *C* are constants that depend on the material parameters of the fluid. As discussed in Chapter 2, the term proportional to $U\Omega^2$ couples rotation to translation in a way that corresponds to a possible symmetry-breaking force. If $C > 0$, the nonlinear force opposes drag and is propulsive, while if $C < 0$ the nonlinear force increases drag and stabilizes the state with no translation. Thus, we are interested in whether *C* is positive or negative for various nonlinear fluids. The results for various nonlinear fluids are discussed below.

Giesekus[40] calculates the force for both a dilute solution of elastic dumbbells, i.e., an Olroyd-B fluid, (his Eq. 72) and a dilute solution of rigid dumbbells or rods (his Eq. 74), and finds positive *C* for both. (Note that the sign of Giesekus' force in his paper is opposite ours since his sphere translates and rotates in the opposite directions.)

Table 6.2-1 of the textbook of Bird, Armstrong and Hassager[47] contains a table listing the parameters for the constitutive laws of third-order fluids corresponding to various kinetic theory models, namely a dilute solution of FENE dumbbells, a dilute solution of multi-bead rods, and a melt of freely-joined bead-rod chains. The table reports the coefficients b_1, b_2, b_{11}, b_3, b_{12}, and $b_{1:11}$ of the constitutive law, Eq. 6.2-1 of that textbook, which is written in terms of the rate of strain tensors defined therein (denoted $\gamma_{(n)}$in Bird, Armstrong and Hassager[47]). In order to use these parameters in Giesekus' result, one must deduce from them the values of the coefficients

denoted $\gamma_0^{(1)}, \gamma_0^{(2)}, \gamma_0^{(11)}, \gamma_0^{(3)}, \gamma_0^{(21)}$, and $\gamma_{11}^{(1)}$ in the constitutive law Eq. 3 (from Giesekus[40]) which is written in terms of (different) kinematic tensors $f^{(n)}$ defined in that paper. We found that

$$\begin{aligned} 2f^{(1)} &= \gamma_{(1)}, \\ 2f^{(2)} - 4f^{(1)} \bullet f^{(1)} &= \gamma_{(2)}, \\ 2f^{(3)} - 6\left(f^{(1)} \bullet f^{(2)} + f^{(2)} \bullet f^{(1)}\right) + 8\left(f^{(1)} \bullet f^{(1)} \bullet f^{(1)}\right) &= \gamma_{(3)}, \end{aligned} \tag{S5}$$

and that if

$$\begin{pmatrix} \gamma_0^{(1)} \\ \gamma_0^{(2)} \\ \gamma_0^{(11)} \\ \gamma_0^{(3)} \\ \gamma_0^{(21)} \\ \gamma_{11}^{(1)} \end{pmatrix} = \begin{pmatrix} 2 & 0 & 0 & 0 & 0 & 0 \\ 0 & 2 & 0 & 0 & 0 & 0 \\ 0 & -4 & 4 & 0 & 0 & 0 \\ 0 & 0 & 0 & 2 & 0 & 0 \\ 0 & 0 & 0 & -6 & 4 & 0 \\ 0 & 0 & 0 & 4 & -8 & 8 \end{pmatrix} \begin{pmatrix} b_1 \\ b_2 \\ b_{11} \\ b_3 \\ b_{12} \\ b_{1:11} \end{pmatrix}, \tag{S6}$$

then the constitutive laws given by Bird, Armstrong and Hassager[47] and Giesekus[40] were identical up to an isotropic function that could be absorbed into the pressure. Using this conversion, we find the nonlinear corrections of the force due to the constitutive laws in the table.

For the melt of freely-jointed bead-rod chains, we tested the sign of *C* at room temperature for molar volumes of polymer molecules of approximately 10^{-4} m^3/mol [146], corresponding to number densities of approximately 10^{28} molecules/m^3, a range of number of beads in each chain of 2 – 10, a solvent viscosity of 1 mPa, a range of time constants λ^k in Table 6.2-1 of Bird, Armstrong and Hassager[47] of 0.1-100 s, and a range of ε of 0.3-0.5 as suggested in that table. In all cases *C* was positive.

For the dilute solution of FENE dumbbells, we tested the sign of *C* at room temperature for number densities of polymer molecules in the range of 10^{26} – 10^{28} molecules/m^3, a solvent

viscosity of 1 mPa, a range of time constants λ_H in Table 6.2-1 of Bird, Armstrong, and Hassager[47] 0.1-100 s, and a range of b of 10-300 as suggested in that table. In all cases C was positive.

For the dilute solution of multibead rods, we tested the sign of C at room temperature for number densities of polymer molecules in the range of 10^{26} – 10^{28} molecules/m^3, a solvent viscosity of 1 mPa, a range of time constants $\lambda^{(1)}_N$ of 0.1-100 s, and a range of $[1 - \lambda^{(1)}_N/ \lambda_{(2)N}]$ of -0.5 – 0.3082 in Table 6.2-1 of Bird, Armstrong, and Hassager[47] as suggested in the that table. In all cases C was positive.

To summarize, in all the cases tested, the sign of C was positive, which indicates that the nonlinear correction to the force around a translating and rotating sphere acts to propel it, at least up to the order of the retarded motion expansion analyzed. As discussed in Chapter 2, this perturbative analysis is only suggestive and cannot explicitly find the symmetry-broken state. An explicit theoretical solution demonstrating symmetry breaking would likely require numerical simulations of a sphere in a nonlinear fluid.

Section 7: Approximate Helmholtz Coils and Magnetic Field Spatial Dependence

All experiments except those involving μPIV and fluorescence were conducted using an approximate Helmholtz coil system for Chapters 2-4. This system has been used extensively in our previous research[96,147,148]. The approximate Helmholtz coils themselves are composed of AWG 25 copper wire with approximately 600 turns each, have an outer diameter of 6.55 cm, an inner diameter of 4 cm, and a thickness of approximately 1.23 cm. The coils are separated from each other at a distance of twice their radius, differing from a traditional Helmholtz coil which has 1 radius of separation (thus why we call them 'approximate'). To account for this discrepancy, the voltages provided to the coils are increased such that a uniform magnetic field profile is present in the center of each coil pair. The coils are arranged in a tri-axial arrangement allowing for approximately uniform magnetic fields to be produced in all three dimensions. More details about specific experimental procedures can be found in the 2.4 Methods section of Chapter 2.

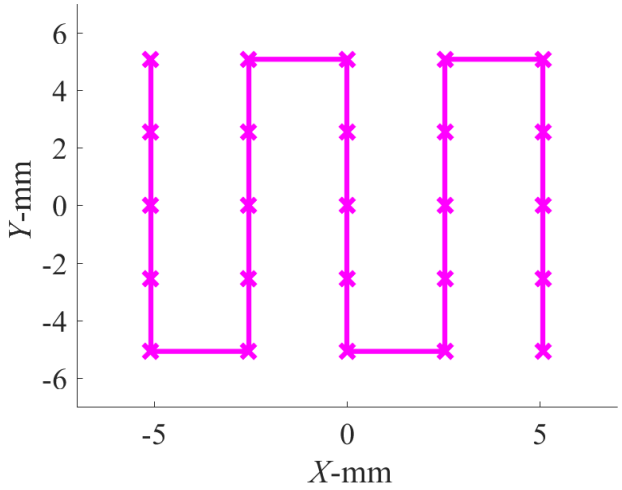

Fig. S12. Path of the magnetometer within the working space of the approximate Helmholtz coil system. The probe of the magnetometer began at (-5,5) and ended at (5,-5) with each point marked by an '×' representing a measurement location.

A THM1176 three axis Hall magnetometer (GWM Associates) was used to measure the magnetic fields at predefined locations within the approximate Helmholtz coil system. The working space at the center of the coil system was confined to an area of 2 cm^2; within this area the teslameter was moved at 2 mm increments along the path designated in Fig. S12. Measurements along this path were taken at *Z*-heights of 0, 1, and 2 mm for each coil pair. During experiments only one pair of coils was set to produce a static field of 2 mT. The measured magnetic fields at each point and height are displayed as a gradient heat map in Fig. S13 for all three coil pairs. In each plane the magnetic fields are mostly uniform, although they are slightly higher than the expected 2 mT value. The *Z*-coil pair [Fig. S13 (c)] appears to have high variation in magnetic fields as height increases along the *Z*-axis; this is confirmed when comparing the static field distributions of all three planes for each coil pair [Fig. S13 (d-f)]. However, the maximum magnetic

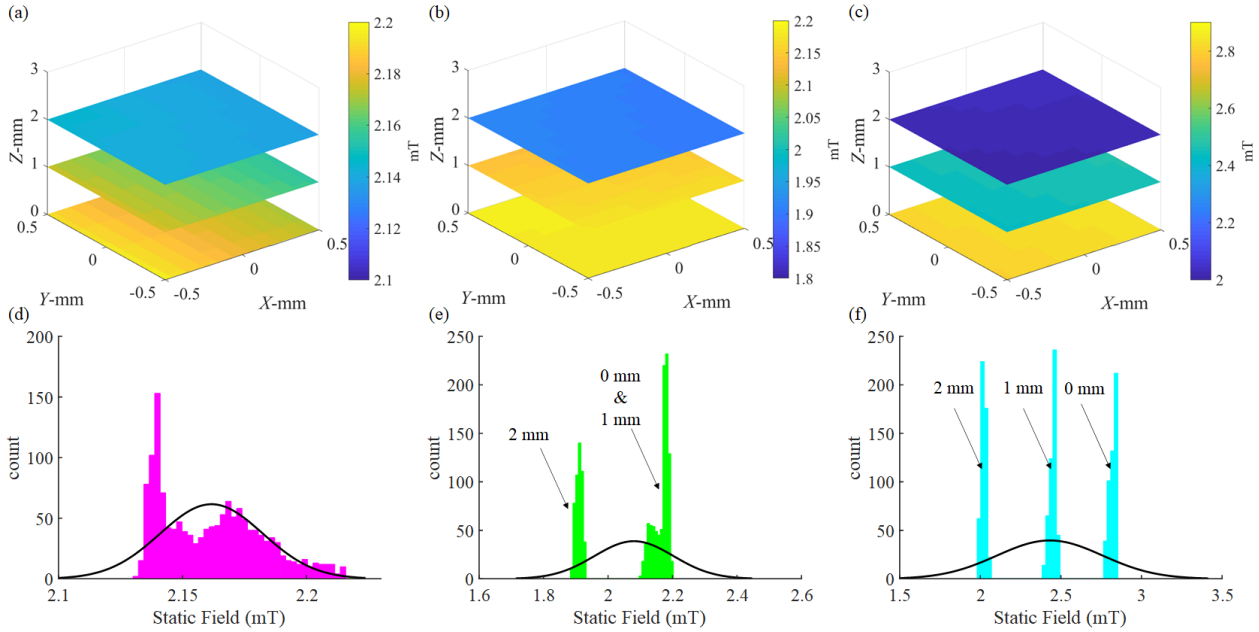

Fig. S13. Approximate Helmholtz coil magnetic field profiles. Magnetic field profiles for (a) X coil, (b) Y coil, and (c) Z coil at different spacings in the XYZ plane under a constant 2 mT static field along each respective direction for (a-c). (d-f) Static field value histograms of all three planes of measurement with estimated normal distributions (black solid lines). The mean static fields were (d) 2.16 mT, (e) 2.08 mT, and (f) 2.43 mT, while the standard deviations were 0.02 mT, 0.12 mT, and 0.34 mT, respectively. The Z coils had significant variance in static field values as height varied, while Y coil had a slight variance.

gradient does not exceed 0.05 mT/mm. Furthermore, given the evidence in Chapter 2 regarding the hysteresis of both microparticles suspended in mucus and polyacrylamide having noticeable propulsive behavior at 0 mT, under purely rotating magnetic fields, we can again dismiss gradients along the propulsive direction as being the primary driver of microparticle propulsion. The control data sets in Fig. 2.1 (b-c), Fig. 3.2 (b-d), and Fig. 4.2 (c) involving saline and methylcellulose solutions also demonstrate that propulsion is not occurring even at high rotational frequencies.

Section 8: Magnetic Field Gradients are not Responsible for Propulsion

In Chapters 2-4 we remark that since propulsion disappears as the rotational frequency approaches zero even though the static field remains present, gradients in the static magnetic field cannot be responsible for the observed propulsion. In this section we provide additional evidence ruling out magnetic field gradients as the cause of propulsion.

First, the estimated force on a magnetic bead was estimated to be 8×10^{-14} N, using the estimated two dimensional dipole moment of $[-1.899 \times 10^{-12},\ \ 6.277 \times 10^{-13}]\ A.m^2$ produced from the maximum magnetic field values of $[1.6978,\ \ 1.6733]$ mT measured in the *x*-*y* plane; using Stokes' law this force results in an estimated translational velocity of 0.0046 μm/s for a 10 μm diameter bead.

Since the estimated translational velocity is order of magnitudes smaller than typically observed propulsion velocities (of order 1 μm/s), the gradient field cannot be responsible for the propulsion observed. In addition, the static magnetic field gradients could not account for the demonstrated controllable propulsion along different directions.

To further assure that magnetic field gradients were not causing the translation behavior, microparticles of 10 μm diameter were dispersed inside a sample chamber containing a 4% mucin synthetic mucus medium and placed inside the approximate Helmholtz coil system. A 2 mT static field was applied along the *X*-coil pair (positive or negative) and microparticles were examined under both rotating (15 Hz) and non-rotating conditions for at least 20 seconds and videos were recorded at 30 frames per second (fps). A mean square displacement (MSD) analysis was performed to compare the diffusive behavior of microparticles under both conditions. The MSD was calculated using,

$$< r^2(\tau) > = \frac{1}{N-\tau}\sum_{i=1}^{N-\tau}[r(t_i+\tau) - r(t_i)]^2, \quad \text{(S7)}$$

where $< r^2(\tau) >$ is the MSD, N is the number of time steps for a given trajectory, τ is the lag time, r is the position vector, and t_i is the i^{th} time increment[103]. For both the rotating and non-rotating cases the MSD profiles were modeled using,

$$< r^2(\tau) > \propto 4D\tau^{\alpha}, \quad \text{(S8)}$$

where D is generalized diffusion and α is the anomalous diffusion exponent; fittings were produced from the ensemble averaged MSD data over multiple rotating microparticles (at least three with each having at least three independent trials) and non-rotating microparticles under the same conditions. The MSD of the rotating and non-rotating microparticles (averaged over at least 3 beads, each with at least 5 trials) can be seen in Fig. S14 (a-b). On the non-logarithmic plot [Fig. S14 (a)] the rotating behavior clearly induces ballistic behavior while the non-rotating case retains a flat MSD throughout. Comparing the results in Fig. S14 (b) against diffusive ($\alpha \sim 1$) and superdiffusive behavior ($\alpha > 1$), it is clear that rotating microparticles are actively propelling under rotation, while the non-rotating microparticles are only experiencing approximately diffusive behavior. After fitting the MSD data between lag time ranges of 1 to 5 seconds using a Delayed Rejection Adaptive Metropolis Markov chain Monte Carlo technique[104], (see Appendix Section 11 for more information) we find that diffusivity and the diffusion exponent are both reasonable for each case. For the non-rotating case the diffusivity and diffusion exponent were 0.0019 $\left(\frac{\mu m^2}{s^{\alpha}}\right)$

and 1.05. The rotating case had a diffusivity and diffusion exponent of 0.44 $\left(\frac{\mu m^2}{s^\alpha}\right)$ and 1.74; the plots for each can be seen as solid lines in Fig. S14 (b).

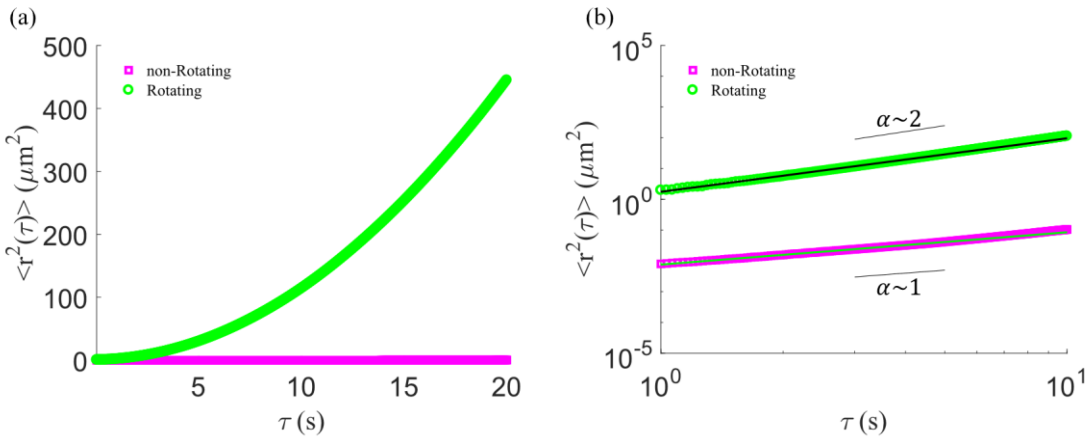

Fig. S14. Mean square displacement of rotating and non-rotating microparticles in 4% mucin. Mean square displacement where (a) is the non-logarithmic plot and (b) shows the logarithmic plot with fittings. The black long solid line corresponds to the fit for the rotating case and the long solid green line is the fit for the non-rotating case. Short solid lines represent general mean square displacement profiles for different values of α.

Section 9: Propulsion Velocity Dependence on Mucin Concentration and Particle Size

Only synthetic mucus of 4% mucin was explored in detail within Chapter 2 and can be considered a reasonable baseline since mucin concentrations within the human body typically ranges between 2-5%[43]. However, it was observed experimentally that microparticles could exhibit similar propulsive behavior for other concentrations of mucins. Presented in Fig. S15 are the propulsion velocities of 10 μm diameter microparticles within 2%, 3%, and 4% mucin solutions at different rotational frequencies; all data sets were averaged over six microparticles per diameter, per fluid, with at least 3 trials each. While at small frequencies (< 10 Hz) there is only minor variation between propulsion velocities, at larger frequencies (> 10 Hz) there are clear differences in propulsion behavior. Based on these trends it appears that increasing mucin concentration positively affects propulsion velocity, while lowering mucin concentration results in a velocity decrease. The limits of this behavior are not well understood at this time although it is expected that at extreme (higher or lower) mucin concentrations the microparticle propulsion velocity should decrease.

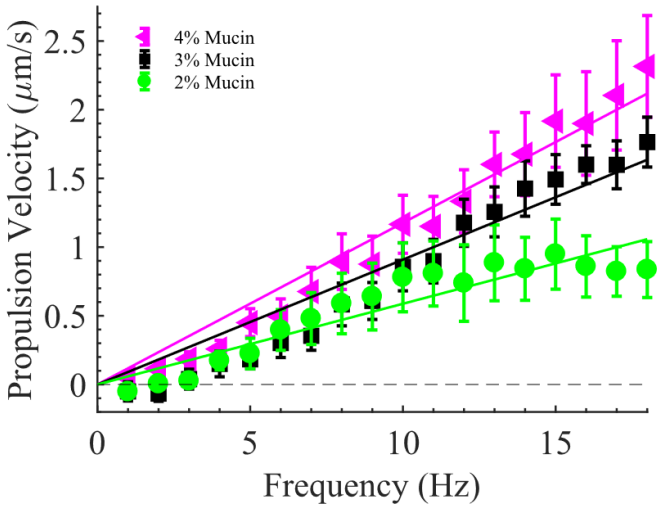

Fig. S15. Velocity and mucin concentration. Propulsion velocity vs. frequency for 10 μm diameter microparticles inside different concentrations of mucin. Error bars represent standard error.

We tested microparticles of several different diameters (2, 4, 8, and 10 µm) to determine if propulsion velocity was influenced by microparticle size [Fig. S16 (a-b)]; all data sets were averaged over at least three microparticles per fluid with at least 3 trials each. In 4% mucin as microparticle diameter increased, so did propulsion velocity, except that both 2 µm diameter microparticles and 4 µm diameter microparticles were nearly identical and had overlapping velocity curves. In 0.25% polyacrylamide the influence of microparticle diameter was less obvious, with 2 µm microparticles being faster than 4 µm microparticles, and 8 µm microparticles having a markedly non-linear relationship to frequency. Other than the 8 µm microparticles in polyacrylamide, for frequencies less than 10 Hz, the velocities of the differently sized microparticles in both fluids were all within a standard error of each other; but for frequencies above 10 Hz the velocity profiles of each diameter microparticle become more distinct from each other.

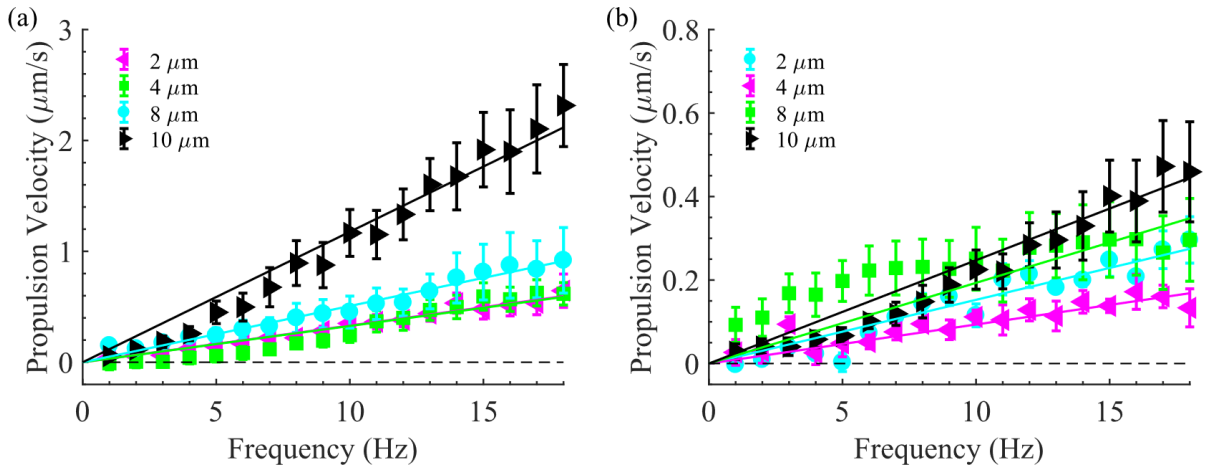

Fig. S16. Velocity and microparticle diameter. (a) Propulsion velocity vs. frequency for different diameter microparticles in 4% mucin. The coefficients of determination (r^2) values were 0.976, 0.8875, 0.9733, and 0.9650 for 2 µm, 4 µm, 8 µm, and 10 µm, respectively. (b) Propulsion velocity vs. frequency for different diameter microparticles in 0.25% polyacrylamide. The r^2 values were 0.9255, 0.8066, -0.4007, and 0.9483 for 2 µm, 4 µm, 8 µm, and 10 µm, respectively. Error bars represent standard error.

Section 10: Rheological Analysis of First and Second Normal Stress

The first normal stress difference (N_1) was measured directly from the axial force (F_{CP}) in a 2° cone-and-plate geometry (60 mm in diameter) on a TA Instruments AR-G2 rheometer,

$$N_1 = \frac{2F_{CP}}{\pi R^2}. \quad \text{(S9)}$$

The second normal stress difference (N_2) was measured by comparing the axial force in the cone-and-plate geometry to the axial force (F_{PP}) in a parallel-plate (60 mm diameter) geometry[83,84],

$$N_1 - N_2 = \frac{F_{PP}}{\pi R^2}\left[2 + \frac{d\ln\left(\frac{F_{PP}}{\pi R^2}\right)}{d\ln(\dot{\gamma})}\right], \quad \text{(S10)}$$

where R is the radius of the geometry, and $\dot{\gamma}$ is the shear rate at the rim of the geometry. We zeroed the axial force balance before each sweep of shear rates and checked that the meniscus of the sample did not change shape during the sweep to ensure that capillary forces did not affect the axial force measurements. A polymethyl methacrylate (PMMA) sheet was used for the lower geometry surface to stabilize the contact line. Care was taken to trim the gap after sample loading and to ensure no air bubbles were trapped in the rheometer during sample loading.

We validated our measurements by comparing measurements of the normal stresses of a 2.5% polyacrylamide solution in water [Fig. S17 (a), averaged over 3 runs] to those reported in the literature[149] (see Fig. 3.3-5 in reference). Similar to the reported values for 1.5%

polyacrylamide solution in a water-glycerin mixture, we measured a positive first normal stress coefficient,

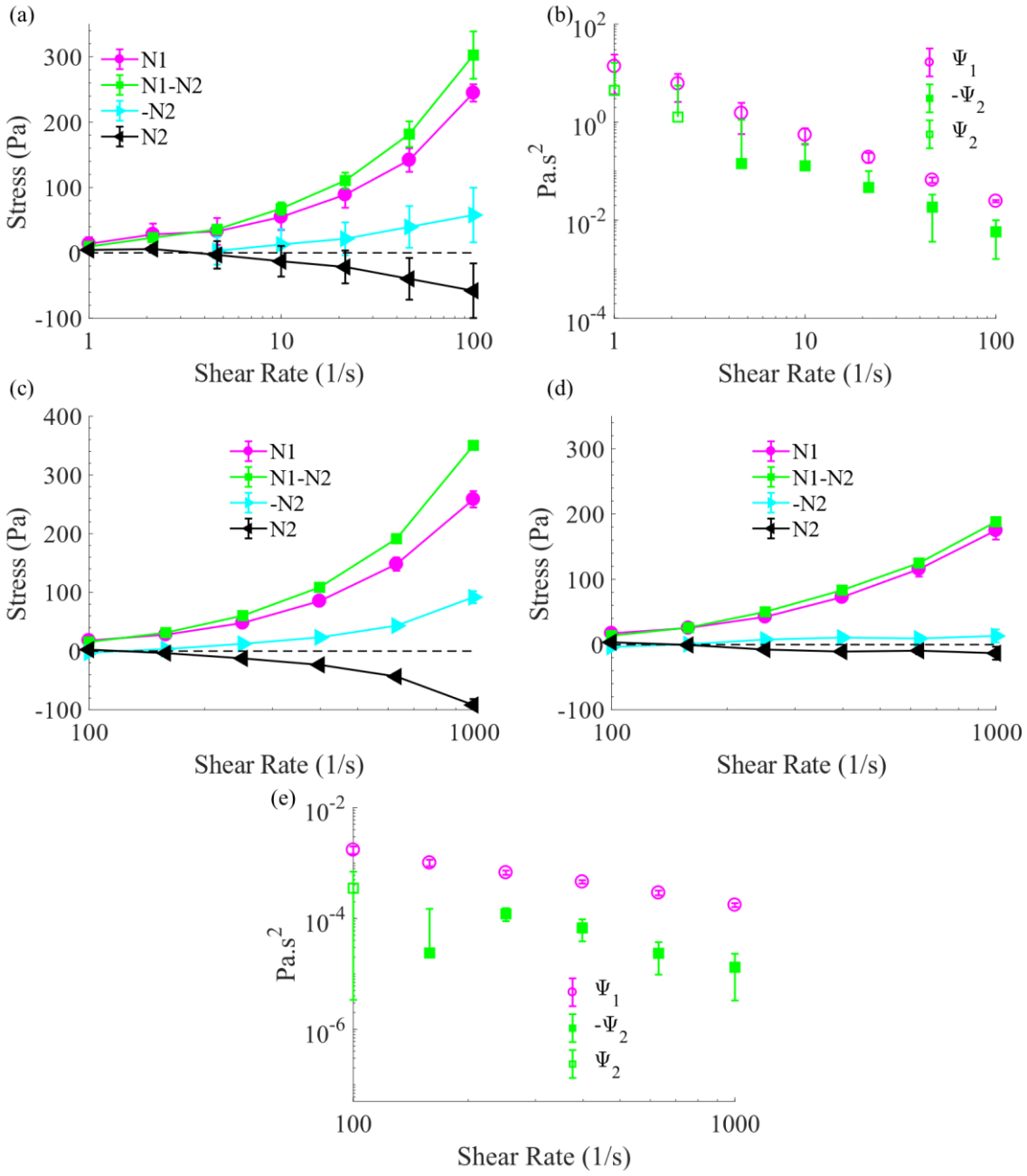

Fig. S17. First and second normal stresses for polyacrylamide and mucin. (a) First and second normal stress differences for 2.5% polyacrylamide and respective (b) normal stress coefficients. (c) First and second normal stress differences for 10% mucin with theoretical inertial correction, with its respective normal stress coefficients shown in Fig. 2.5 (e). (d) First and second normal stress differences for 10% mucin with experimental inertial correction and its respective (e) normal stress coefficients. Error bars represent standard deviation.

$$\Psi_1 = \frac{N_1}{\dot{\gamma}^2}, \tag{S11}$$

that decreased with increasing shear rate as $\dot{\gamma}^{-\frac{3}{2}}$, and a negative second normal stress coefficient,

$$\Psi_2 = \frac{N_2}{\dot{\gamma}^2}, \tag{S12}$$

that was about 23% the magnitude of the first normal stress coefficient [Fig. S17 (b)]. The magnitude of our measured normal stresses were systematically smaller than those reported previously, possibly due to differences in the solvents and molecular weight of the polyacrylamide.

We measured the normal stress differences of a 10% mucin solution for shear rates between 100 and 1000 s^{-1} (near microparticles rotating at 15-20 Hz, shear rates are 94-125 s^{-1} in our experiments). For each geometry, three runs were performed with the addition of a drop of nonionic surfactant (Nonidet P-40; 0.025 m/v% aqueous solution) to the air-sample interface. For these shear rates, inertial effects and normal stress differences contributed similar magnitude axial forces. We corrected for inertial effects in two different ways in Fig. S17 (c-e). The expected axial forces due to inertia are theoretically expected to be $F = -0.075\rho\pi W^2 R^4$ where ρ is the density of the fluid, W is the angular velocity, and R is the radius of the geometry[150]. Normal stress difference measurements corrected using these expected axial forces were used to plot Fig. S17 (c), while the normal stress coefficients were plotted in Fig. 2.5 (e). As a check of the accuracy of the theoretical inertial correction, we also measured axial forces due to inertia by performing measurements on water, with and without the addition of surfactant (Nonidet P-40; 0.025 m/v% aqueous solution) to account for any capillary effects. We observed no significant dependence on geometry type or impact due to capillary forces; however, we did find the measured contribution

due to inertia to be slightly less than expected. Normal stress difference measurements and normal stress coefficients corrected using these measured axial forces were used to plot Fig. S17 (d-e).

Both Fig. 2.5 (e) and Fig. S17 (e) show that the mucin solution also has positive first normal stress coefficients and smaller negative second normal stress coefficients in this range of shear rates. The magnitude of normal stress differences is significantly smaller than those we measured in polyacrylamide solution. For both 0.25% polyacrylamide and 4% mucin solution, axial forces were even smaller and below the limit of the sensitivity of the force transducers on both rheometers used during experiments, so we could not obtain reliable measurements.

To summarize, our measurements show that mucin solutions develop normal stress differences under shear, which can lead to rod-climbing-like effects such as those we propose are responsible for symmetry-breaking propulsion.

Section 11: Secondary Flows from Microparticle Rotating

Here we compare the radial inward flow observed in our μPIV data for particles propelling in the *z*-direction [Fig. 2.4 (g-i)] to the secondary flows expected for nonlinearly viscoelastic fluids. The secondary flow around a rotating and translating sphere predicted by the perturbation expansion described in Section 6 is,

$$\begin{bmatrix} v_r \\ v_\theta \\ v_\phi \end{bmatrix} = \begin{bmatrix} \frac{(-1+B_{11})(-1+r)^2(-8-3U^2+r(-4+3U^2))(1+3\cos 2\theta)}{16r^5} \\ \frac{-3(-1+B_{11})(-1+r)(-8+3(-1+r)U^2)\sin 2\theta}{16r^5} \\ \frac{3(-1+B_{11})(-1+r)U\sin 2\theta}{4r^4} \end{bmatrix}, \tag{S13}$$

where r is the nondimensional radius of the sphere, U is the nondimensional velocity, θ is the cartesian angle from the spheres propulsion axis to it's center plane, and $B_{11} = \frac{b_{11}}{b_2}$ depends on the parameters of the constitutive law (see Appendix Section 6), where each term on the left hand side are the velocities in the spherical basis. The radial flow fields along the plane where $\theta = \frac{\pi}{2}$ were extracted from the μPIV data [Fig. 2.4 (g)] and plotted in Fig. S18 (a) for various angles of ϕ; the average of these is shown using the black symbols and line in Fig. S18 (a). Aside from some variation between the different ϕ values, all of the velocity profiles were markedly similar. It is

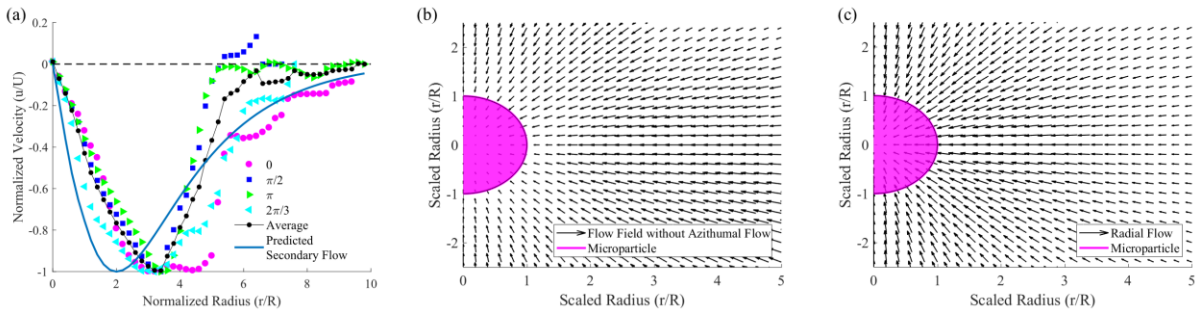

Fig. S18. Experimental and theoretical secondary flows. (a) Experimentally extracted secondary radial flow along several angles of ϕ for $\theta = \frac{\pi}{2}$, an ensemble average between the different angles, and a fit to the ensemble average over a range of different *z*-planes using Equation S13. (b) Experimentally extracted vector field of radial flow. (c) Theoretically predicted radial flow vector field using the estimated parameters and averages between the planes.

important to note here that the non-zero velocity within one normalized radius of the particle is the result of the particle translating upwards during the experiment. The resulting averaged radial component was used to nonlinearly fit the parameters B_{11}, U, and the beginning and end heights of the *z*-slices used for averaging, by comparing the average μPIV radial flow [black curve in Fig. S18 (a)]. The best fit parameters were calculated using a delayed rejection adaptive Metropolis (DRAM) Markov chain Monte Carlo algorithm[104]. Markov chains had a length of 100,000 and only the last 10% of the chain was used to estimate the parameters. A burn-in of 10,000 was used before adaptation occurred using the DRAM process. No prior distributions were utilized but there was a restriction of $||B_{11}|| < 1$ and that the starting *z*-slice was limited to $\leq$ 1 radii and the ending *z*-slice had to be > 1. Additionally, the fit was normalized again by its absolute maximum value to scale correctly with the ensemble averaged data. The ensemble average and the proposed fit can be found in Fig. S18 (a). The estimated values for B_{11} and U for the fit were 0.0326 and 1.2911, respectively. The optimized starting and ending *z*-slices were estimated to be -2.8507 and 4.2760 radii, respectively. The best-fit secondary flow prediction is similar to those of experiments, with the main difference being the radial position of the maximum magnitude of radial velocity. The vector flow field for the experimental data is shown in Fig. S18 (b) while the vector field from the estimated fit can be seen in Fig. S18 (c).

Section 12: μPIV in 0.25% Polyacrylamide

Performing the same μPIV experiment as Fig. 2.4 (g-i) in 0.25% polyacrylamide resulted in similar flow fields to those produced in the 4% mucin experiments. These results can be seen in Fig. S19 where a 10 μm diameter microparticle was rotated at 15 Hz along the positive *z*-direction. The radial component of the flow field in Fig. S19 (a) matches the secondary flows predicted by the theory and is similar to the ones displayed by particles in 4% mucin; the (b) azimuthal velocity and (c) total velocity are likewise comparable.

When imaging the μPIV of a 2 μm particle, we find that the flow fields are very similar to the ones produced by the larger particles. Figure S20 shows (a) the radial, (b) the azimuthal, and (c) total flow field for a 2 μm microparticle; unlike the 10 μm case, this particle was not in contact with the substrate and was ≥ 20 μm away from it. Note that the radial inward flow remains present despite the larger distance from the substrate, indicating that the secondary flow is not caused by

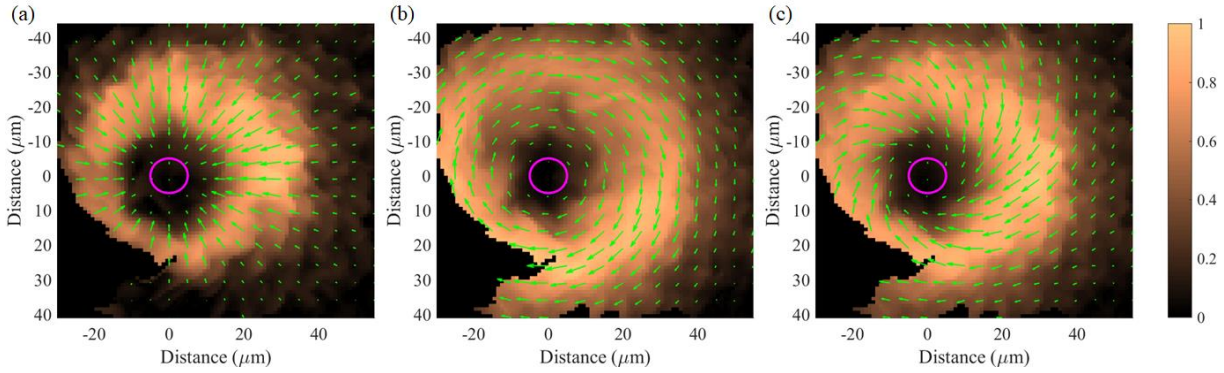

Fig. S19. μPIV in 0.25% polyacrylamide. The (a) radial, (b) azimuthal, and (c) total velocity flow field for a microparticle propelling away from the substrate (positive *z*-direction). All μPIV experiments were performed close to the boundary (< 100 μm, see 2.4 Methods). Magenta circle is the microparticle. Color bars to the right represents percentage of velocity magnitude with respect to the maximum velocity magnitude.

boundary effects. Compared to the 10 μm case, the magnitude of the flows decay more rapidly as distance from the sphere increases, perhaps due to boundary effects.

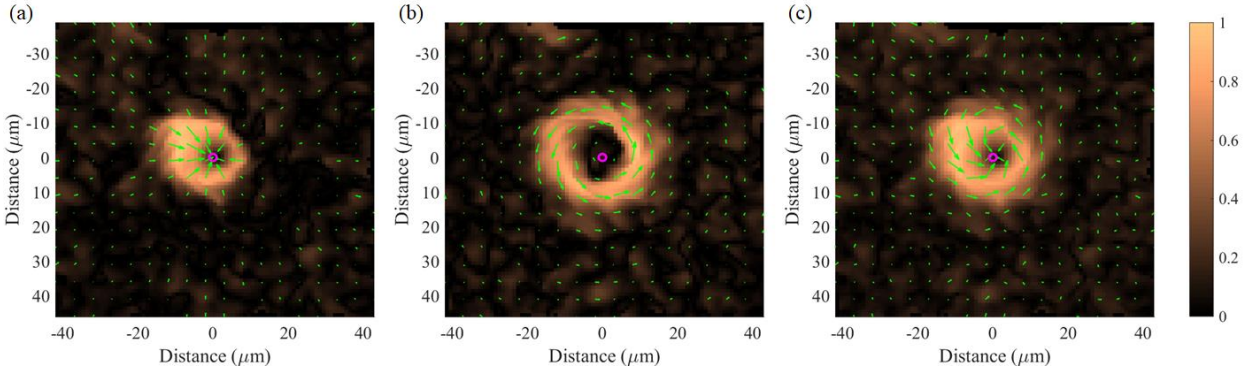

Fig. S20. μPIV in 0.25% polyacrylamide for a 2 μm particle. The (a) radial, (b) azimuthal, and (c) total velocity flow field for a 2 μm microparticle propelling in the positive z-direction. The microparticle was 20 μm off the substrate. All μPIV experiments were performed close to the boundary (< 100 μm, see 2.4 Methods). Magenta circle is the microparticle. Color bars to the right represents percentage of velocity magnitude with respect to the maximum velocity magnitude.

Section 13: Additional µPIV Information

All µPIV graphs shown in Chapter 2 and throughout the Appendix section were normalized between 0 and 1 for comparability. Provided below in Table S.1 is a listing of each figure and the maximum absolute velocities measured by the µPIV software during each experiment.

Table S.1: Maximum Velocity in µPIV Figures

Figure #	Maximum Velocity ($\mu m/s$)
Fig. 2.4 (a)	58.91
Fig. 2.4 (b)	47.21
Fig. 2.4 (c)	73.01
Fig. 2.4 (d)	59.91
Fig. 2.4 (e)	73.16
Fig. 2.4 (f)	82.26
Fig. 2.4 (g)	164.26
Fig. 2.4 (h)	162.69
Fig. 2.4 (i)	218.70
Fig. S19 (a)	207.00
Fig. S19 (b)	189.97
Fig. S19 (c)	253.02
Fig. S20 (a)	90.16
Fig. S20 (b)	72.49
Fig. S20 (c)	100.84

REFERENCES

1 Feynman, R. P. in *APS Annual Meeting*.

2 Bozuyuk, U. *et al.* Light-triggered drug release from 3D-printed magnetic chitosan microswimmers. *ACS Nano* **12**, 9617-9625 (2018).

3 Selimis, A., Mironov, V. & Farsari, M. Direct laser writing: Principles and materials for scaffold 3D printing. *Microelectronic Engineering* **132**, 83-89 (2015).

4 Kim, S. *et al.* Fabrication and characterization of magnetic microrobots for three-dimensional cell culture and targeted transportation. *Advanced Materials* **25**, 5863-5868 (2013).

5 Qiu, F. *et al.* Artificial bacterial flagella functionalized with temperature-sensitive liposomes for controlled release. *Sensors and Actuators B: Chemical* **196**, 676-681 (2014).

6 Qiu, F. *et al.* Noncytotoxic artificial bacterial flagella fabricated from biocompatible ORMOCOMP and iron coating. *Journal of Materials Chemistry B* **2**, 357-362 (2014).

7 Servant, A., Qiu, F., Mazza, M., Kostarelos, K. & Nelson, B. J. Controlled in vivo swimming of a swarm of bacteria-like microrobotic flagella. *Advanced Materials* **27**, 2981-2988 (2015).

8 Suter, M. *et al.* Superparamagnetic microrobots: fabrication by two-photon polymerization and biocompatibility. *Biomedical Microdevices* **15**, 997-1003 (2013).

9 Tottori, S. *et al.* Magnetic helical micromachines: fabrication, controlled swimming, and cargo transport. *Advanced materials* **24**, 811-816 (2012).

10 Zhang, L. *et al.* Artificial bacterial flagella: Fabrication and magnetic control. *Applied Physics Letters* **94**, 064107 (2009).

11 Zhang, L., Peyer, K. E. & Nelson, B. J. Artificial bacterial flagella for micromanipulation. *Lab on a Chip* **10**, 2203-2215 (2010).

12 Wang, X. *et al.* 3D printed enzymatically biodegradable soft helical microswimmers. *Advanced Functional Materials* **28**, 1804107 (2018).

13 Gao, W. *et al.* Bioinspired helical microswimmers based on vascular plants. *Nano Letters* **14**, 305-310 (2014).

14 Kamata, K. *et al.* Spirulina-templated metal microcoils with controlled helical structures for THz electromagnetic responses. *Scientific Reports* **4**, 4919 (2014).

15 Yan, X. *et al.* Multifunctional biohybrid magnetite microrobots for imaging-guided therapy. *Science Robotics* **2** (2017).

16 Khalil, I. S., Fatih Tabak, A., Klingner, A. & Sitti, M. Magnetic propulsion of robotic sperms at low-Reynolds number. *Applied Physics Letters* **109**, 033701 (2016).

17 Peyer, K. E., Siringil, E. C., Zhang, L., Suter, M. & Nelson, B. J. in *Conference on Biomimetic and Biohybrid Systems.* 216-227 (Springer).

18 Baraban, L. *et al.* Catalytic Janus motors on microfluidic chip: deterministic motion for targeted cargo delivery. *ACS Nano* **6**, 3383-3389 (2012).

19 Das, S., Steager, E. B., Hsieh, M. A., Stebe, K. J. & Kumar, V. Experiments and open-loop control of multiple catalytic microrobots. *Journal of Micro-Bio Robotics* **14**, 25-34 (2018).

20 Cheang, U. K. & Kim, M. J. Self-assembly of robotic micro-and nanoswimmers using magnetic nanoparticles. *Journal of Nanoparticle Research* **17**, 145 (2015).
21 Cheang, U. K. *et al.* in *2015 12th International Conference on Ubiquitous Robots and Ambient Intelligence (URAI)*. 518-523 (IEEE).
22 Kaynak, M. *et al.* Acoustic actuation of bioinspired microswimmers. *Lab on a Chip* **17**, 395-400 (2017).
23 Bechinger, C. *et al.* Active particles in complex and crowded environments. *Reviews of Modern Physics* **88**, 045006 (2016).
24 Purcell, E. M. Life at low Reynolds number. *American Journal of Physics* **45**, 3-11 (1977).
25 Lauga, E. & Powers, T. R. The hydrodynamics of swimming microorganisms. *Reports on Progress in Physics* **72**, 096601 (2009).
26 Lauga, E. Life around the scallop theorem. *Soft Matter* **7**, 3060-3065 (2011).
27 Cheang, U. K., Meshkati, F., Kim, D., Kim, M. J. & Fu, H. C. Minimal geometric requirements for micropropulsion via magnetic rotation. *Physical Review E* **90**, 033007 (2014).
28 Meshkati, F. & Fu, H. C. Modeling rigid magnetically rotated microswimmers: Rotation axes, bistability, and controllability. *Physical Review E* **90**, 063006 (2014).
29 Sachs, J. *et al.* Role of symmetry in driven propulsion at low Reynolds number. *Physical Review E* **98**, 063105 (2018).
30 Rogowski, L., Ali, J., Zhang, X., Fu, H. & Kim, M. J. Propulsion of microparticles in nonlinearly viscoelastic fluids through symmetry breaking. *Bulletin of the American Physical Society* (2020).
31 Fu, H., Rogowski, L., Ali, J., Zhang, X. & Kim, M. Propulsion of spherical microparticles through spontaneous symmetry breaking in mucus. *Bulletin of the American Physical Society* **64** (2019).
32 Rogowski, L. W., Oxner, M., Tang, J. & Kim, M. J. Heterogeneously flagellated microswimmer behavior in viscous fluids. *Biomicrofluidics* **14**, 024112 (2020).
33 Rogowski, L., Tang, J., Zhang, X., Oxner, M. & Kim, M. J. Flagellated Janus particles for swimming and catalytic propulsion. *Bulletin of the American Physical Society* (2020).
34 Qiu, T. *et al.* Swimming by reciprocal motion at low Reynolds number. *Nature Communications* **5**, 5119 (2014).
35 Rogowski, L. W., Kim, H., Zhang, X. & Kim, M. J. in *15th International Conference on Ubiquitous Robots (UR)*. 5-10 (IEEE, 2018).
36 Puente-Velázquez, J. A., Godínez, F. A., Lauga, E. & Zenit, R. Viscoelastic propulsion of a rotating dumbbell. *Microfluidics and Nanofluidics* **23**, 108 (2019).
37 Strogatz, S. H. Nonlinear dynamics and chaos. (1996).
38 Keim, N. C., Garcia, M. & Arratia, P. E. Fluid elasticity can enable propulsion at low Reynolds number. *Physics of Fluids* **24**, 081703 (2012).
39 Pak, O. S., Zhu, L., Brandt, L. & Lauga, E. Micropropulsion and microrheology in complex fluids via symmetry breaking. *Physics of Fluids* **24**, 103102 (2012).
40 Giesekus, H. Die simultane Translations-und Rotationsbewegung einer Kugel in einer elastoviskosen Flüssigkeit. *Rheologica Acta* **3**, 59-71 (1963).
41 Zhu, L., Lauga, E. & Brandt, L. Low-Reynolds-number swimming in a capillary tube. *Journal of Fluid Mechanics* **726**, 285-311 (2013).
42 Li, G.-J. & Ardekani, A. M. Hydrodynamic interaction of microswimmers near a wall. *Physical Review E* **90**, 013010 (2014).

43 Lai, S. K., Wang, Y.-Y., Wirtz, D. & Hanes, J. Micro-and macrorheology of mucus. *Advanced Drug Delivery Reviews* **61**, 86-100 (2009).
44 Boger, D. V. & Walters, K. *Rheological Phenomena in Focus*. (Elsevier, 2012).
45 Keegan, F. *Experimental investigation into non-Newtonian fluid flow through gradual contraction geometries*, Citeseer, (2009).
46 Christiansen, E. & Leppard, W. Steady-State and Oscillatory Flow Properties of Polymer Solutions. *Transactions of the Society of Rheology* **18**, 65-86 (1974).
47 Bird, R. B., Armstrong, R. C. & Hassager, O. Dynamics of polymeric liquids. Vol. 1: Fluid mechanics. (1987).
48 Moreira, R., Chenlo, F., Silva, C. & Torres, M. D. Rheological behaviour of aqueous methylcellulose systems: Effect of concentration, temperature and presence of tragacanth. *LWT - Food Science and Technology* **84**, 764-770 (2017).
49 Lauga, E. & Bartolo, D. No many-scallop theorem: Collective locomotion of reciprocal swimmers. *Physical Review E* **78**, 030901 (2008).
50 Happel, J. & Brenner, H. *Low Reynolds number hydrodynamics: with special applications to particulate media*. Vol. 1 (Springer Science & Business Media, 2012).
51 Hiller, D. High coercivity chromium dioxide. *Journal of Applied Physics* **49**, 1821-1822 (1978).
52 Castillo, A. *et al.* Drag coefficient for a sedimenting and rotating sphere in a viscoelastic fluid. *Physical Review Fluids* **4**, 063302 (2019).
53 Muller, S. J. Elastically-influenced instabilities in Taylor-Couette and other flows with curved streamlines: a review. *Korea-Australia Rheology Journal* **20**, 117-125 (2008).
54 Yoncheva, K., Vandervoort, J. & Ludwig, A. Development of mucoadhesive poly (lactide-co-glycolide) nanoparticles for ocular application. *Pharmaceutical Development and Technology* **16**, 29-35 (2011).
55 Ci, L. *et al.* Amino-functionalized poloxamer 407 with both mucoadhesive and thermosensitive properties: preparation, characterization and application in a vaginal drug delivery system. *Acta Pharmaceutica Sinica B* **7**, 593-602 (2017).
56 Oaku, Y. *et al.* Impact of surface coated magnetite used in magnetic drug delivery system on immune response. *Journal of Applied Physics* **117**, 17D135 (2015).
57 Reichelt, S., Elsner, C., Pender, A. & Buchmeiser, M. R. Tailoring the surface of magnetic microparticles for protein immobilization. *Journal of Applied Polymer Science* **121**, 3628-3634 (2011).
58 Popov, A., Schopf, L., Bourassa, J. & Chen, H. Enhanced pulmonary delivery of fluticasone propionate in rodents by mucus-penetrating nanoparticles. *International Journal of Pharmaceutics* **502**, 188-197 (2016).
59 Anderski, J., Mahlert, L., Mulac, D. & Langer, K. Mucus-penetrating nanoparticles: Promising drug delivery systems for the photodynamic therapy of intestinal cancer. *European Journal of Pharmaceutics and Biopharmaceutics* **129**, 1-9 (2018).
60 Boya, V. N. *et al.* Probing mucin interaction behavior of magnetic nanoparticles. *Journal of Colloid and Interface Science* **488**, 258-268 (2017).
61 Wang, N. *et al.* Magnetic nanoparticles (MNPs) covalently coated by PEO–PPO–PEO block copolymer for drug delivery. *Journal of Colloid and Interface Science* **395**, 50-57 (2013).
62 Jain, A. & Cheng, K. The principles and applications of avidin-based nanoparticles in drug delivery and diagnosis. *Journal of Controlled Release* **245**, 27-40 (2017).

63 Park, J.-H. *et al.* Preparation and characterization of magnetic chitosan particles for hyperthermia application. *Journal of Magnetism and Magnetic Materials* **293**, 328-333 (2005).
64 Le Renard, P.-E. *et al.* Magnetic and in vitro heating properties of implants formed *in situ* from injectable formulations and containing superparamagnetic iron oxide nanoparticles (SPIONs) embedded in silica microparticles for magnetically induced local hyperthermia. *Journal of Magnetism and Magnetic Materials* **323**, 1054-1063 (2011).
65 Arruebo, M., Fernández-Pacheco, R., Ibarra, M. R. & Santamaría, J. Magnetic nanoparticles for drug delivery. *Nano Today* **2**, 22-32 (2007).
66 Sun, C., Lee, J. S. & Zhang, M. Magnetic nanoparticles in MR imaging and drug delivery. *Advanced Drug Delivery Reviews* **60**, 1252-1265 (2008).
67 Veiseh, O., Gunn, J. W. & Zhang, M. Design and fabrication of magnetic nanoparticles for targeted drug delivery and imaging. *Advanced Drug Delivery Reviews* **62**, 284-304 (2010).
68 Cheang, U. K. & Kim, M. J. Fabrication and control of simple low Reynolds number microswimmers. *Applied Physics Letters* **109**, 034101 (2016).
69 Murgia, X., Loretz, B., Hartwig, O., Hittinger, M. & Lehr, C.-M. The role of mucus on drug transport and its potential to affect therapeutic outcomes. *Advanced Drug Delivery Reviews* **124**, 82-97 (2018).
70 Juge, N. Microbial adhesins to gastrointestinal mucus. *Trends in Microbiology* **20**, 30-39 (2012).
71 Groo, A.-C. & Lagarce, F. Mucus models to evaluate nanomedicines for diffusion. *Drug Discovery Today* **19**, 1097-1108 (2014).
72 Johansson, M. E., Sjövall, H. & Hansson, G. C. The gastrointestinal mucus system in health and disease. *Nature Reviews Gastroenterology & Hepatology* **10**, 352 (2013).
73 Katz, D., Mills, R. & Pritchett, T. The movement of human spermatozoa in cervical mucus. *Reproduction* **53**, 259-265 (1978).
74 Berg, H. C. & Turner, L. Movement of microorganisms in viscous environments. *Nature* **278**, 349 (1979).
75 Riley, E. E. & Lauga, E. Enhanced active swimming in viscoelastic fluids. *EPL (Europhysics Letters)* **108**, 34003 (2014).
76 Fu, H. C., Powers, T. R. & Wolgemuth, C. W. Theory of swimming filaments in viscoelastic media. *Physical Review Letters* **99**, 258101 (2007).
77 Natale, G., Datt, C., Hatzikiriakos, S. G. & Elfring, G. J. Autophoretic locomotion in weakly viscoelastic fluids at finite Péclet number. *Physics of Fluids* **29**, 123102 (2017).
78 Teran, J., Fauci, L. & Shelley, M. Fluid elasticity can enable propulsion at low Reynolds number. *Physical Review Letters* **104**, 038101 (2010).
79 Qu, Z., Temel, F. Z., Henderikx, R. & Breuer, K. S. Changes in the flagellar bundling time account for variations in swimming behavior of flagellated bacteria in viscous media. *Proceedings of the National Academy of Sciences* **115**, 1707-1712 (2018).
80 Patteson, A., Gopinath, A., Goulian, M. & Arratia, P. Running and tumbling with E. coli in polymeric solutions. *Scientific Reports* **5**, 15761 (2015).
81 Michelin, S., Lauga, E. & Bartolo, D. Spontaneous autophoretic motion of isotropic particles. *Physics of Fluids* **25**, 061701 (2013).
82 Vandenberghe, N., Zhang, J. & Childress, S. Symmetry breaking leads to forward flapping flight. *Journal of Fluid Mechanics* **506**, 147-155 (2004).

83 Mall-Gleissle, S. E., Gleissle, W., McKinley, G. H. & Buggisch, H. The normal stress behaviour of suspensions with viscoelastic matrix fluids. *Rheologica Acta* **41**, 61-76 (2002).
84 Alcoutlabi, M. *et al.* A comparison of three different methods for measuring both normal stress differences of viscoelastic liquids in torsional rheometers. *Rheologica Acta* **48**, 191-200 (2009).
85 Berg, H. C. Bacterial behaviour. *Nature* **254**, 389-392 (1975).
86 Hasegawa, K., Suzuki, H., Vonderviszt, F., Mimori-Kiyosue, Y. & Namba, K. Structure and switching of bacterial flagellar filaments studied by X-ray fiber diffraction. *Nature structural biology* **5**, 125-132 (1998).
87 Hayashi, F. *et al.* Key amino acid residues involved in the transitions of L-to R-type protofilaments of the Salmonella flagellar filament. *Journal of Bacteriology* **195**, 3503-3513 (2013).
88 Kamiya, R. & Asakura, S. Flagellar transformations at alkaline pH. *Journal of Molecular Biology* **108**, 513-518 (1976).
89 Darnton, N. C. & Berg, H. C. Force-Extension Measurements on Bacterial Flagella: Triggering Polymorphic Transformations. *Biophysical Journal* **92**, 2230-2236 (2007).
90 Kamiya, R. & Asakura, S. Helical transformations of Salmonella flagella in vitro. *Journal of Molecular Biology* **106**, 167-186 (1976).
91 Qiu, T. *et al.* Swimming by reciprocal motion at low Reynolds number. *Nature communications* **5**, 1-8 (2014).
92 Asakura, S., Eguchi, G. & Iino, T. Reconstitution of bacterial flagella in vitro. *Journal of Molecular Biology* **10**, 42-IN49 (1964).
93 Asakura, S., Eguchi, G. & Iino, T. Unidirectional growth of Salmonella flagella in vitro. *Journal of Molecular Biology* **35**, 227-236 (1968).
94 Ali, J. *et al.* Bacteria-inspired nanorobots with flagellar polymorphic transformations and bundling. *Scientific Reports* **7**, 1-10 (2017).
95 Ali, J., Cheang, U. K., Darvish, A., Kim, H. & Kim, M. J. Biotemplated flagellar nanoswimmers. *Apl Materials* **5**, 116106 (2017).
96 Cheang, U. K., Roy, D., Lee, J. H. & Kim, M. J. Fabrication and magnetic control of bacteria-inspired robotic microswimmers. *Applied Physics Letters* **97**, 213704 (2010).
97 Nasatto, P. *et al.* Methylcellulose, a cellulose derivative with original physical properties and extended applications. *Polymers* **7**, 777-803 (2015).
98 Hai-Lang, Z. & Shi-Jun, H. Viscosity and density of water+ sodium chloride+ potassium chloride solutions at 298.15 K. *Journal of Chemical & Engineering Data* **41**, 516--520 (1996).
99 Ali, J. *et al.* Bacteria-inspired nanorobots with flagellar polymorphic transformations and bundling. *Scientific Reports* **7**, 14098 (2017).
100 Schamel, D. *et al.* Nanopropellers and their actuation in complex viscoelastic media. *ACS Nano* **8**, 8794-8801 (2014).
101 Teran, J., Fauci, L. & Shelley, M. Viscoelastic fluid response can increase the speed and efficiency of a free swimmer. *Physical Review Letters* **104**, 038101 (2010).
102 Lauga, E. Propulsion in a viscoelastic fluid. *Physics of Fluids* **19**, 083104 (2007).
103 Michalet, X. Mean square displacement analysis of single-particle trajectories with localization error: Brownian motion in an isotropic medium. *Physical Review E* **82**, 041914 (2010).

104 Haario, H., Laine, M., Mira, A. & Saksman, E. DRAM: efficient adaptive MCMC. *Statistics and Computing* **16**, 339-354 (2006).
105 Chen, Y.-F., Wei, H.-H., Sheng, Y.-J. & Tsao, H.-K. Superdiffusion in dispersions of active colloids driven by an external field and their sedimentation equilibrium. *Physical Review E* **93**, 042611 (2016).
106 Bachmann, F., Bente, K., Codutti, A. & Faivre, D. Using Shape Diversity on the Way to Structure-Function Designs for Magnetic Micropropellers. *Physical Review Applied* **11**, 034039 (2019).
107 Kim, M., Bird, J. C., Van Parys, A. J., Breuer, K. S. & Powers, T. R. A macroscopic scale model of bacterial flagellar bundling. *Proceedings of the National Academy of Sciences* **100**, 15481--15485 (2003).
108 Kim, M. J. *et al.* Particle image velocimetry experiments on a macro-scale model for bacterial flagellar bundling. *Experiments in Fluids* **37**, 782--788 (2004).
109 Diamandis, E. P. & Christopoulos, T. K. The biotin-(strept) avidin system: principles and applications in biotechnology. *Clinical Chemistry* **37**, 625-636 (1991).
110 Mellnik, J. W. R. *et al.* Maximum likelihood estimation for single particle, passive microrheology data with drift. *Journal of Rheology* **60**, 379--392 (2016).
111 Campuzano, S. *et al.* Magnetic Janus particles for static and dynamic (bio) sensing. *Magnetochemistry* **5**, 47 (2019).
112 Kirillova, A., Marschelke, C. & Synytska, A. Hybrid Janus particles: challenges and opportunities for the design of active functional interfaces and surfaces. *ACS Applied Materials & Interfaces* **11**, 9643-9671 (2019).
113 Kirillova, A. *et al.* Hybrid hairy Janus particles decorated with metallic nanoparticles for catalytic applications. *ACS Applied Materials & Interfaces* **7**, 21218-21225 (2015).
114 Baraban, L. *et al.* Transport of cargo by catalytic Janus micro-motors. *Soft Matter* **8**, 48-52 (2012).
115 Yi, Y., Sanchez, L., Gao, Y., Lee, K. & Yu, Y. Interrogating cellular functions with designer Janus particles. *Chemistry of Materials* **29**, 1448-1460 (2017).
116 Wu, Z. *et al.* A microrobotic system guided by photoacoustic computed tomography for targeted navigation in intestines in vivo. *Science Robotics* **4** (2019).
117 Brown, A. & Poon, W. Ionic effects in self-propelled Pt-coated Janus swimmers. *Soft Matter* **10**, 4016-4027 (2014).
118 Das, S. *et al.* Boundaries can steer active Janus spheres. *Nature Communications* **6**, 1-10 (2015).
119 Campbell, A. I., Ebbens, S. J., Illien, P. & Golestanian, R. Experimental observation of flow fields around active Janus spheres. *Nature Communications* **10**, 1-8 (2019).
120 Chattopadhyay, P. & Simmchen, J. Interactions of different Janus particles with passive tracers. (2019).
121 Gomez-Solano, J. R., Blokhuis, A. & Bechinger, C. Dynamics of self-propelled Janus particles in viscoelastic fluids. *Physical Review Letters* **116**, 138301 (2016).
122 Ebbens, S., Tu, M.-H., Howse, J. R. & Golestanian, R. Size dependence of the propulsion velocity for catalytic Janus-sphere swimmers. *Physical Review E* **85**, 020401 (2012).
123 Ke, H., Ye, S., Carroll, R. L. & Showalter, K. Motion analysis of self-propelled Pt− silica particles in hydrogen peroxide solutions. *The Journal of Physical Chemistry A* **114**, 5462-5467 (2010).

124 Michelin, S. & Lauga, E. Geometric tuning of self-propulsion for Janus catalytic particles. *Scientific Reports* **7**, 1-9 (2017).
125 Choudhury, U., Soler, L., Gibbs, J. G., Sanchez, S. & Fischer, P. Surface roughness-induced speed increase for active Janus micromotors. *Chemical Communications* **51**, 8660-8663 (2015).
126 Uspal, W. Theory of light-activated catalytic Janus particles. *The Journal of Chemical Physics* **150**, 114903 (2019).
127 Huang, Z. *et al.* Bacteria-Activated Janus Particles Driven by Chemotaxis. *ACS Nano* **12**, 6725-6733 (2018).
128 Ma, X. & Sánchez, S. Bio-catalytic mesoporous Janus nano-motors powered by catalase enzyme. *Tetrahedron* **73**, 4883-4886 (2017).
129 Pinchasik, B. E., Möhwald, H. & Skirtach, A. G. Mimicking Bubble Use in Nature: Propulsion of Janus Particles due to Hydrophobic-Hydrophilic Interactions. *Small* **10**, 2670-2677 (2014).
130 Schattling, P. S., Ramos-Docampo, M. A., Salgueiriño, V. & Städler, B. Double-fueled Janus swimmers with magnetotactic behavior. *ACS Nano* **11**, 3973-3983 (2017).
131 Gao, W., D'Agostino, M., Garcia-Gradilla, V., Orozco, J. & Wang, J. Multi-fuel driven janus micromotors. *Small* **9**, 467-471 (2013).
132 Halliwell, B., Clement, M. V., Ramalingam, J. & Long, L. H. Hydrogen peroxide. Ubiquitous in cell culture and in vivo? *IUBMB Life* **50**, 251-257 (2000).
133 Lynn Humberston, C., Dean, B. S. & Krenzelok, E. P. Ingestion of 35% hydrogen peroxide. *Journal of Toxicology: Clinical Toxicology* **28**, 95-100 (1990).
134 Pritchett, S., Green, D. & Rossos, P. Accidental Ingestion of 35% Hydrogen Peroxide. *Canadian Journal of Gastroenterology* **21**, 423217 (2007).
135 Chatterjee, P., Tang, E. M., Karande, P. & Underhill, P. T. Propulsion of catalytic Janus spheres in viscosified Newtonian solutions. *Physical Review Fluids* **3**, 014101 (2018).
136 Lai, S. K., Wang, Y.-Y., Wirtz, D. & Hanes, J. Micro- and macrorheology of mucus. *Advanced Drug Delivery Reviews* **61**, 86-100 (2009).
137 Kei Cheang, U., Lee, K., Julius, A. A. & Kim, M. J. Multiple-robot drug delivery strategy through coordinated teams of microswimmers. *Applied Physics Letters* **105**, 083705 (2014).
138 Tang, J., Rogowski, L. W., Zhang, X. & Kim, M. J. Flagellar nanorobot with kinetic behavior investigation and 3D motion. *Nanoscale* (2020).
139 Ali, J. *et al.* Fabrication and magnetic control of alginate-based rolling microrobots. *AIP Advances* **6**, 125205 (2016).
140 Stanton, M. M., Simmchen, J., Ma, X., Miguel-López, A. & Sánchez, S. Biohybrid janus motors driven by Escherichia coli. *Advanced Materials Interfaces* **3**, 1500505 (2016).
141 Mellnik, J. W. *et al.* Maximum likelihood estimation for single particle, passive microrheology data with drift. *Journal of Rheology* **60**, 379-392 (2016).
142 Rogowski, L. W. *et al.* in *2019 International Conference on Robotics and Automation (ICRA), Montreal, Canada.* 1352-1357 (IEEE).
143 Ebagninin, K. W., Benchabane, A. & Bekkour, K. Rheological characterization of poly (ethylene oxide) solutions of different molecular weights. *Journal of Colloid and Interface Science* **336**, 360-367 (2009).
144 Rogowski, L. W. *et al.* in *2019 International Conference on Robotics and Automation (ICRA)* 1352--1357 (2019).

145 Malekian, B. *et al.* Fabrication and Characterization of Plasmonic Nanopores with Cavities in the Solid Support. *Sensors* **17**, 1444 (2017).
146 Quach, A. & Simha, R. Pressure-volume-temperature properties and transitions of amorphous polymers; polystyrene and poly (orthomethylstyrene). *Journal of Applied Physics* **42**, 4592-4606 (1971).
147 Cheang, U. K., Kim, H., Milutinović, D., Choi, J. & Kim, M. J. Feedback control of an achiral robotic microswimmer. *Journal of Bionic Engineering* **14**, 245-259 (2017).
148 Ali, J., Kim, H., Cheang, U. K. & Kim, M. J. Micro-PIV measurements of flows induced by rotating microparticles near a boundary. *Microfluidics and Nanofluidics* **20**, 131 (2016).
149 Huppler, J., Ashare, E. & Holmes, J. Rheological Properties of Three Solutions. Part I. Non-Newtonian Viscosity, Normal Stresses, and Complex Viscosity. *Transactions of the Society of Rheology* **11**, 159-179 (1967).
150 Kulicke, W., Kiss, G. & Porter, R. S. Inertial normal-force corrections in rotational rheometry. *Rheologica Acta* **16**, 568-572 (1977).